

# AUS Repository

## Microstructures-Based Constitutive Modelling for Dynamic Strain Aging in Metal Alloys

Item Type	Dissertation
Authors	Hassan, Arhum
Download date	2026-05-20 16:35:35
Link to Item	<a href="https://hdl.handle.net/11073/25653">https://hdl.handle.net/11073/25653</a>

MICROSTRUCTURES-BASED CONSTITUTIVE MODELLING FOR DYNAMIC  
STRAIN AGING IN METAL ALLOYS

by

Arhum Hassan

A Dissertation Presented to the Faculty of the  
American University of Sharjah  
College of Arts and Sciences  
in Partial Fulfillment  
of the Requirements  
for the Degree of

Doctor of Philosophy in  
Materials Science and Engineering

Sharjah, United Arab Emirates

September 2024

## Declaration of Authorship

I declare that this dissertation is my own work and, to the best of my knowledge and belief, it does not contain material published or written by a third party, except where permission has been obtained and/or appropriately cited through full and accurate referencing.

Signature .....Arhum Hassan.....

Date .....02-Sep-2024.....

The Author controls copyright for this report.  
Material should not be reused without the consent of the author. Due  
acknowledgement should be made where appropriate.

© Year 2024

Arhum Hassan

ALL RIGHTS RESERVE

## **Approvals**

We, the undersigned, approve the PhD Dissertation written by Arhum Hassan

Dissertation Title: Microstructures-Based Constitutive Modelling for Dynamic Strain Aging in Metal Alloys

Date of Defense: 02-Sep-2024

### **Name, Title and Affiliation**

---

Dr. Farid Abed  
Professor  
Department of Civil Engineering  
Dissertation Advisor

---

Dr. Ali Alnaser  
Professor  
Department of Physics  
Dissertation Committee Member

---

Dr. Wael Abuzaid  
Associate Professor  
Department of Mechanical Engineering  
Dissertation Committee Member

---

Dr. Maen Alkhader  
Professor  
Department of Mechanical Engineering  
Dissertation Examiner

---

Dr. Syed Wilayat Husain  
Professor  
Department of Materials Science and Engineering  
Dissertation Examiner

---

Accepted by:  
Dr. Mohamed El-Tarhuni  
Vice Provost for Research and Graduate Studies  
Office of Research and Graduate Studies

## Acknowledgements

First and foremost, I am deeply grateful to **Allah Almighty** for His countless blessings. His grace has been my strength during this challenging path.

I would like to extend sincere thanks to the **American University of Sharjah** for providing a platform that supported my academic and career growth. I am particularly grateful for the **Graduate Assistantship**, which played a crucial role in facilitating my research and professional development.

I am especially grateful to my supervisor, **Professor Farid Abed**, for his guidance, patience, and support during both my academic and personal challenges. His mentorship has been invaluable.

Special thanks to **Professor Ali Alnaser**, Program Coordinator, for his continuous support, guidance, and opportunities throughout my journey. His encouragement played a pivotal role in shaping my experience.

I am also thankful to the **Dissertation Advisory Committee** and the **Examination Committee** for their time and valuable feedback, which significantly improved the quality of this research.

To my **parents, siblings, wife, and daughter**, your endless love and encouragement have been the foundation of my success. I am deeply thankful for your unwavering belief in me. Words cannot explain how grateful I am for your sacrifices, patience, and support in helping me become the person I am today.

I also appreciate my **friends** and **colleagues**, whose support made this journey more manageable and rewarding. Your companionship and encouragement were essential throughout this process.

Lastly, I would like to acknowledge all those whose names may not appear here but who have contributed to my personal and professional growth in numerous ways. Thank you for being part of this journey.

## **Dedications**

To my beloved parents, for their endless love.

To my wife and daughter, for their unwavering support, sacrifice and patience.

And to all those who believed in me throughout this journey.

## Abstract

Dynamic Strain Aging (DSA) is encountered in some metals at certain combinations of temperatures and strain rates. DSA phenomenon arises due to interactions between mobile dislocations and solute atoms that diffuse around them. This dissertation aims to deepen the understanding of dynamic strain aging in different metals and alloys through a comprehensive approach that incorporates microstructure-based constitutive modeling and finite element (FE) analysis. The constitutive model developed in this study incorporates the effect of increased waiting time that activates DSA. This is achieved by introducing diffusion parameters into the model to formulate an expression that predicts the temperature ranges for the activation of DSA at different strain rates. The framework is based on material-specific activation energy for diffusion and the diffusion constants of impurity/solute atoms, with the increase in strength associated with the concentration of these atoms. The model is validated through comparison with experimental results over a broad temperature range for pure metals and alloys such Niobium, Vanadium and Titanium, C45 steel alloy and MMFX high strength steel at different strain rates (0.0015/s – 0.15/s) and over a wide range of temperatures (298K – 923K). The constitutive model was implemented in the commercially available FE software ABAQUS using a user-defined material subroutine coded as VUMAT. The simulation results were validated using available experimental results, both in the presence and absence of DSA, over a broad range of temperatures (200K – 900K) and strain rates (0.001/s – 2200/s) for all the metals and alloys discussed. Moreover, the FE simulations presented in this dissertation indicate that necking initiates earlier in the presence of DSA. The underlying reason is the increased viscosity due to the increased waiting time, which reduces the material's ability to deform plastically, leading to early failure. Overall, the developed models contribute to a comprehensive understanding of the metallic response under thermomechanical loading scenarios, providing valuable insights into the behaviour of metals and alloys subject to DSA.

**Keywords:** Dynamic Strain Aging, Constitutive Modelling, Damage Modelling, Finite Element Modelling.

## Table of Contents

Abstract .....	6
List of Figures .....	9
List of Tables .....	15
Chapter 1. Introduction.....	16
1.1. Problem Statement .....	18
1.2. Research Objectives .....	18
1.3. Outline.....	20
Chapter 2. Literature Review.....	22
2.1. Thermomechanical Models.....	29
2.2. FE Models .....	32
2.3. Voyiadjis-Abed (VA) Constitutive Model.....	35
2.3.1. For bcc metals .....	36
2.3.2. For fcc metals.....	38
2.3.3. For hcp metals.....	40
2.3.4. For alloys .....	41
2.4. Adiabatic Heating at Very High Strain Rates .....	44
2.5. Damage Model.....	44
Chapter 3. Research Methodology .....	47
3.1. Theoretical/Constitutive Model Development.....	47
3.1.1. The first approach .....	47
3.1.2. The second approach.....	51
3.1.3. The third approach .....	53
3.1.4. Model parameter evaluation .....	57
3.2. FE Modelling .....	58
3.3. Potential Implications .....	67

Chapter 4.	Results and Discussions .....	68
4.1.	Commercially Pure Niobium (CP-Nb) .....	68
4.2.	CP-Vanadium (CP-V) .....	72
4.3.	CP-Titanium (CP-Ti) .....	76
4.4.	Martensitic Microcomposite Formable (MMFX) Steel .....	82
4.5.	Medium Carbon C45 Steel .....	85
4.6.	Damage Modeling .....	90
Chapter 5.	FE Modelling .....	94
5.1.	CP-Niobium .....	95
5.2.	CP-Vanadium .....	96
5.3.	CP-Titanium .....	97
5.4.	MMFX Steel .....	97
5.5.	C45 Steel .....	100
Chapter 6.	Numerical Examples .....	104
6.1.	Necking Problem .....	104
6.1.1.	CP-Niobium .....	104
6.1.2.	CP-Vanadium .....	107
6.2.	Shear Hat Problem .....	109
6.2.1.	BCC Niobium .....	110
Chapter 7.	Conclusions .....	113
References	.....	117
Vita	.....	127

## List of Figures

Figure 1 Different types of serrations during deformation of metal [47].	24
Figure 2 Stress–strain curves of different steels with varying carbon and nickel compositions at a strain rate of 0.0001/s [55].	27
Figure 3 TEM images 800H alloy samples at 1023 K temperature and true strain of 0.2 strain deformed with a strain rate of (a) 0.1/s, and (b) 0.01/s [57].	29
Figure 4. Stress vs Temperature profile at different strain rates for C45E steel [32].	30
Figure 5 Isothermal flow stress at different temperature and strain rates at a plastic strain of 0.1 for experimental data, JC and modified PTW models [68].	33
Figure 6 Comparison between the experimental data (grey) and the model predicted flow stress curves (black) (a) 298 K, (b) 388 K, (c) 458 K, and (d) 508 K [70].	34
Figure 7 Comparison of the experimental data with predicted stress-strain curves for the VA model, the modified VA model, and the FE results at different temperatures and a strain rate of (a) 0.0015/s, and (b) 0.15/s [69].	34
Figure 8 Comparison of the VA model for bcc metal (Tantalum) with the experimental data [9].	38
Figure 9 Comparison of the VA model for fcc metal (Oxygen-free high thermal conductivity (OFHC) copper) with the experimental data [9].	39
Figure 10 Comparison of the VA model results for hcp metals with the experimental data for commercially pure titanium [8].	41
Figure 11 True Stress-True Strain curves for Al-6XN stainless alloy showing both thermal yielding and thermal hardening phenomena. Blue lines indicate the VA model for alloys given in Eqn. (20) [15].	43
Figure 12: The experimental values of a) Thermal Yielding Stress and b) Thermal Hardening Stress against temperature for the cases of DSA absence [8, 9], and with the presence of DSA at different strain rates for C45 steel [21].	50
Figure 13 Schematics for the development of solute atmosphere and interactions with dislocations where (a) shows the bond breakage under applied stress thus causing slippage in the structure and (b) shows the formation of dislocation pinning and the Cottrell’s atmosphere.	52

Figure 14 Schematic representation of impurity interaction with the dislocations. The mobile dislocations pin due to impurities diffusion along the dislocation line.....	54
Figure 15 Stress-temperature curves experimentally determined for various strain rates at a plastic strain of 10% for Niobium [44]. .....	68
Figure 16 Comparison of Stress vs Temperature for the two models against the experimental data for Niobium at a plastic strain of 10% at $\dot{\epsilon}_p = 0.001/s$ . .	70
Figure 17 Stress-temperature relationship at various plastic strain levels in Niobium at $\dot{\epsilon}_p = 0.001/s$ [44]. .....	71
Figure 18 Stress-Strain curves at $\dot{\epsilon}_p = 0.001/s$ for the VA model with and without DSA in comparison to the experimental data for Niobium. The temperatures considered are (a) 293 K, (b) 400 K, (c) 500 K, (d) 600 K, (e) 700 K, and (f) 800 K. ....	72
Figure 19 Stress-temperature curves experimentally determined for various strain rates at a plastic strain of 10% for CP-Vanadium [24]......	73
Figure 20 Comparison of Stress vs Temperature for the two models against the experimental data for Vanadium at a plastic strain of 10% at $\dot{\epsilon}_p = 0.001/s$ . .....	75
Figure 21 Stress-temperature relationship at various plastic strain levels in Vanadium at $\dot{\epsilon}_p = 0.001/s$ [24]. .....	75
Figure 22 Stress-Strain curves at $\dot{\epsilon}_p = 0.001/s$ for the VA model with and without DSA in comparison to the experimental data for Vanadium. The temperatures considered are (a) 293 K, (b) 400 K, (c) 500 K, (d) 600 K, (e) 700 K, and (f) 800 K. ....	77
Figure 23 Experimental stress vs temperature with increase in plastic strain at (a) $\dot{\epsilon}_p = 0.001/s$ , and (b) $\dot{\epsilon}_p = 2200/s$ .....	78
Figure 24 Comparison of the VA and Modified VA models to the experimental Stress vs Temperature profile at the yield point and 20% plastic strain and at (a) $\dot{\epsilon}_p = 0.001/s$ , and (b) $\dot{\epsilon}_p = 2200/s$ . ....	79
Figure 25 Comparison of Stress-Strain profile of CP-Ti for the VA model with and without the DSA component at $\dot{\epsilon}_p = 0.001/s$ and T = (a) 77 K, (b) = 296 K, (c) = 473 K, and (d) = 673K.....	80

Figure 26 Comparison of Stress-Strain profile of CP-Ti for the VA model with and without the DSA component at $\dot{\epsilon}_p = 2200/s$ and $T =$ (a) 77 K, (b) = 296 K, (c) = 498 K, and (d) = 698 K.....	81
Figure 27 Stress-temperature curves experimentally determined for various plastic strains at strain rates of (a) 0.0015/s and (b) 0.15/s for MMFX steel [14]..	82
Figure 28 Stress vs Temperature comparison, at 1% plastic strain, between the two models with the experimental data for MMFX at (a) $\dot{\epsilon}_p = 0.0015/s$ and (b) $\dot{\epsilon}_p = 0.15/s$ .....	84
Figure 29 Stress-Strain curves for original VA model, modified VA model, and experimental data at $\dot{\epsilon}_p = 0.0015/s$ and (a) $T = 298$ K, (b) $T = 523$ K, (c) $T = 723$ K, and (d) $T = 923$ K for MMFX steel.....	85
Figure 30 Stress-Strain curves for original VA model, modified VA model, and experimental data at $\dot{\epsilon}_p = 0.15/s$ and (a) $T = 298$ K, (b) $T = 523$ K, (c) $T = 723$ K, and (d) $T = 923$ K for MMFX steel.....	86
Figure 31 Stress vs Temperature curve for C45 Steel at the yield point and different $\dot{\epsilon}_p$ for (a) $\dot{\epsilon}_p = 0.0015/s$ and (b) $\dot{\epsilon}_p = 0.15/s$ [21].....	88
Figure 32 Stress vs Temperature comparison at 4% plastic strain between the two model with the experimental data for (a) $\dot{\epsilon}_p = 0.0015/s$ and (b) $\dot{\epsilon}_p = 0.15/s$ .....	88
Figure 33 Stress-Strain curves defining the parameters for athermal component of VA model, in comparison to the experimental data, at $T = 923K$ and (a) $\dot{\epsilon}_p = 0.0015/s$ and (b) $\dot{\epsilon}_p = 0.15/s$ .....	89
Figure 34 Stress-Strain curves for original VA model, modified VA model, and experimental data at $T = 298K$ and (a) $\dot{\epsilon}_p = 0.0015/s$ and (b) $\dot{\epsilon}_p = 0.15/s$ strain rate. ....	89
Figure 35 Stress-Strain curves for original VA model, modified VA model, and experimental data at $T = 523K$ and (a) $\dot{\epsilon}_p = 0.0015/s$ and (b) $\dot{\epsilon}_p = 0.15/s$ strain rate. ....	90
Figure 36 Stress-Strain curves for original VA model, modified VA model, and experimental data at $T = 723K$ and (a) $\dot{\epsilon}_p = 0.0015/s$ and (b) $\dot{\epsilon}_p = 0.15/s$ .	90
Figure 37 Comparison of the stress-strain curves obtained through the modified constitutive model at different temperatures and strain rate of (a, c, and e)	

0.0015/s and (b, d, and f) 0.15/s in the presence and absence of damage parameter with the experimental data. ....	91
Figure 38 Modified VA Model with and without the damage parameter compared to experimental data at $\dot{\epsilon}p = 0.0015/s$ and (a) $T = 298\text{ K}$ , (b) $T = 523\text{ K}$ , (c) $T = 723\text{ K}$ , (d) $T = 923\text{ K}$ .....	92
Figure 39 Modified VA Model with and without the damage parameter compared to experimental data at $\dot{\epsilon}p = 0.15/s$ and (a) $T = 298\text{ K}$ , (b) $T = 523\text{ K}$ , (c) $T = 723\text{ K}$ , (d) $T = 923\text{ K}$ .....	93
Figure 40 Sketch of the uniaxial sample tested in FE simulations. (a) The loaded sample. (b) Quarter of the problem. (c) Applied loading profile .....	94
Figure 41 Comparison of the experimental stress against the flow stress obtained using the constitutive model and FE simulations for CP-Niobium. At a strain rate of 0.001/s, (a) gives the stress vs temperature profile while (b), (c), and (d) gives the stress-strain comparison at 500K, 600K, and 700K respectively.....	95
Figure 42 Comparison of the experimental stress against the flow stress obtained using the constitutive model and FE simulations for CP-Vanadium. At a strain rate of 0.001/s, (a) gives the stress vs temperature profile while (b), (c), and (d) gives the stress-strain comparison at 600K, 700K, and 800K respectively.....	96
Figure 43 Comparison of the experimental stress against the flow stress obtained using the constitutive model and FE simulations for CP-Titanium at a strain rate of 0.001/s, and temperatures of (a) 77K, (b) 296K, (c) 473K and (d) 673K.....	98
Figure 44 Comparison of the experimental stress against the flow stress obtained using the constitutive model and FE simulations for CP-Titanium at a strain rate of 2200/s, and temperatures of (a) 77K, (b) 296K, (c) 473K and (d) 673K.....	99
Figure 45 Stress-Temperature profile obtained through the constitutive model for MMFX steel and the FE simulations and its comparison with the experimental data at a strain rate of (a) 0.0015/s and (b) 0.15/s. ....	100
Figure 46 Stress-Strain profiles obtained through the constitutive model and the FE simulations for MMFX steel in comparison to the experimental data at a	

strain rate of 0.0015/s and temperatures of (a) 298 K, (b) 523 K, (c) 723 K, and (d) 923 K.....	101
Figure 47 Stress-Strain profiles obtained through the constitutive model and the FE simulations for MMFX steel in comparison to the experimental data at a strain rate of 0.15/s and temperatures of (a) 298 K, (b) 523 K, (c) 723 K, and (d) 923 K.....	102
Figure 48 Comparison of the flow stress at different temperatures and $\epsilon_p$ of (a) 0.0015/s and (b) 0.15/s for C45 steel.....	102
Figure 49 Comparison of the stress-strain profile at $\epsilon_p = 0.0015/s$ and $T =$ (a) 298K, (b) 523K, (c) 723K, and (d) 923K for C45 steel. ....	103
Figure 50 Comparison of the stress-strain profile at $\epsilon_p = 0.15/s$ and $T =$ (a) 298K, (b) 523K, (c) 723K, and (d) 923K for C45 steel.....	103
Figure 51 Sketch of the uniaxial sample tested in FE simulations for necking problem. (a) The loaded sample. (b) Quarter of the problem with mesh (7 x 30). (c) Applied loading profile. ....	105
Figure 52 Mesh geometry for the necking problem where (a) gives the quarter of the axisymmetric sample while (b) shows the complete cylindrical sample subjected to the necking application. ....	106
Figure 53 Deformed Nb sample at $\epsilon_p = 0.001/s$ and $T = 600$ K in the (a) absence and (b) presence of DSA. (c) Radius reduction, (d) Longitudinal stress, and (e) Equivalent plastic strain against the longitudinal strain with and without DSA.....	107
Figure 54 Deformed Nb sample at $\epsilon_p = 0.001/s$ and $T = 700$ K in the (a) absence and (b) presence of DSA. (c) Radius reduction, (d) Longitudinal stress, and (e) Equivalent plastic strain against the longitudinal strain with and without DSA.....	108
Figure 55 Deformed V sample at $\epsilon_p = 0.001/s$ and $T = 600$ K in the (a) absence and (b) presence of DSA. (c) Radius reduction, (d) Longitudinal stress, and (e) Equivalent plastic strain against the longitudinal strain with and without DSA.....	109
Figure 56 Deformed V sample at $\epsilon_p = 0.001/s$ and $T = 700$ K in the (a) absence and (b) presence of DSA. (c) Radius reduction, (d) Longitudinal stress, and (e)	

Equivalent plastic strain against the longitudinal strain with and without DSA. ....	110
Figure 57 (a) Sketch, and (b) section view of the axisymmetric hat-shaped sample.	111
Figure 58 Path specified for the shear localization due to axial loading conditions..	111
Figure 59 (a) Stress distribution across the deformed sample, (b) Equivalent plastic strain along the path, and (c) Nodal displacement after deformation for Nb at 0.001/s strain rate and 600K temperature.....	112
Figure 60 (a) Stress distribution across the deformed sample, (b) Equivalent plastic strain along the path, and (c) Nodal displacement after deformation for Nb at 0.001/s strain rate and 600K temperature.....	112

## List of Tables

Table 1 Diffusion Equation Parameters for impurity diffusion in CP-Niobium .....	69
Table 2 Model Parameters for CP-Niobium. ....	69
Table 3 Diffusion Equation Parameters for impurity diffusion in CP-Vanadium .....	74
Table 4 Model parameters for CP-Vanadium .....	74
Table 5 Diffusion Equation Parameters for impurity diffusion in CP-Titanium .....	78
Table 6 Model parameter values for CP-Titanium .....	79
Table 7. MMFX average chemical composition [14] .....	83
Table 8. Model parameters for MMFX steel. ....	83
Table 9 C45 steel composition [21] .....	86
Table 10 Model Parameters for C45 Steel .....	87

## Chapter 1. Introduction

Researchers have been able to predict the thermomechanical behavior of metals over a broad range of strain rates and temperatures through the utilization of different computational approaches. However, there are still challenges with making reliable numerical models for Dynamic Strain Aging (DSA), during which, the metal gets stronger because of interactions between the diffusing impurity/solute atoms and mobile dislocations. During thermomechanical loading conditions, DSA appears as a sudden increase in the mechanical strength of an alloy under certain combinations of strain rate and temperature. Metals, due to their ductile nature, exhibit plastic slip, under an applied stress which results in the discrete mobility of the dislocations. This means that the flow is not continuous, and the dislocations must wait for a certain amount of time known as the waiting time ( $t_w$ ) at each local obstacle before they move on to the next one. During the waiting period, the adjacent solute atoms initiate a process of pipe diffusion into the dislocation core region, where they engage in interactions with the mobile dislocations, resulting in a deceleration of their motion. This is also termed as dislocation pinning. This requires extra stress for further movement of dislocations, which results in an increase in strength called as dynamic strain aging (DSA) that has been reported in numerous studies [1-6].

The interactions between the dislocations and solute atoms gives rise to DSA activation in a metal, that is contingent upon various factors, including the lattice parameters, type of impurity and its diffusion parameters, crystal structure etc. Furthermore, these parameters establish the temperature range within which DSA phenomenon will be activated, under a specific strain rate condition. Cheng and Nasser showed that the thermal activation free energy and the thermal stress is implicitly dependent on the concentration of solute atoms which is indirectly influenced by the time required for the diffusion of solute atoms into the dislocation core [4]. Additionally, the diffusion kinetics, which are determined by the diffusion constant and diffusion energy, also exhibit variation which depends on the type of solute and solvent atoms [7].

In addition to the study of diffusion kinetics, the thermomechanical properties of these metals are influenced by the nature of the obstacles encountered by the dislocations in

motion [8]. They can be long-ranged for face-centered cubic (fcc) metals and short-ranged for body-centered cubic (bcc) metals. That is why the temperature dependence of stress in fcc metals, is observed in the plastic deformation region whereas in bcc metals, it is observed at the yield points [8, 9]. In contrast, it has been observed that hexagonal close-packed (hcp) metals [8, 9] and alloys [10-15] exhibit both thermal yielding and thermal hardening phenomena. Various numerical approaches have been effectively employed in the literature to model the thermomechanical responses of these metals and alloys in the absence of DSA [11, 15-25].

However, these models have been found to be ineffective in capturing DSA and therefore, have been modified using different numerical approaches to predict the activation of DSA [26-32]. These approaches are either empirical in nature or are material specific as discussed in the subsequent sections. Hence, it is imperative to develop a constitutive model based on the physical constants of material, which can also account for the diffusion kinetics of the solute atoms and their interactions with the dislocations, that can accurately capture the activation of dynamic strain aging in various metals and alloys. In order to address this issue, a constitutive model has been developed in this dissertation that encompasses a wide range of temperatures and strain rates for various metals and alloys that exhibit dynamic strain aging.

In addition, beyond the ultimate stress value while approaching failure, a material experiences permanent deformation due to stress induced plasticity, which results in a decrease in its capacity to withstand stress. Several studies [17, 21, 33-41] have reported this phenomenon, which is generally referred to as damage in the material and is usually associated with the microstructure of the material. In order to accurately represent this process, an energy-based damage model has been integrated with the developed constitutive model for different alloys in this work. Later, the constitutive model is integrated in ABAQUS through a user-defined VUMAT subroutine to perform FE simulations. Realtime numerical problems have been simulated to study the necking and shearing in metals exhibiting DSA. In summary, this dissertation investigates the fundamental mechanisms and predictive modelling of dynamic strain aging (DSA) in metal alloys through an extensive approach that integrates constitutive modelling, and Finite Element (FE) modelling.

## **1.1. Problem Statement**

Despite extensive research conducted on dynamic strain aging, the existing literature does not provide a comprehensive physical constitutive model that adequately incorporates the phenomenon of dynamic strain aging across various metals and alloys. Furthermore, the existing models lack the ability to accurately represent the mechanisms of diffusion and the interactions that occur between diffusing impurities or solutes and the mobile dislocations. The current models available can be categorized as either empirical or metal-specific, and they do not possess the ability to effectively predict the temperature ranges for dynamic strain aging (DSA) at a given strain rate. Likewise, there is a necessity for enhancing the current finite element models in order to capture DSA. The existing numerical models do not incorporate the diffusion mechanics necessary for accurately predicting the temperature range needed for impurity diffusion at specific strain rates. Moreover, the effect of the concentration of these diffusing impurities also needs to be employed. As a result, the usefulness of the currently developed models is limited to a small range of metals and alloys.

## **1.2. Research Objectives**

The main objective of the current work is to develop a physically constitutive model that is thermodynamically valid and accounts for the activation of dynamic strain aging based on the diffusion of impurity or solute atoms and their interactions with the dislocations. Moreover, the model needs to be applicable over a wide range of temperature and strain rates. This dissertation provides a comprehensive constitutive model that can predict the activation region of DSA over a broad range of temperatures and strain rates. Moreover, during plasticity, the metal experiences damage due to creation of micro voids and defects. This reduces the metallic strength after reaching the ultimate strength. For this reason, the current model is coupled with an energy-based damage parameter, thereby facilitating the generation of comparable results due to thermal softening and microstructural damage in the material. The current research follows the framework outlined below:

1. Development of a physical constitutive relation that can model the plastic flow stress for metals with different crystal structure and capture the activation of dynamic strain aging based on the diffusion kinetics and concentration of the impurities or solute atoms in the studied alloys.

Dislocations move in a discrete manner and stop at each obstacle before moving on to the next one. During DSA, the impurity or solute atoms diffuse into the dislocation core through pipe diffusion and restrict their movement also known as dislocation pinning. This pinning increases the dislocation waiting time at obstacles until it reaches the time required for impurities relaxation time. At this point, the specific conditions of strain rate and temperature is reached which gives rise to the initiation of DSA. However, the impurity concentration along dislocation during DSA activation depends on the temperature at the applied strain rate and contribute to the increase in strength. These diffusion and solute concentration profile contribute to the development of the model that enables it to capture DSA. The model results are compared with the available experimental data.

2. Combination of the constitutive model with the energy-based damage evolution parameter which accounts for the material defects (such as microcracks, voids, and cavities). During plastic deformation, upon reaching the ultimate strength, the material start losing strength due to the creation of microstructural defects in the material. These defects initiate cracking that leads to failure of the material. The intensity of these damage is evaluated by using the SEM images to find the damage parameter. This enables the model to capture thermal softening and material damage beyond ultimate stress point under different thermomechanical loading conditions.
3. Implementation of the established constitutive model into a commercial FE software ABAQUS to simulate the activation of DSA under different thermomechanical loading conditions. This comprises of developing a two- and three-dimensional FE code using vectorized user material (VUMAT) subroutine in the ABAQUS FE software. This implementation has been tested through a simple uniaxial tension problem and the effect of DSA on necking behaviour of metals by determining the model parameters using the available

experimental data. The numerical model is tested, and the results are compared with the experimental findings to validate the model reliability.

### **1.3. Outline**

This dissertation mainly comprises of five chapters (Chapters 2-6) which contribute to addressing the problem statement based on the defined objectives. This dissertation gives a broad understanding of DSA, including the microstructural development of scenarios responsible for activation of DSA, the role of diffusion kinetics in the identification of correct combination of temperatures and strain rate responsible for activation of DSA, their inclusion in the constitutive model development and implementation in ABAQUS to carry out FE simulations. Moreover, most of the work presented in this dissertation has already been published in international journals and conference papers.

Chapter 2 presents an overview of the literature on dynamic strain aging, focusing on notable studies in the field. This section discusses the previously constructed numerical models, the underlying mechanism of DSA activation, and the many terminologies utilized in the literature.

Chapter 3 discusses the methodologies adopted in this dissertation for modifying the VA model to capture DSA. The first approach was based on an empirical approach that suggests a second order term to capture DSA. The second approach suggests the change in reference Gibbs free energy with a change in solute concentration during the activation of DSA. The third approach shows how the diffusion kinetics play a major role in the identification of temperature range for activation of DSA at a specific strain rate. In the later part, the approach used for implementing the model for FE simulations is discussed.

Chapter 4 presents the results obtained through the constitutive model that was obtained through the introduction of diffusion parameters. Different commercially pure metals (bcc and hcp) and alloys are studied. The model results are compared with the available experimental data for different metals and alloys.

Chapters 5 and 6 discuss the FE simulations for the constitutive model developed in this dissertation. A simple uniaxial tension problem is presented in chapter 5. The

problem is simulated in commercially available software ABAQUS to validate the thermomechanical response of metals in the presence of DSA. The constitutive model is incorporated in the software by writing a VUMAT subroutine to cover high and low strain rates application.

In chapter 6, the same subroutine is applied to simulate the role of DSA on the shear strength and ductility of the metals. A cylindrical axisymmetric problem is simulated where the metal is subjected to necking. The neck radius is compared in the presence and absence of DSA to show the effect of dynamic strain aging in metals. Moreover, a hat shaped sample is simulated to study strain localization in the shear zones

Lastly, the dissertation is concluded in chapter 7 where the future works are also highlighted.

## Chapter 2. Literature Review

One of the primary objectives in computational material science research is to develop a constitutive model that possesses broad applicability and the capacity to accurately represent complex material responses. In order to be deemed successful, a model must possess the capability to obtain the model parameters using the least experimental data, while simultaneously covering both static and dynamic material responses. Consequently, numerous investigations have been carried out to examine the thermomechanical behaviors of different metals and alloys having distinct crystal structures across a broad range of temperatures and strain rates [11, 15-17, 19]. The aforementioned models demonstrate efficacy in accurately representing standard thermomechanical behavior. However, they exhibit certain limitations in their ability to effectively model the phenomenon of DSA.

DSA activates when the impurities diffuse along the dislocation core and interact with mobile dislocations under specific combinations of temperatures and strain rates [4]. The impurities that are diffused, pin down the mobile dislocations and result in an increase in the dislocation waiting time ( $t_w$ ) at obstacles. During the activation of DSA, this waiting time equals the relaxation time required for the diffusion of impurities over the mean width of the obstacles [42]. Consequently, to continue with their movement through the local obstacles, the dislocations need extra stress and therefore, a rise in strength of the metal is observed. Metals usually have a closed pack structure and for the impurities to fit in, the interstitial sites are the only available locations. The limited space keeps them under stress and they have a high tendency to diffuse towards any larger space (whenever available) to lower their energy.

Metals exhibit ductility, a property characterized by their ability to undergo plastic deformation when subjected to external forces, resulting in a shearing effect within their atomic structure. Consequently, there is breakage of the metallic bonds and subsequently new bonds are established with adjacent atoms. Moreover, there is an increase in the mobile dislocation density due to slippage. During DSA, as the metal deforms, new sites emerge where the impurities diffuse around the dislocations through pipe diffusion and create a pinning effect, which hinders the mobility of dislocations across the obstacles [43]. Due to pinning, the waiting time for dislocation

movement increases, and it is directly related to the relaxation time needed for the diffusion of solute or impurity atoms and is influenced by the specific combination of strain rate and temperature. This interaction between impurities and dislocations activates the dynamic strain aging phenomenon in metals [28], which alters the mechanical properties of metals, and appears as an increase in their strength.

It is well known that the temperature values for initiation DSA increases proportionally with the strain rate [5, 6, 24, 44]. The observed phenomenon can be described by the correlation between an increase in strain rate and a decrease in the waiting time for dislocation movement. Consequently, this reduction in waiting time restricts the opportunity for impurity atoms to diffuse and hinder dislocations at lower temperatures. At elevated temperatures, the rate of diffusion increases, facilitating the interaction between impurity atoms and dislocations, thereby enabling dynamic strain aging (DSA) to occur at higher temperatures and strain rates. Furthermore, it is observed that as the temperature increases during dynamic strain aging (DSA) activation, there is an increase in the concentration of impurity atoms within the dislocation core [4]. This phenomenon has been found to enhance the strength of the metal until the impurity concentration saturates. At this point, a decrease in metallic strength is observed due to the reduction in solute concentration within the dislocation core, which decreases the pinning effect. [45].

As discussed before, DSA is a flow instability in a metal being deformed at a certain combination of strain rates and temperatures due to the diffusion of impurity or solute atoms. This flow instability macroscopically appears in different patterns due to a phenomenon known as the Portevin–Le Chatelier (PLC) effect and it is associated with DSA. The phenomenon being discussed pertains to the appearance of a serrated stress-strain curve or discontinuous flow, which is observed in certain metals during the process of plastic deformation. The phenomenon described is generally linked to DSA, exhibiting distinct serrations on the flow curve.

Although the physical interpretations of the PLC effect may be complex, its appearance is easily recognizable. The serrations and accompanying deformation bands have been categorized into five distinct classes, as depicted in Figure 1. Type A bands appears as small stress drops while type E bands are the same at higher strains.

Subsequently, a distinct set of type B "hopping bands" emerges, characterized by lowered stress amplitudes and reduced serration regularity. The phenomenon arises as a result of the discontinuous plastic deformation bands. Type C bands with significant and consistent stress drops are observed when the strain rate increases or the temperature decreases. The decrease in yield is attributed to the unlocking of dislocations, which is commonly observed at elevated temperatures. Type D serrations can be identified as Lüders bands, which commonly appear as plateaus in the flow stress curve [46-48].

The activation of dynamic strain aging has been documented in numerous metals and alloys while subjected to a wide range of temperatures and strain rates. The fundamental can be attributed to the interactions between the mobile dislocations and solute atoms or impurities. In the case of pure metals, DSA is activated by the diffusion of carbon, nitrogen, and oxygen impurities around the dislocation core. Conversely, in alloys, the movement of dislocations is impeded by the diffusion of interstitial or substitutional solute atoms, leading to the activation of dynamic strain aging. Depending on the metallic crystal structure, different metals and alloys activate DSA at different combinations of strain rates and temperatures [8-10, 12-14, 21]. Below are some examples from literature that discusses dynamic strain aging in several pure metals and alloys.

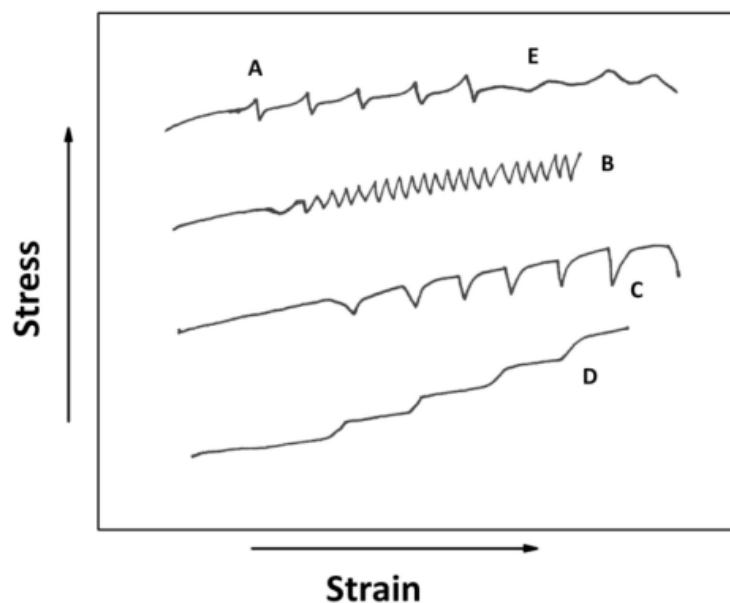


Figure 1 Different types of serrations during deformation of metal [47].

As previously mentioned, the initiation of dynamic strain aging (DSA) takes place under certain combinations of temperature and strain rate, and is influenced by the diffusion of impurities, including oxygen, nitrogen, and carbon atoms [43]. It has been reported that commercially pure bcc metals Niobium (Nb) and Vanadium (V) do not exhibit DSA at higher strain rates but show DSA at lower strain rates [24, 44]. Nemat Nasser and coworkers showed that for Nb and V, DSA activated at a strain rate of 0.001/s within specific range of temperatures for each metal. For Nb, the temperature range was 550 K – 750 K, while for V, it was 600 K – 900 K [24, 44]. The fundamental mechanism responsible for dynamic strain aging in these was reported to be the interaction of the mobile dislocations with impurities being diffused through pipe diffusion. This led to the immobilization of mobile dislocations due to pinning at nearby short-range obstacles, and resulted in higher stress before plastic deformation thus causing DSA [24, 44].

DSA mostly appears under conditions characterized by low strain rates and elevated temperatures [44], but in commercially pure Titanium (CP-Ti), the activation of this phenomenon has been documented across a wide spectrum of strain rates and temperatures, ranging from 0.001/s to 2000/s and 200K to 700K, respectively. [43]. Additionally, it has been stated that CP-Ti exhibits dynamic strain aging in the hardening region. This observation suggests that DSA only occurs after a specific level of plastic deformation has been reached. Furthermore, the occurrence of deformation twins was observed across a wide range of temperatures and strain rates, and it was found that the amount of deformation twins increased proportionally with plastic deformation. Nevertheless, the detailed study conducted by Nemat Nasser demonstrates that while the deformation twins are indeed present, they do not influence the increase in flow stress. Therefore, it can be inferred that the primary factor contributing to the increase of stress levels is dynamic strain aging [43].

Nalawade and coworkers [49] conducted elevated temperature–strain rate experiments to investigate the effect of instantaneous strain rate sensitivity on dynamic strain aging (DSA) in a Nickel base superalloy (Inconel 718). The serrated flow was observed through broad temperature range ( $T = 473 \text{ K} - 973 \text{ K}$ ) with a strain rate of  $6.5 \times 10^{-5}/\text{s}$  whereas no serrations were observed above 823 K. The substitutional diffusion of Nb

in solution treated alloy was responsible for DSA while the absence of serration above 823 K were attributed to the depletion of Nb in the matrix due to precipitation [49].

Negative strain rate sensitivity (SRS) has been observed in some alloys and is often associated with structural heterogeneity and dynamic strain aging [50-52]. Dynamic strain aging in an Al-4.8 at. % Mg alloy was studied by Aboufadi et al., at the atomic scale by Atom Probe Tomography (APT) and Transmission Electron Microscopy (TEM). It was reported that at a strain rate of  $1.67 \times 10^{-5}/s$  and room temperature, the diffusion of Mg along the dislocations gave rise to DSA while the Mg depleted area caused local softening which promotes slip localization and negative strain rate sensitivity that results in the formation of stress-strain serrations [50]. Another study on Al-Mg (AA5182-O) alloy was conducted by Jianbin et al within the temperature range of 298K – 418K and strain rates from  $10^{-4}/s$  –  $10^{-1}/s$ , where dynamic strain aging was present [52]. The experimental stress-strain curves reveal the effect of the strain rate and temperature on the serrated flow and the occurrence of PLC bands. The investigation revealed that the interplay between DSA and work hardening gives rise to distinct jerky flow patterns and contribute to the positive and negative strain rate sensitivities outside and inside the PLC band domain.

Fe-37.55Mn-8.5Al-0.6C (wt.%) low-density steel was examined by Rezvan et al. in a very recent study [53]. The novel medium entropy alloy was subjected to hot uniaxial compression tests at the temperature range of 473K – 873K and strain rate of  $0.0001/s$  –  $0.1/s$ . The post deformation analysis revealed that the serrated flow behavior and the presence of negative SRS at the temperature range of 473K – 873K indicated the activation of DSA. Just like CP-Ti [43], There was no role attributed to the martensite to austenite transformation or to the occurrence of deformation twinning to provide such deformation behavior [53]. The medium entropy enabled the short-range solute atoms diffusion, which promoted the localized mobile dislocations pinning. This created favorable circumstances for the activation of DSA at elevated temperatures. In another study, Xing et al. studied the DSA effect on negative SRS in Fe-30Mn-9Al-1C steel [54]. Negative SRS in the alloy was observed when the strain rate increased from  $10^0 s^{-1}$  to  $10^2 s^{-1}$  due to the activation of DSA. The XRD patterns evidenced that the initial austenitic matrix remained stable after deformation under different strain rate conditions with no twinning or phase transformation. Therefore, the underlying

reason for the effect of DSA on negative SRS was attributed to the variation in the dislocation density [54].

The mechanical properties of Fe–19Cr–8Ni–0.14C and Fe–19Cr–8Ni–0.05C metastable austenitic steels were studied by Ogawa et al. with a focus on the effects of solute carbon concentration [55]. Both the alloys exhibited transformation-induced plasticity (TRIP). Owing to the increase in austenite stability offered by excess amount of carbon, the former alloy exhibited lower transformability. However, the TRIP and DSA had a synergistic effect that boosted the work hardening capability (Figure 2). Due to the fcc to bcc transformation, DSA was observed in the alloy at higher strains. This was attributed to the higher diffusivity characteristic of the bcc phase in comparison to the fcc (austenitic) phase. Although the transformation rate per strain was reduced by carbon addition, the addition of carbon to the bcc-martensite resulted in an increase in its hardening capability per unit volume. This enhancement was attributed to the combined effects of dislocation pinning and solution hardening caused by the carbon atmosphere. On the other hand, the low carbon steel, owing to its high transformation rate per strain, exhibited rapid work hardening. [55].

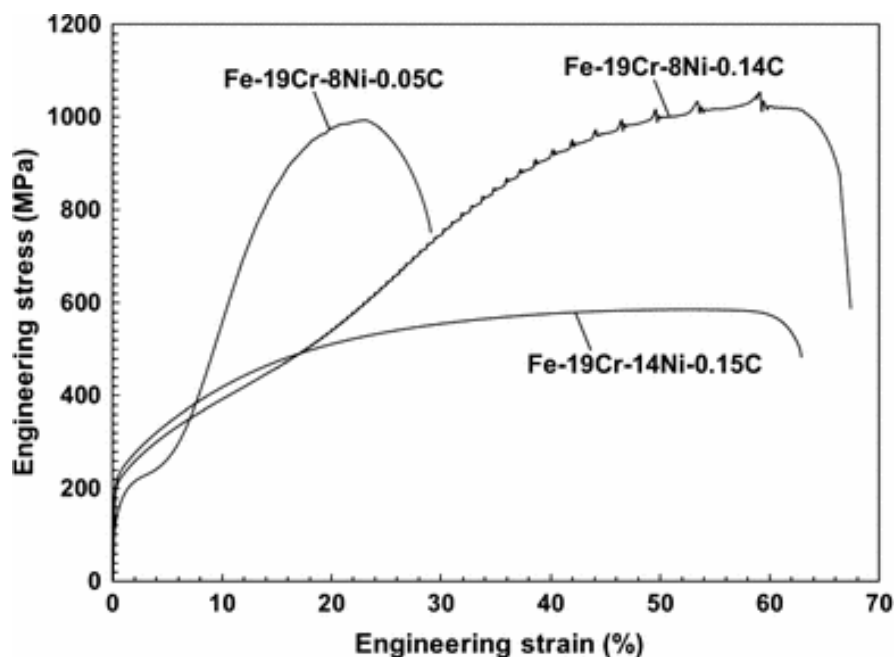


Figure 2 Stress–strain curves of different steels with varying carbon and nickel compositions at a strain rate of 0.0001/s [55].

Similar study on Fe–17Mn–0.6C and Fe–17Mn–0.8C Twinning Induced Plasticity (TWIP) steels was given by Koyama and coworkers [56], who showed that the serrations in the stress strain curves were due to DSA. The experimental studies showed that deformation twins were observed throughout the temperature range while the serrations were only observed at certain temperature range only which shows that the serrations in the plastic flow were not because of the twins but due to the activation of DSA [56], and this has also been highlighted by a previous work by Nemat Nasser et al., on CP-Ti as discussed before [43].

The influence of DSA on microstructural evolution for 800H alloy was studied by Cao et al [57]. They carried out hot compression tests within a wide temperature range (723 K – 1173 K) and strain rate range of  $0.001\text{s}^{-1} - 1\text{s}^{-1}$ . DSA in Alloy 800 H is speculated to originate from the pipe diffusion of substitutional solutes (i.e., Cr, Ni, and Ti). TEM characterization revealed that as the deformation temperature increased, the linear microstructure at about 1023 K tends to slip along certain planes because dislocations move along those planes (see Figure 3a and b). The authors also reported similar findings for 253MA stainless steel [58]. These flat structures can get in the way of the movement of dislocations, which makes the material harder and the strain is likely to be concentrated along the most active slip planes due to the pinning effect of solute atoms on the mobile dislocations [59]. This revealed that the interaction between solute atoms and dislocations restrict the movement of dislocations. Moreover, the cross-slip tendency was found to be constrained by the presence of pinning sites along the dislocations, thereby promoting planar slip mode and resulting in a linear microstructure. [60, 61].

Li et al. studied quasi-static tensile properties of Hastelloy X (HX), which is a Ni-Cr-Fe-Mo alloy fabricated through Laser Powder Bed Fusion (LPBF), in the temperature range of  $22^{\circ}\text{C} - 800^{\circ}\text{C}$  and strain rate of  $10^{-4}-10^{-2}\text{s}^{-1}$  and compared it with the commercial alloy. The LPBF HX alloy showed DSA in the temperature range of  $300^{\circ}\text{C} - 600^{\circ}\text{C}$  which was reported to be lower than that of the commercial alloy showing DSA after  $600^{\circ}\text{C}$ . The underlying reason was the low activation energy and high dislocation density in which the LPBF alloy, which facilitated the diffusion of solute atoms along dislocation cores at lower temperatures [62].

## 2.1. Thermomechanical Models

Numerous works demonstrate experimental, constitutive modelling and FE simulations of metals and alloys under thermomechanical loading conditions [11, 15-20]. As previously discussed, various numerical models have reportedly predicted the metallic response to thermomechanical tests including the Johnson Cook (JC) model [22], Zerilli Armstrong (ZA) Model [25], Nemat Nasser Model [24], Preston-Tonks-Wallace (PTW) [23], and Voyiadjis-Abed (VA) model. It has been mentioned before that the activation of dynamic strain aging is significantly influenced by the metallic structure, resulting in variations in temperature and strain rate range across different metals and alloys. Within this particular framework, a number of numerical models have been formulated with the aim of covering dynamic strain aging phenomena. These models are either tailored for a particular metal or alloy or have been modified from previous thermomechanical models to accommodate a broader range of metals and alloys [26, 29, 30, 63].

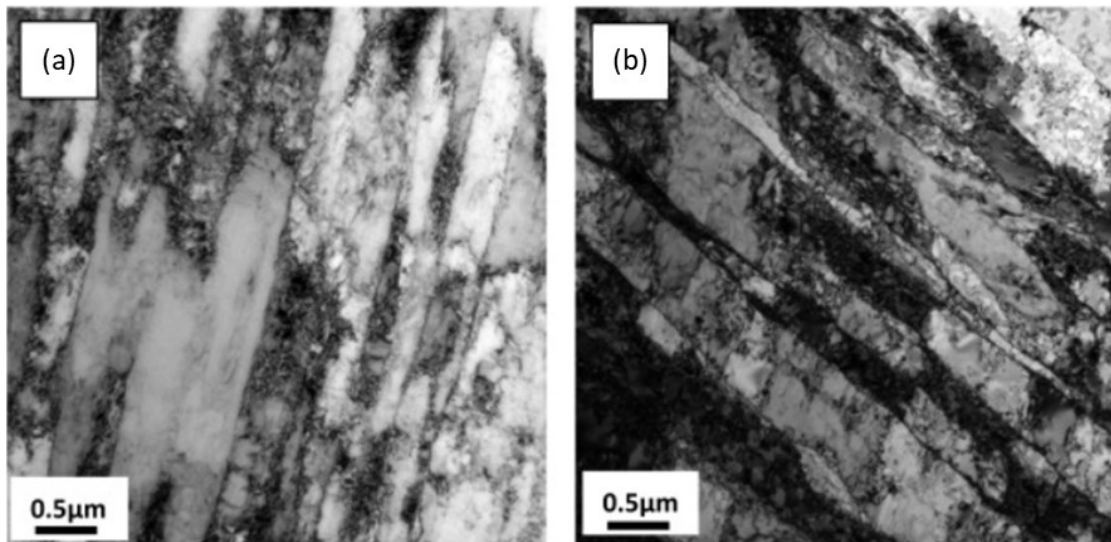


Figure 3 TEM images 800H alloy samples at 1023 K temperature and true strain of 0.2 strain deformed with a strain rate of (a) 0.1/s, and (b) 0.01/s [57].

For instance, JC model was modified by Sindhura to predict dynamic strain aging in commercially pure titanium [31]. A second order polynomial was introduced that was coupled with work hardening, strain rate, and thermal softening features of CP-Ti. Likewise, Devotta et al., performed a second order polynomial fitting to the JC model

and modified it to capture DSA in C45E steel (Figure 4) [32]. Comparing numerical models to experimental data revealed a high degree of coherence.

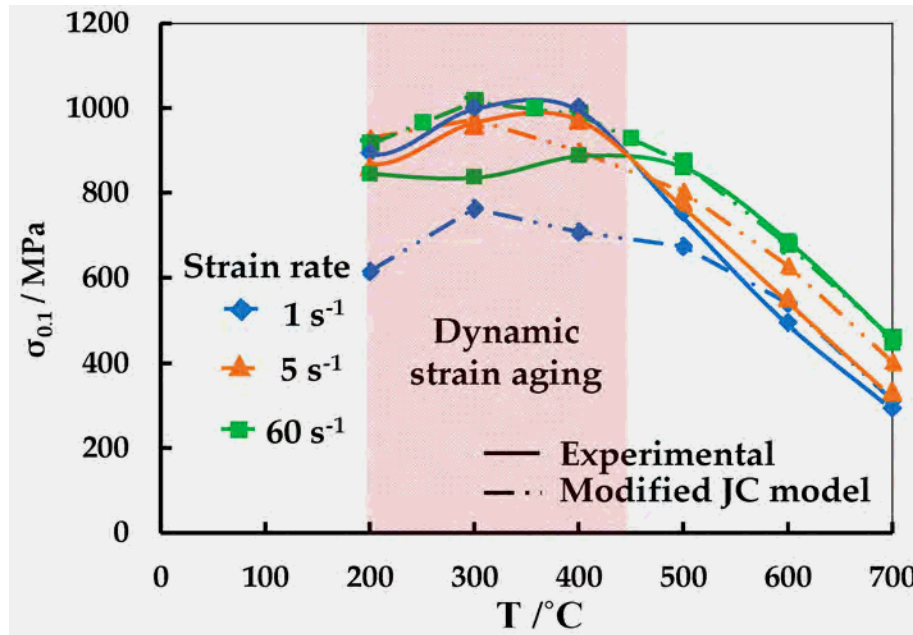


Figure 4. Stress vs Temperature profile at different strain rates for C45E steel [32].

Similarly, DSA activation was captured by Steven and Sheng by modifying the dimensionless Preston-Tonks-Wallace (PTW) model for 1045 steel [30]. An empirical Gaussian function that was dependent on strain rate was introduced to the PTW model, based on the bell-shaped curve of stress vs temperature plot during DSA. Song and coworkers adopted a similar approach by modifying the VA model using a Weibull probability distribution function (PDF) to capture dynamic strain aging in Nb [64], CP-Ti [28], Inconel 718 [42], and C45 steel [27]. The VA model, which is a physical model, has the capability to estimate the thermomechanical flow stress across a broad range of strain rates and temperatures. However, the modification implemented in this study was derived from the observation of a bell-shaped curve during dynamic strain aging when plotting flow stress vs. temperature. Nevertheless, as indicated by multiple studies, the activation of DSA is contingent upon a specific configuration of temperature and strain rate and remain inactive in other scenarios. Hence, employing a probability or gaussian function as a means to capture DSA may not be deemed as a persuasive approach.

A physical parameter based modification was developed by Cheng and Nasser in the Nemat-Nasser and Li model [65] to predict dynamic strain aging in CP-Ti [4]. The modification was developed by considering the relationship between the thermal activation energy and the threshold yield stress with respect to the impurity concentration along the line of dislocation which implicitly relies on the diffusion parameters [4]. Physical parameters were considered while implementing the modification, and the model results exhibited a high degree of similarity to the experimental data. However, the model's applicability is restricted solely to higher strain rates [43]. In contrast, as previously stated, the VA model is a constitutive model that relies on physical parameters. It is capable of encompassing a wide range of temperatures and strain rates, ranging from 0.001/s to 8300/s [15]. Hence, the current study develops a modification, based on diffusion kinetics and physical parameters, to the constitutive VA model in order to effectively capture dynamic strain aging.

The VA model depends on various microstructural parameters, including the dislocation density, thermal activation energy, dislocation velocity, and Burgers vector etc. Although the model has been previously employed for estimating the thermomechanical behavior of various metals and alloys, its applicability to the phenomenon of DSA has not been evaluated. [8, 12, 14]. The primary cause can be attributed to the absence of thermal activation parameters that adequately consider the interactions between impurities and dislocations in the context of dynamic strain aging. Hence, the model demonstrates suitable results in scenarios where the metals do not exhibit DSA. According to Cheng and Nasser, the activation of DSA leads to the diffusion of impurity atoms into the dislocation core via pipe diffusion, resulting in their interaction with the dislocations [43]. These interactions lead to a deceleration in the dislocation's motion through the surrounding obstacles, resulting in a macroscopic increase in the metal's strength. [4].

Furthermore, the extent of the interaction is directly influenced by the concentration of impurity atoms. As the temperature increases, there is a corresponding increase in the concentration of impurities along the dislocation line until it reaches a state of saturation. The thermal activation parameter for the combination of temperature and strain rate during DSA is determined by the diffusion kinetics of these impurities.

This work introduces a modification to the VA model based on the diffusion kinetics and impurity concentration along dislocations, in order to capture DSA in various metals and alloys. Section 2.3 details the development of the constitutive VA model while the modification follows later.

## **2.2. FE Models**

Finite Element Modelling has been carried out based on the numerical modelling approaches adopted to capture DSA in multiple studies [66-70]. S. Serajzadeh and H. Sheikh utilized a combination of two-dimensional FE analysis, neural network models and stream function models, to investigate the thermo-mechanical characteristics involved in the process of hot strip rolling of AA5083. [67]. The velocity field and stream functions were initially determined utilizing the principles of volume constancy and the upper bound theorem. Subsequently, the temperature field across the metal was determined by employing the two-dimension conduction-convection approach. An artificial neural network model was employed for analysis of flow stress and its strain, strain rate and temperature dependencies. Two models were created, one for regular flow, and the other for serrated flow exhibiting DSA. The validity of the FE model was demonstrated by a good agreement between the model predictions and the experimental data [67].

In a recent study conducted by Friedrich et al., orthogonal cutting experiments were simulated using a novel material model specifically designed for AISI 1045 steel. This model incorporated the time-dependent plastic response that arises from interrupted austenite transformation during short heating periods. [68]. The new model included complex strain hardening and DSA effects, resulting in improved alignment with experimental observations under high cutting speeds. The results were also compared with the fundamental JC model (Figure 5) [68]. The simulations were performed using DEFORM v12.0.1 for three material modelling conditions i.e., JC, m-PTW-0, and m-PTW-1. Thermophysical properties, such as Young's modulus, thermal conductivity, density, and heat capacity were determined by CalPhad method using JMatPro V11 software. These were then transferred into DEFORM software as a temperature dependent function [68].

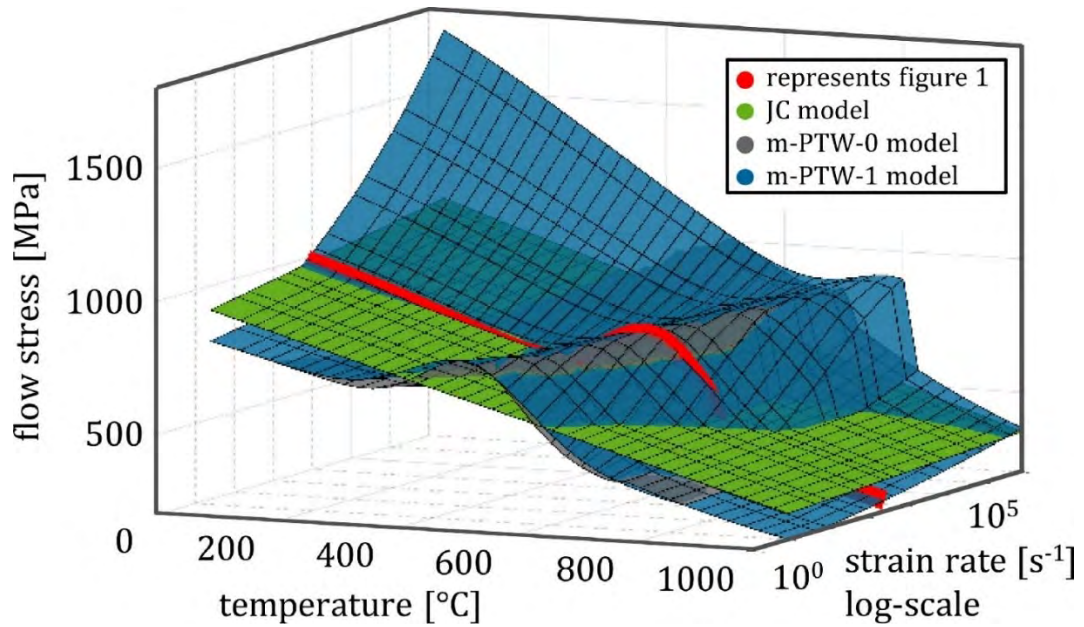


Figure 5 Isothermal flow stress at different temperature and strain rates at a plastic strain of 0.1 for experimental data, JC and modified PTW models [68].

DSA behavior was studied for a supersaturated age-hardenable aluminum alloy in the temperature range of (298 K – 508 K) and strain rate range of (0.0001/s – 0.05/s) by Anjabin et al [70]. Two mechanisms i.e., dynamic precipitation and the pinning of mobile dislocations by the solute atoms were attributed to DSA in the applied loading conditions. Both mechanisms were investigated using physically based material modelling and experimental approaches. The constitutive formulation was incorporated into the widely used FE software ABAQUS/Explicit as a user defined VUMAT subroutine. This allowed for the simulation of the material's flow behaviour under iso-thermal uniaxial tensile testing conditions. The model effectively predicted the experimental stress-strain curves, serrations, and possible jerky flow (Figure 6) [70].

Song and coworkers performed theoretical investigations on the thermomechanical properties of Martensitic Microcomposite Formable Steel (MMFX) alloy for strain rates from 0.0015/s to 500/s and a broad temperatures range (Room temperature to 923 K) [69]. The constitutive VA model was modified using a probability distribution function to capture DSA and an FE code was developed related to the modified model by writing a user defined subroutine. The comparison of the developed FE results with the experimental data (Figure 7), it was revealed that in the activation region of

DSA the VA model did not work effectively while the DSA-induced hardening was successfully captured by their proposed model and FE code [69]. However as discussed before, their model was developed using a PDF function which does not account for the diffusion phenomenon.

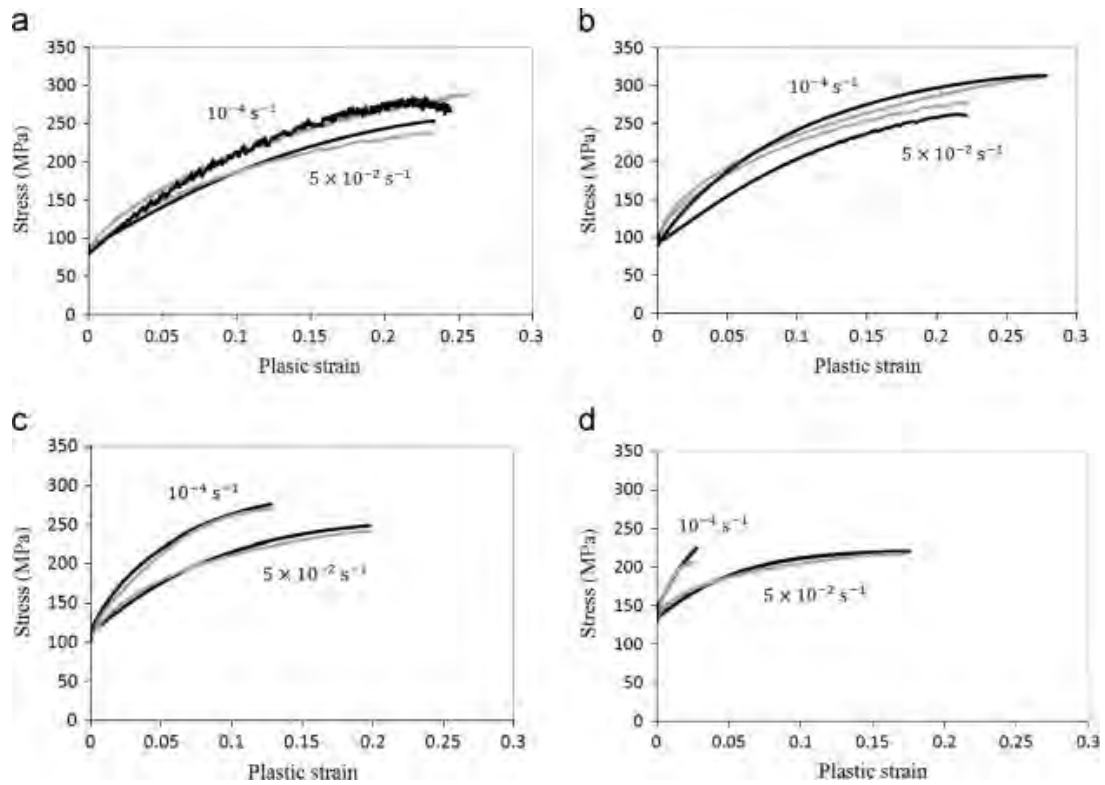


Figure 6 Comparison between the experimental data (grey) and the model predicted flow stress curves (black) (a) 298 K, (b) 388 K, (c) 458 K, and (d) 508 K [70].

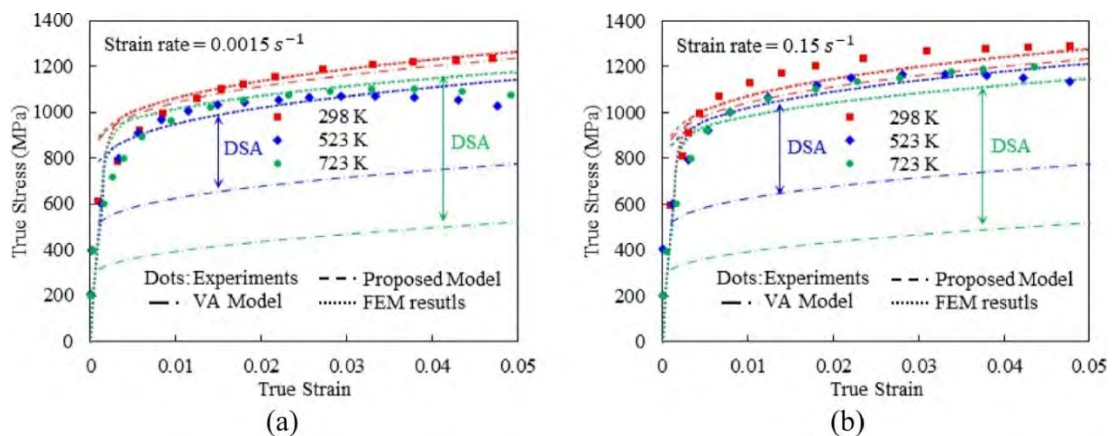


Figure 7 Comparison of the experimental data with predicted stress-strain curves for the VA model, the modified VA model, and the FE results at different temperatures and a strain rate of (a) 0.0015/s, and (b) 0.15/s [69].

With the user-defined VUMAT subroutine, this dissertation includes numerical models that are based on the developed constitutive model. But the application focuses on predicting temperature ranges for dynamic strain aging at a given strain rate based on how solute atoms diffuse through the material and how they interact with dislocations. The numerical results are discussed and compared to the experimental data and the results of the constitutive models. The case studies use different metals and alloys and use experimental data from literature. Moreover, real-time numerical problems are analyzed within the activation regions of DSA. Simulations are carried out for studying necking and shearing during the activation of DSA.

### 2.3. Voyiadjis-Abed (VA) Constitutive Model

The constitutive VA model was initially developed for pure metals of the same type of crystal structures [8, 9]. Later, they redefined the model for steel and other alloys, based on physical quantities [10-15, 20]. When a metal is deformed plastically, the movement of dislocations is hindered by obstacles that results in an increase in strength. These obstacles can either be short or long ranged. Since plasticity is a function of dislocation movement through both these short- and long-range barriers, both have their own contribution to the total flow stress. Based on this fact, the VA model was developed by decomposing the flow stress of the material into athermal stress ( $\sigma_{ath}$ ) and thermal stress ( $\sigma_{th}$ ) [8, 9] components as shown by Eqn. (1):

$$\sigma = \sigma_{ath} + \sigma_{th} \quad (1)$$

During plastic deformation the strength is determined based on the dislocation interaction within the crystal structure. The movement mechanisms of these dislocations have been extensively discussed by Orowan [71] who related the plastic shear strain rate ( $\dot{\epsilon}_p$ ) with burger vector ( $b$ ), mobile dislocation density ( $\rho_m$ ), and the average dislocation velocity ( $v$ ) as given in Eqn.(2).

$$\dot{\epsilon}_p = \bar{m}b\rho_mv \quad (2)$$

Where  $\bar{m}$  is the Schmidt orientation factor. Eqn. (3) describes the relation between average dislocation velocity and the thermal activation energy to overcome local

obstacles. Kocks et al [72] related the activation energy ( $G$ ) to the flow stress ( $\sigma$ ) and the thermal flow stress ( $\sigma_{th}$ ) and the shape of the dislocations. (Eqn. (4)) and Eqn. (5) discusses the evolution of mobile dislocation density.

$$v = v_0 e^{(-G/kT)} \quad (3)$$

Here  $v_0$  is the reference velocity of dislocations defined as  $v_0 = d/t_w$ .  $d$  is the average distance between obstacles that is covered by dislocations movement,  $k$  is the Boltzmann's constant and  $T$  is the temperature. The activation energy defined by Kocks et al. is given as:

$$G = G_0(1 - (\sigma/\sigma_{th})^q)^p \quad (4)$$

In Eqn. (4),  $G_0$  is the Gibb's free energy at absolute zero temperature, while the constants  $p$  and  $q$  define the shape of the short-range barrier. The value range for  $p$  is 0 to 1, while it is 1 to 2 for  $q$ . The mobile dislocation density evolution is given as:

$$d\rho_m/d\varepsilon_p = M - k_a(\rho - \rho_i) \quad (5)$$

Here  $\varepsilon_p$  is the plastic strain,  $M$  is the dislocation multiplication factor which is defined as  $M = 1/bl$ , where  $l$  is the free path length for trapped dislocations. The factor  $k_a$  is responsible for dislocation annihilation that depends on strain rate and temperature and  $\rho_i$  is the dislocation density that already existed in the material initially. All these equations are utilized in defining the different physical parameters of the VA model.

### 2.3.1. For bcc metals

As previously mentioned, plasticity in a metal refers to the phenomenon of dislocation flow through long-range and short-range obstacles. The VA model is formulated based on these two phenomena and is divided into the athermal stress ( $\sigma_{ath}$ ) component and the thermal stress ( $\sigma_{th}$ ) component, respectively [8, 9] as given by Eqn. (1). The athermal stress ( $\sigma_{ath}$ ) for bcc metals is defined as:

$$\sigma_{ath} = Y_a + B\varepsilon_p^n \quad (6)$$

In Eqn. (6), the athermal yield strength ( $Y_a$ ) is the strength of metal in the absence of plastic deformation, and it is insensitive to temperature. Similarly, the hardening constants ( $B$  and  $n$ ) remain unaffected by temperature and therefore contribute to the athermal stress component. The plastic strain during deformation is represented by  $\varepsilon_p$ .

For bcc metals, the thermal stress ( $\sigma_{th}$ ) component is described in Eqn. (7) as:

$$\sigma_{th} = \hat{\sigma} \left( 1 - (\beta T)^{\frac{1}{q}} \right)^{\frac{1}{p}} \quad (7)$$

Where  $\hat{\sigma}$  is the minimum threshold stress yield stress needed to overcome the Peierl's barrier at 0 K temperature. T represents the working temperature while the thermal activation parameter ( $\beta$ ) is determined by Eqn. (8) as:

$$\beta = \beta_1 - \beta_2 \ln \varepsilon_p \quad (8)$$

The values of  $\beta_1$  and  $\beta_2$  are influenced by the thermal activation energy ( $G_o$ ), and the Boltzmann's constant ( $k$ ), while ,  $\beta_1$  also depends on the mobile dislocation density ( $\rho_m$ ), the reference dislocation velocity ( $v_o$ ), burgers vector ( $b$ ), and the Schmidt orientation factor ( $\bar{m}$ ) as indicated in equations (9) and (10).

$$\beta_1 = \frac{k}{G_o} \ln(\dot{\varepsilon}_{po}^i) = \frac{k}{G_o} \ln(\bar{m} b v_o \rho_m) \quad (9)$$

$$\beta_2 = \frac{k}{G_o} \quad (10)$$

In Eqn. (9),  $\dot{\varepsilon}_{po}^i$  represents the initial reference strain rate which depends on  $v_o$ , and is defined as  $d/t_w$ . The constitutive VA model for bcc metals can be obtained by rearranging Eqn. (1) in the light of equations (6), (7), and (8) as:

$$\sigma = \underbrace{Y_a + B \varepsilon_p^n}_{\text{athermal stress}} + \underbrace{\hat{\sigma} \left( 1 - (\beta_1 T - \beta_2 T \ln \varepsilon_p)^{\frac{1}{q}} \right)^{\frac{1}{p}}}_{\text{thermal stress}} \quad (11)$$

It is pertinent to mention here that the thermal stress component given in Eqn. (11) should always be positive. This means that in case of a negative value, due to increase

in temperature beyond the critical temperature ( $T_{cr}$ ), the terms inside the bracket in thermal stress must be set equal to 0. Accordingly, the critical temperature is defined in Eqn. (12) as:

$$T_{cr} = (\beta_1 - \beta_2 \ln(\dot{\epsilon}_p))^{-1} \quad (12)$$

Figure 8 shows an example of the utilization of VA model for bcc metals to predict the thermomechanical response of Tantalum [9]. It can be observed that the hardening remains unaffected by the changes in temperature while the yield point is influenced by changes in temperature. Hence the thermal part of VA model for bcc metals comprises of thermal yielding only, as shown in Eqn. (11). The works by Abed et al. [8-10] provide further details on the physical dependence of material parameters indicated in Eqn. (11).

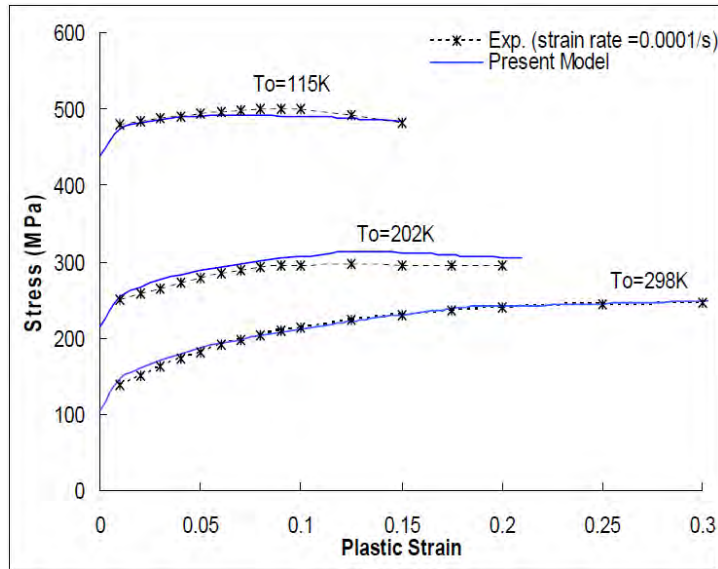


Figure 8 Comparison of the VA model for bcc metal (Tantalum) with the experimental data [9]

### 2.3.2. For fcc metals

Unlike bcc metals, the athermal flow stress of fcc metals is composed of just the yield strength ( $Y_a$ ). It means that there is no contributions from temperature and strain rates on the yield strength of the metal and hence it is nearly constant for all the ranges of strain rates and temperatures. On the other hand, the thermal stress component is described by thermal hardening behavior as follows:

$$\sigma_{th} = B\varepsilon_p^n \left( 1 - (\beta_1 T - \beta_2 T \ln \dot{\varepsilon}_p)^{\frac{1}{q}} \right)^{\frac{1}{p}} \quad (13)$$

Thermal stress parameter shows the strong dependence of temperature and strain rates on the plastic flow stress of fcc metals, while yield point remains temperature insensitive. For Eqn. (13), the definition of different parameters given is the same as for Eqn. (11). Eqn. (13) can be utilized to rewrite the complete form of VA model for fcc metals as given by Eqn. (14):

$$\sigma = \underbrace{Y_g}_{\text{athermal stress}} + \underbrace{B\varepsilon_p^n \left( 1 - (\beta_1 T - \beta_2 T \ln \dot{\varepsilon}_p)^{\frac{1}{q}} \right)^{\frac{1}{p}}}_{\text{thermal stress}} \quad (14)$$

Figure 9 compares the VA model (Eqn. (14)) results for fcc metal OFHC-copper with the experimental data [9].

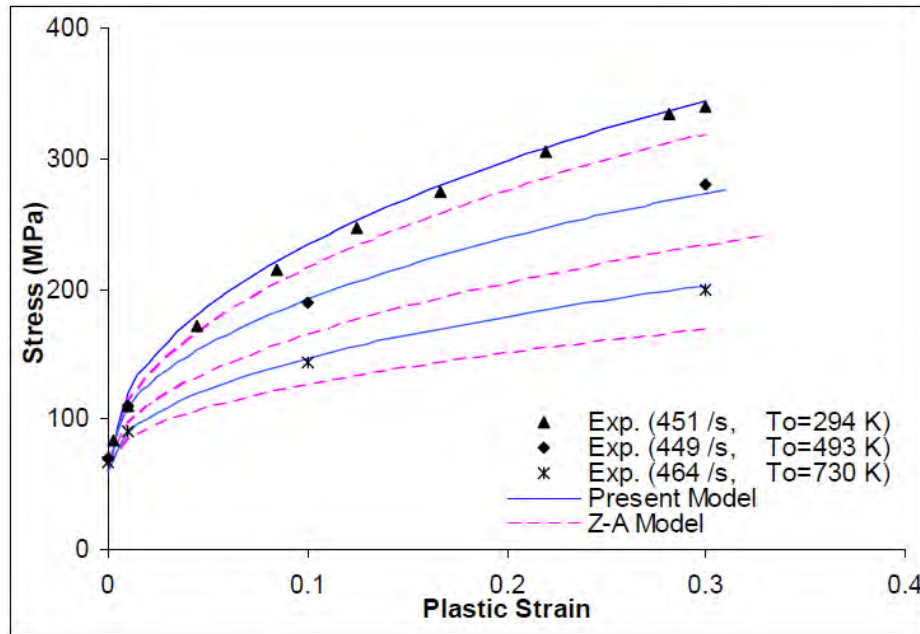


Figure 9 Comparison of the VA model for fcc metal (Oxygen-free high thermal conductivity (OFHC) copper) with the experimental data [9]

It can be observed that for fcc metals, the yielding remains unaffected by the changes in temperature while the metal hardening shows variation with changes in temperature. Hence the thermal part of VA model for fcc metals comprises of thermal hardening only as indicated by Eqn. (14).

### 2.3.3. For hcp metals

The hcp metals flow stress is decomposed into three components i.e., athermal stress, thermal yielding, and thermal hardening. These are defined in Eqn. (15) as follows:

$$\sigma = \underbrace{Y_a + B_1 \varepsilon_p^{n_1}}_{\text{athermal stress}} + \underbrace{\hat{\sigma} \left( 1 - (\beta^Y T)^{\frac{1}{q}} \right)^{\frac{1}{p}}}_{\text{thermal yielding}} + \underbrace{B_2 \varepsilon_p^{n_2} \left( 1 - (\beta^H T)^{\frac{1}{q}} \right)^{\frac{1}{p}}}_{\text{thermal hardening}} \quad (15)$$

As discussed before, metals typically experience a decline in their mechanical strength as temperature rises, until a specific threshold temperature is attained. Beyond this, only the athermal stress component remains while the thermal stress component diminishes. In Eqn. (15), the athermal yield stress ( $Y_a$ ) and the athermal hardening component ( $B_1$  and  $n_1$ ) comprise of the athermal stress component. The thermal hardening components are represented by  $B_2$  and  $n_2$ .  $\beta$  follows the same definition given for bcc and fcc metals in Eqn. (9) and (10). The superscripts Y and H correspond to the phenomena of yielding and hardening, respectively. The comprehensive form of VA model for metals having hcp crystal structure is given in Eqn. (16) as:

$$\sigma = \underbrace{Y_a + B_1 \varepsilon_p^{n_1}}_{\text{athermal stress}} + \underbrace{\hat{\sigma} \left( 1 - (\beta_1^Y T - \beta_2^Y T \ln \dot{\varepsilon}_p)^{\frac{1}{q}} \right)^{\frac{1}{p}}}_{\text{thermal yielding stress}} + \underbrace{B_2 \varepsilon_p^{n_2} \left( 1 - (\beta_1^H T - \beta_2^H T \ln \dot{\varepsilon}_p)^{\frac{1}{q}} \right)^{\frac{1}{p}}}_{\text{thermal hardening stress}} \quad (16)$$

Voyiadjis and Abed have reported the utilization of Eqn. (16) for both isothermal and adiabatic deformation, with the former being suitable for low strain rates and the latter for high strain rates [8]. Figure 10 shows the existence of both thermal yielding and thermal hardening in commercially pure Ti (CP-Ti) which is in an hcp metal. The VA model results capture thermal yielding and thermal hardening effectively in the DSA inactive region. However, as can be seen by the comparison of curve for 296 K and 473 K, the model could not capture the stress increase due to DSA [8], which necessitates the need of modification in the VA model to incorporate the activation of DSA.

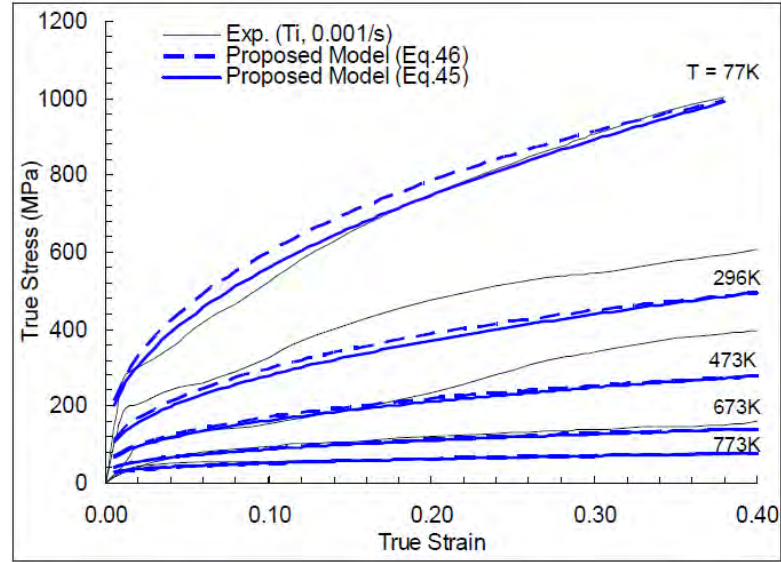


Figure 10 Comparison of the VA model results for hcp metals with the experimental data for commercially pure titanium [8]

#### 2.3.4. For alloys

Most of the alloys are made up of a combination of bcc, fcc and hcp metals. In this context, the model developed for alloys contains the features of all of these types of crystal structures. As previously discussed, the stress in the constitutive VA model (given in Eqn. (1)) is decomposed into athermal and thermal stress components. Eqn. (17) defines the athermal stress component as:

$$\sigma_{ath} = Y_a + B_1 \epsilon_p^{n_1} \quad (17)$$

In bcc metals, the process of hardening is primarily influenced by Peierls barriers, which are of short-range and remains relatively unaffected by variations in temperature and strain rate under applied stress. Conversely, in fcc metals, the deformation mechanism is attributed to the formation and expansion of heterogeneous dislocation microstructures, as well as the occurrence of long-range intersections between dislocations [8]. In the case of alloys, data collected from experiments suggests that plastic deformation is influenced by the short ranged Peierls barriers, the dislocation-dislocation interactions over long range, as well as the short-range interactions between dislocations and solute atoms. Or in simple words, it can be inferred that temperature and strain rates have an impact on both yield stress and

strain hardening. Consequently, it was deduced that, in addition to the athermal hardening present in the alloy, thermal hardening is also a contributing factor. The observed phenomenon can be ascribed to the incorporation of various alloying elements possessing bcc, fcc and hcp crystal structures. Therefore, the thermal stress component comprises of thermal yielding and thermal hardening component, as indicated by Eqn. (18):

$$\sigma_{th} = \underbrace{\hat{\sigma} \left( 1 - (\beta_1^Y T - \beta_2^Y T \ln \varepsilon_p)^{\frac{1}{q}} \right)^{\frac{1}{p}}}_{\text{thermal yielding stress}} + \underbrace{B_2 \varepsilon_p^{n_2} \left( 1 - (\beta_1^H T - \beta_2^H T \ln \varepsilon_p)^{\frac{1}{q}} \right)^{\frac{1}{p}}}_{\text{thermal hardening stress}} \quad (18)$$

Although  $\beta_1^i$  and  $\beta_2^i$  (where  $i$  is  $Y$  for yielding and  $H$  for hardening) have the same definition for both yielding and hardening phenomena, their physical interpretations are quite different. For instance, the thermal activation energy  $G_o$  varies between both of them due to their association with two distinct mechanisms which results in different values for the parameters  $\beta_2^Y$  and  $\beta_2^H$ .  $\beta_1^Y$  is found based on the initial values of the microstructural quantities ( $l$ ,  $\rho_f$ , and  $\rho_m$ ). In contrast, the evaluation of  $\beta_1^H$  relies on the average values of these quantities that are obtained during material hardening phase. Since taking the average values does not give very accurate results for  $\beta_1^H$  as it changes with  $\varepsilon_p$ , one possible approach to address this issue is by employing Orwan's relation to establish the definition of  $\beta_1^H$ . This assumes a relation between the forest dislocations and  $\varepsilon_p$  as given in Eqn. (19):

$$\beta_1^H = \frac{k}{G_o} \ln \left( \frac{v_o \varepsilon_p}{1 - \frac{\tilde{m} l \lambda_1}{b} + \lambda_2 \varepsilon_p + l \lambda_3 \lambda_4 \varepsilon_p^{0.5}} \right) \quad (19)$$

Here the constant coefficients  $\lambda_1$ ,  $\lambda_2$ ,  $\lambda_3$  and  $\lambda_4$  are indicative of various phenomena related to mobile dislocations.  $\lambda_1$  represents the multiplication of mobile dislocations,  $\lambda_2$  signifies their mutual trapping & annihilation,  $\lambda_3$  denotes their immobilization through interaction with forest dislocations, and  $\lambda_4$  characterizes the dynamic recovery process [15]. Despite the relationship between  $\beta_1^H$  with  $\varepsilon_p$  introduces a higher level of accuracy, it significantly complicates the flow stress relation, particularly when attempting to fit the model to experimental data. Hence, it is more

practical to use Eqn. (9) as it has demonstrated a highly accurate approximation in several previous works by Abed and coworkers [9, 10, 15].

By substituting equations (17) and (18) in equation (1), the comprehensive form of the VA model for alloys can be derived as:

$$\sigma = \underbrace{Y_a + B_1 \varepsilon_p^{n_1}}_{\text{athermal stress}} + \underbrace{\hat{\sigma} \left( 1 - (\beta_1^Y T - \beta_2^Y T \ln \dot{\varepsilon}_p)^{\frac{1}{q}} \right)^{\frac{1}{p}}}_{\text{thermal yeilding}} + \underbrace{B_2 \varepsilon_p^{n_2} \left( 1 - (\beta_1^H T - \beta_2^H T \ln \dot{\varepsilon}_p)^{\frac{1}{q}} \right)^{\frac{1}{p}}}_{\text{thermal hardening}} \quad (20)$$

The constitutive VA model, given in Eqn. (20) was used to predict the thermomechanical response of the Al-6XN stainless steel alloy in isothermal and adiabatic heating conditions [15]. The experimental data reveals the influence of temperature on both the yielding and hardening phenomena (Figure 11). This was efficiently captured by the VA model for alloys owing to the inclusion of thermal yielding and thermal hardening components given in Eqn. (20).

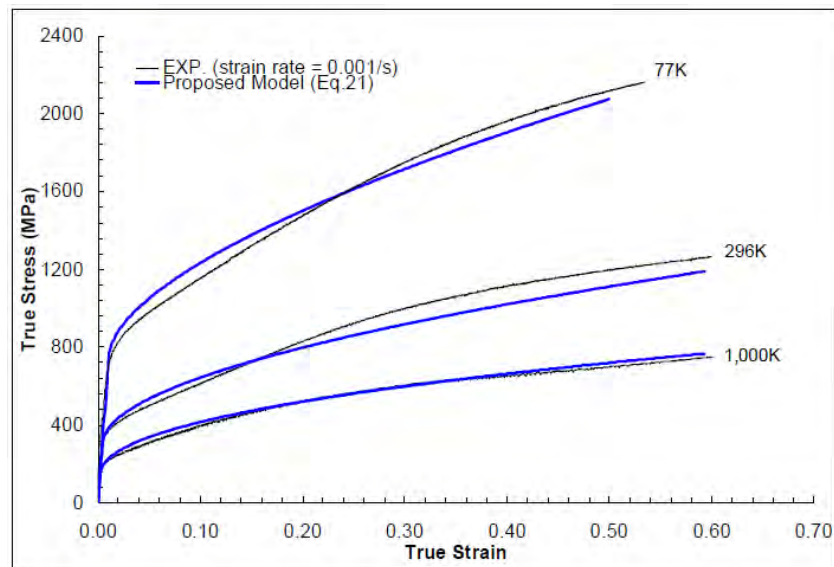


Figure 11 True Stress-True Strain curves for Al-6XN stainless alloy showing both thermal yeilding and thermal hardening phenomena. Blue lines indicate the VA model for alloys given in Eqn. (20) [15].

Equation (20) encompasses both athermal and thermal mechanisms in the determination of the strain hardening parameters B and n. As previously discussed, the different parameters given in the constitutive VA model (Eqn. (20)) are physical in nature and further details are available in the works authored by Abed and coworkers [10-15].

#### 2.4. Adiabatic Heating at Very High Strain Rates

At low strain rates, the material behaves isothermally but when the strain rates are very high, there is not enough time for the material to radiate the heat generated due to deformation into the environment and behaves adiabatically. In the context of isothermal analysis, T refers to the initial temperature ( $T_0$ ). However, in case of higher strain rates, the material undergoes plastic deformation, resulting in the generation of heat. Therefore, at high strain rates, adiabatic temperature is determined to account for the generated heat using Eqn. (21) [73].

$$T = T_0 + \frac{\zeta}{c_p \rho} \int_0^{\varepsilon_p} \sigma d\varepsilon_p \quad (21)$$

Here,  $\zeta$  represents the Taylor-Quinney coefficient,  $c_p$  denotes the specific heat at constant pressure and  $\rho$  represents the density of the material.

#### 2.5. Damage Model

As discussed before, when a material is subjected to stress induced plasticity, it deforms permanently. Upon further plastic deformation beyond the ultimate stress point, the material loses its capability to bear more stress. This phenomenon of decreased mechanical properties in the material, commonly referred to as damage, is closely associated with the microstructural characteristics of the material and has been documented in numerous studies [21, 33-41]. Damage in the material was analyzed by Lemaitre and Chaboche on the basis of micro voids and cracks present within the microstructure of the material. They introduced a damage parameter  $\phi$  that serves to quantify the amount of damage present within the material. The parameter  $\phi$  is assigned a value of 0 in the absence of damage, indicating a plastically undamaged material. Conversely, a value of 1 is assigned to  $\phi$  when the material undergoes damage resulting in the fracture of the material. The typical range for the critical

value of this damage parameter is generally observed to be within the range of 0.2 to 0.8. [39].

Numerous works have been reported on development of numerical models related to damage in a material [36, 37, 40, 41]. Most of them are either limited to a single material or are empirical in nature. However, a simple damage model was presented by Abed and coworkers that is founded on the idea that materials sustain damage proportional to the amount of energy they take in as they deform [17, 21, 35, 38]. The model is referred to as the energy-based damage model, which quantifies a material's ability to accumulate damage by utilizing the area under the stress-strain curve. Once the maximum capacity is reached, a state of failure will follow. Equation (22) characterizes the extent of damage in the material at a given point ( $\varphi_p$ ) as:

$$\varphi_p = \varphi_f \left( \frac{U_p}{U_T} \right)^n \quad (22)$$

Here  $\varphi_f$  represents the level of damage at the point of failure, which is determined through the utilization of SEM images to assess the density of micro cracks at the fracture site. The parameter  $n$  corresponds to the damage exponent associated with displacement.  $U_p$  denotes the amount of energy stored within the material at a given location, while  $U_T$  represents the total energy absorbed by the material prior to failure. The energy is calculated by evaluating the integral of the stress with respect to strain, as expressed in equation (23):

$$U = \int_0^{\varepsilon_p} \sigma d\varepsilon \quad (23)$$

After assessing the damage parameter, the effective flow stress is determined by utilizing equation (24), that relates the damaged ( $\sigma_d$ ) and undamaged ( $\sigma_{ud}$ ) flow stress of the material.

$$\sigma_d = \sigma_{ud}(1 - \varphi_p) \quad (24)$$

Contemplating the literature studied, this dissertation aims to develop a physically constitutive model that highlights the role of diffusion kinetics of impurities/solute atoms and their interactions with the dislocations that results in the activation of DSA. The objective is achieved by introducing an additional expression to the VA model given in Eqn. (39) and Eqn. (40) to capture dynamic strain aging. In addition, the

modified constitutive VA model incorporates the effect of damage evolution by utilizing the relationship between the flow stress of damaged and undamaged materials given in Eqn. (24). Moreover, the developed constitutive model is implemented in FE software (ABAQUS) using VUMAT subroutine. Later, the FE simulation and constitutive model results are compared with the experimental works available in the literature. A detailed discussion on the constitutive model development and research methodologies is given in the next chapter.

## Chapter 3. Research Methodology

The research methodology is partitioned into two different yet interconnected components:

### 3.1. Theoretical/Constitutive Model Development

As discussed before, the constitutive model to capture DSA was developed by modifying the VA model. In this dissertation, three different approaches were adapted to capture DSA in metals and alloys. The first approach was based on utilizing a second-degree polynomial to capture the increase in strength due to dislocation pinning by solute atoms.

The second approach was based on the work reported by Nasser et al. [4] where the authors related the concentration of solute/impurity atoms with reference Gibbs free energy ( $G_o$ ). This approach was used to find that the value of  $G_o$  does not remain constant during the activation of DSA.

The third approach which was mainly utilized and published in different articles was based on the diffusion parameters and kinetics of the solute/impurity atoms present inside the metals or alloys. The diffusion constants of these atoms help in predicting the right combination of temperature and strain rate that activates DSA. Hence, this approach is recommended to be used for modelling and prediction of DSA in metals and alloys.

#### 3.1.1. The first approach

As discussed by Abed et al. [10], DSA occur when the waiting time is equal to the aging time of the dislocations that are trapped by solute atoms leading to the increase in the obstacle strength by certain amount. DSA can occur through a directional diffusion of the dislocation core atmosphere at high strain rates, or through a bulk diffusion at low strain rates [10]. This means that the interaction between dislocations and solute atoms can be considered as short-range interaction. Since those dislocation-solute interactions are short range interactions, and because those types of interactions

are controlled by the thermal stress component of the VA model as described earlier, then the DSA mechanism can be incorporated into that component of the model.

As defined earlier, the thermal component consists of thermal yielding and thermal hardening terms. The thermal yielding component does not depend on the accumulation of the dislocation densities during the plastic deformation but rather on the initial quantities of dislocations that are supplied due to yielding or already existing in the material from the manufacturing process. Therefore, the thermal yielding stress component is related to the stresses at zero plastic strain. Accordingly, the model shown by Eqn. (20) reduces to the relation shown by Eqn. (25) at zero plastic strain:

$$\sigma = Y_a + \hat{\sigma} \left( 1 - (\beta^Y T)^{\frac{1}{q}} \right)^{\frac{1}{p}} \quad (25)$$

Rearranging the equation to get Eqn. (26), it can be written such that:

$$(\sigma - Y_a)^P = \hat{\sigma}^P - \hat{\sigma}^P (\beta^Y)^{\frac{1}{q}} (T)^{\frac{1}{q}} \quad (26)$$

In the absence of DSA,  $(\sigma - Y_a)^P$  is related to  $(T)^{\frac{1}{q}}$  by a linear relationship in the form of  $y = b - mx$  where  $x = (T)^{\frac{1}{q}}$ ,  $m = \hat{\sigma}^P (\beta^Y)^{\frac{1}{q}}$ , and  $b = \hat{\sigma}^P$ . This can be clearly proven as shown by Figure 12. However, in the case of DSA, the relation does not follow a linear trend but rather a 2nd order polynomial in the form of  $y = ax^2 + bx + C$  for different strain rates as shown by Figure 12. In abstract terms, the additional term  $ax^2$  is basically a higher order temperature term of the form  $(\gamma^Y T^2)^{\frac{1}{q}}$  and the constant term  $C$  is no longer equivalent to  $\hat{Y}^P$ , but rather it is of the form  $C = \omega \hat{Y}^P$ . The parameters  $\omega$  and  $\gamma$  are proposed to capture the DSA mechanism where ( $\omega$ ) can be thought of as a strain rate sensitivity factor that converges to 1 in the absence of DSA, and  $\gamma$  is the coefficient of the higher order temperature term which vanishes since  $\gamma$  converges to zero in the absence of DSA. The term  $\gamma$  is defined in the same manner as  $\beta$  because it is proposed to take care of the dislocation-solute atoms interaction and it will be a function of the density of pinned dislocations due to their interaction with solute atoms. In other words,  $\gamma^Y$  and  $\omega^Y$  are defined as shown by Eqns. (27) and (28):

$$\gamma^Y = \gamma_1^Y - \gamma_2^Y \ln \dot{\epsilon}_p \quad (27)$$

$$\omega^Y = \left( \frac{\dot{\epsilon}}{\dot{\epsilon}_0} \right)^{m_Y} \quad (28)$$

where  $\gamma_1^Y$  and  $\gamma_2^Y$  terms can be defined to be of the same format to that of  $\beta_1^Y$  and  $\beta_2^Y$  terms. In other words, they can be defined to be of the same exact expression in Eqns. (9) and (10). However, the physical interpretation of  $\gamma_j^Y$  is different than that of  $\beta_j^Y$ . The terms  $\gamma_j^Y$  is dependent on the initial quantities of dislocations that are pinned by solute atoms only because the increase in strength is due to those dislocations at this range of temperatures and strain rates. Therefore, this additional term shall take care of this additional strength that is introduced into the material and will vanish in the absence of DSA.

Following the exact same approach by plotting the thermal hardening term at any value of plastic strain against  $(T)^{\frac{1}{q}}$ , the thermal hardening term can be found to follow the same trend by fitting a 2nd order polynomial in the presence of DSA. Therefore, the thermal hardening term is also modified by introducing  $\gamma^H$  and  $\omega^H$  where they are described in similar manner to that shown by Eqns. (27) and (28). They are described to be as shown by Eqns. (29) and (30):

$$\gamma^H = \gamma_1^H - \gamma_2^H \ln \dot{\epsilon}_p \quad (29)$$

$$\omega^H = \left( \frac{\dot{\epsilon}}{\dot{\epsilon}_0} \right)^{m_H} \quad (30)$$

By introducing those physical based modifications to the model, the model is now capable of capturing the dynamic strain aging in steel alloys such as C45 steel. By combining the aforementioned equations and introducing those modifications into Eqn. (20), the new format of the model is described as shown by Eqn. (31):

$$\begin{aligned} \sigma_{VA} = & Y_a + B_1 \epsilon_p^{n_1} + \hat{\sigma} \left( \omega^Y - (\beta^Y T)^{\frac{1}{q}} - (\gamma^Y T^2)^{\frac{1}{q}} \right)^{\frac{1}{p}} \\ & + B_2 \epsilon_p^{n_2} \left( \omega^H - (\beta^H T)^{\frac{1}{q}} - (\gamma^H T^2)^{\frac{1}{q}} \right)^{\frac{1}{p}} \end{aligned} \quad (31)$$

In the case of no DSA, the new terms  $\omega^i$  and  $\gamma^i$  will converge to one and zero, respectively reducing the relation to its format shown by Eqn. (20). Therefore, the model is modified to introduce a higher order temperature term that captures the interaction between dislocations and solute atoms, and to introduce a strain rate sensitivity parameter to capture the effect of strain rate on yielding and hardening parameters. Those parameters will not be strain-rate sensitive in the absence of DSA, and for that this rate sensitivity parameter will converge to one.

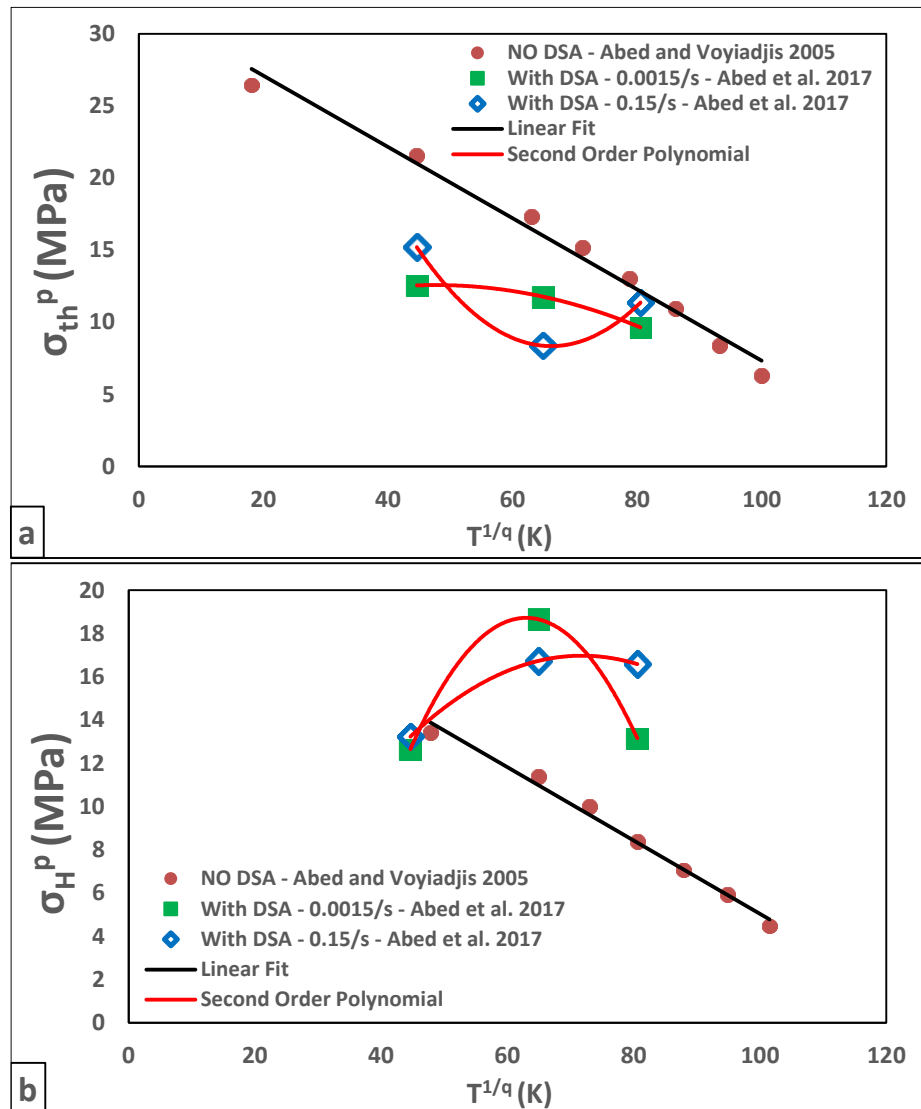


Figure 12: The experimental values of a) Thermal Yielding Stress and b) Thermal Hardening Stress against temperature for the cases of DSA absence [8, 9], and with the presence of DSA at different strain rates for C45 steel [21].

However, this approach was not studied further in detail as it deviated from the main goal of dissertation which is to develop a constitutive model based on physical and

microstructural parameters. Moreover, the approach was empirical in nature and hence was not utilized further.

### **3.1.2. The second approach**

The VA model is completely composed of terms that capture the mechanisms for dislocation interactions as well as the thermal activation processes and is consequently interpreted in terms of microstructural based physical quantities. However, in previous studies, the effect of increase in the solute concentration during the event of activation of DSA was not considered. As defined earlier, DSA is basically a sudden increase in strength due to pinning of dislocations by the solute atoms and restricting their mobility until enough stresses (thermal or mechanical) are exerted to make those dislocations overcome those barriers and restore their mobility. A schematic representation for the diffusion and interactions of solute atoms and the dislocation is given in Figure 13.

In a crystal lattice, the solute atoms are located at the interstitial sites available. They are under constant stress due to limited space available. However, since they do not have any other space in the lattice, the interstitial vacancies are the most suitable place for them. But whenever there is a more suitable space available, the solute atoms will diffuse into that space to release their stresses. When a mechanical stress is applied to the material, the bonds between the atoms break causing a slip in the system (Figure 13(a)). While the new bonds are formed, there is also formation of extra half planes known as dislocations.

During this plastic deformation, the solute atoms diffuse into the available free space adjacent around the dislocation (Figure 13(b)) [74]. This diffusion of solutes into the newly available sites increase the solute concentration at those locations which reduces the solute entropy at these sites. In other words, the driving force for solute diffusion to pin down dislocations becomes dominated by the enthalpy of mixing. Hence, this interaction of the solute atoms and the dislocations results in an increase in the overall activation energy. For further deformation, the stress applied must be increased to overcome this new barrier formed which results in an increase in the strength of the material.

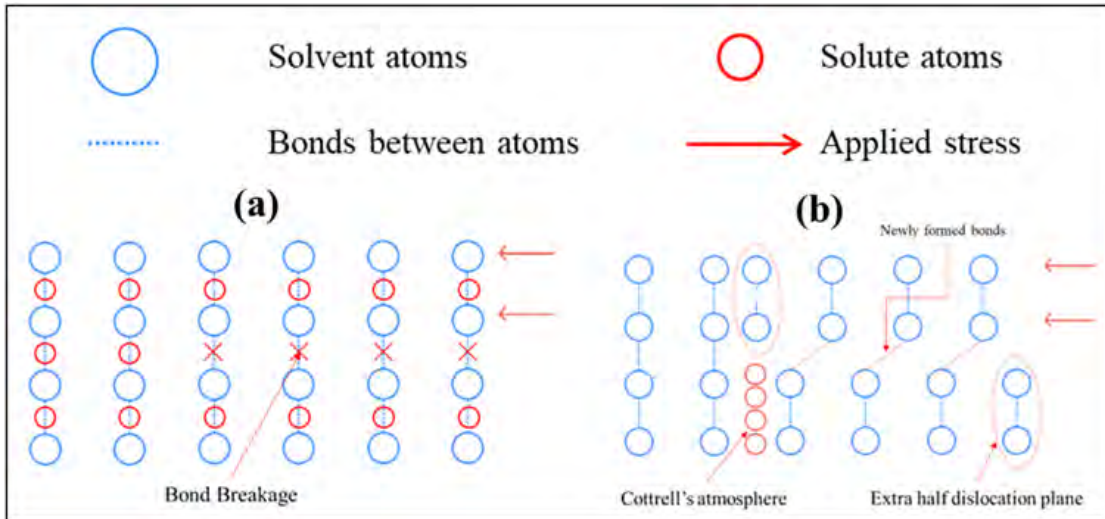


Figure 13 Schematics for the development of solute atmosphere and interactions with dislocations where (a) shows the bond breakage under applied stress thus causing slippage in the structure and (b) shows the formation of dislocation pinning and the Cottrell's atmosphere.

As discussed by Abed et al. [10], DSA occur when the waiting time is equal to the aging time of the dislocations that are trapped by solute atoms leading to the increase in the obstacle strength by certain amount. The dislocation velocity depends on this waiting time [8] and gets increased during DSA due to diffusion of solutes, which can either occur through a directional diffusion of the dislocation core atmosphere at high strain rates, or through a bulk diffusion at low strain rates [10]. Since those dislocation-solute interactions are short range interactions, and because those types of interactions are controlled by the thermal stress component of the VA model as described earlier, the DSA mechanism must be a part of the thermal component of the model.

Cheng and coworkers [4] demonstrated the relationship of  $G_o$  with the binding free energy ( $G_B$ ) per unit length as follows:

$$G_o \propto \sqrt{G_B G_D} w \quad (32)$$

In equation (32), ( $G_D$ ) is the free energy per unit length of dislocation that is independent of the presence of solute atoms, and  $w$  is the trough's effective width that was utilized by the authors in their numerical model for DSA. It was also reported that  $G_B$  is proportional to the product of solute atoms concentration ( $C$ ) along the

dislocation line and the strength of interaction for each solute atoms ( $G_{BO}$ ) [4] and shown here in Eqn. (33).

$$G_B \propto G_{BO}C \quad (33)$$

Eqns. (32) and (33) signifies the impact of change in the concentration of solute atoms at the barriers and their interaction with the dislocations on the binding free energy which indirectly affects the activation free energy ( $G_O$ ). During an event of DSA, solute concentration increases significantly at the local obstacles that pins the dislocation and restricts their movement. Therefore, a much higher activation energy is required for the movement of dislocations through these obstacles. Hence, a jump in strength is observed during DSA.

Later, with a further increase in the temperature, the solute atoms distribute them in the matrix that results in the loss of strength. In other words, increase in entropy of the solute atoms becomes the driving force to release the pinned dislocations which accounts for the decrease in strength of the metal.

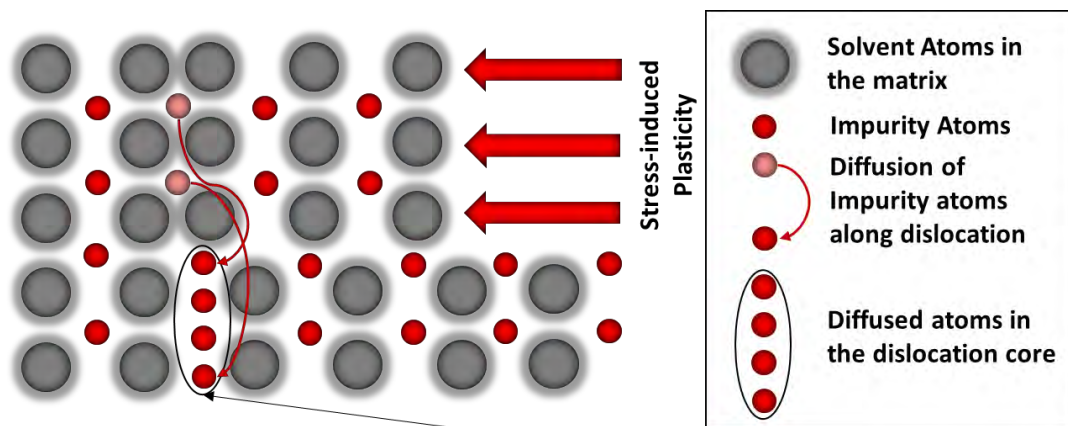
However, this approach was not found useful at a later stage as the model could not predict the combination of temperature and strain rates for activation of DSA. Moreover, too much fluctuation in the energy was also not a good approach as it was more of a data fitting approach and was not satisfactory for unknown data sets.

### **3.1.3. The third approach**

Metal deformation under stress occurs due to its inherent ductility. This phenomenon is characterized by the discontinuous movement of dislocations. When stress is applied, the metal undergoes plastic deformation, during which, there is movement of dislocations. These dislocations interact with various obstacles, that act as a barrier to their movement. While they are waiting at the obstacles, the solute atoms that are trapped in the matrix find a space where they can diffuse along the dislocation line and lower their energy. These diffused solute atoms interact with the dislocations and result in their pinning. This increases the dislocation waiting time, which leads to the activation of DSA. As discussed before, DSA appears when this waiting time becomes equal to the solute diffusion time. Contemplating above, an additional expression is introduced into the VA model based on different parameters such as

diffusion time, dislocations waiting time, and diffusion energy etc. Moreover, the dislocation motion, solute atom interactions, and thermal activation energy etc. are considered in the development of the constitutive model.

As previously discussed, DSA is initiated by the interactions occurring between dislocations and the diffusing impurities. The phenomenon described can be attributed to the localized dislocation pinning due to the diffusion of impurities or solute atoms [4]. In the context of metal deformation, it is commonly observed that the ductile nature of metals leads to the occurrence of shearing within their structure. Dislocations exhibit a discontinuous movement pattern along the loading direction, stopping at each obstacle for a specific duration called the waiting time. It exhibits a continuous mobility after successfully overcoming each obstacle, followed by waiting upon encountering the subsequent obstacle. This leads to the occurrence of strain hardening within the metal. Nevertheless, as the temperature rises, the impurities that were previously positioned within the interstitial sites begin to undergo diffusion, moving into the vacant areas along the dislocation lines (see Figure 14).



**Higher impurity concentration along the dislocation line that results in pinning**

Figure 14 Schematic representation of impurity interaction with the dislocations. The mobile dislocations pin due to impurities diffusion along the dislocation line.

The presence of impurities initiates interactions with dislocations, thereby impeding their mobility as they encounter local obstacles. This leads to an increase in the dislocation waiting time and dynamic strain aging activates when this waiting period reaches the threshold of the relaxation time required for impurity diffusion across the average obstacle width [42].

The schematic depicted in Figure 14 illustrates the presence of impurities such as hydrogen, carbon, nitrogen, and oxygen, positioned at the interstitial sites owing to the comparatively smaller size. The impurities experience continuous stress due to restricted space and exhibit a tendency to diffuse towards larger areas whenever accessible. Microstructural defects, including vacancies, voids, and dislocations, will always occur in metallic structures when subjected to stress due to the shearing of atomic planes. These structural imperfections facilitate the impurity diffusion within the matrix. As a result, a high degree of diffusion is exhibited by the impurities into the core of dislocations, leading to the initiation of dynamic strain aging. It is important to note that the kinetics of impurity diffusion vary depending on the type of impurity, with each impurity exhibiting a distinct combination of temperature and strain rate for diffusion.

Contemplating above, the proposed work involves the modification of the constitutive VA model to effectively capture DSA activation in metals and alloys. As previously mentioned, dislocations exhibit discrete motion and stop at each obstacle encountered during the process of plastic deformation. Nevertheless, as a result of the presence of diffusing atoms in the process of dynamic strain aging, the average duration of dislocation waiting ( $t_w$ ) at obstacles equals the impurity diffusion relaxation time ( $t_d$ ) across the average obstacles width [28]. According to Nasser et al. [43], the following equation is provided:

$$t_d = \frac{(a')^2}{D} \quad (34)$$

In Eqn. (34),  $a'$  denotes the mean distance of dislocation which is estimated to be approximately 3 times the value of  $b$ , where  $b$  represents the burgers vector. The diffusion coefficient ( $D$ ) is described as:

$$D = D_0 \exp\left(-\frac{Q_d}{kT}\right) \quad (35)$$

In Eqn. (35), the diffusion constant ( $D_0$ ) and the diffusion activation energy ( $Q_d$ ) are material specific and varies with the type of solute and solvent atoms. The average spacing between dislocations ( $d$ ) divided by the reference velocity of dislocation ( $v_0$ ) defines the average waiting time of dislocations as given in equation (36) as:

$$t_w = \frac{d}{v_0} \quad (36)$$

Summarizing above, the diffusion strain rate ( $\dot{\epsilon}_{DSA}$ ) of impurities/solutes during DSA is defined in Eqn. (37), using equations (9), (34) and (36) as:

$$\dot{\epsilon}_{DSA} = \frac{D\bar{m}b\rho_m d}{(a')^2} \quad (37)$$

The enhanced diffusion of solute atoms along the line of dislocations results in the interactions between the dislocations and the solute atoms. This implies that the rate at which diffusion occurs is positively correlated with temperature, resulting in a corresponding increase in the impurity concentration ( $C$ ) along the dislocation line. The ratio of impurity concentration ( $C/C_S$ ) is a significant factor in characterizing the stress vs temperature profile during the activation of DSA. Here  $C_S$  represents the saturated impurity concentration. The impurity ratio primarily influences the stress increment during DSA.

Furthermore, it is important to note that the initial temperature for activation of DSA is dependent upon the strain rate employed and the kinetics of diffusion governing the interaction between solute and solvent metal. The activation of DSA at low temperatures is only possible at low strain rates as the solute atoms have enough time to diffuse, despite the slower diffusion kinetics at low temperatures. Conversely, when strain rates are increased, the diffusion kinetics become significant only at elevated temperatures, as the strain rate applied prevents the diffusion mechanism from overcoming plastic deformation at lower temperatures. Therefore, it can be observed that the activation of DSA at higher strain rates is more pronounced at elevated temperatures. The dynamic strain aging strain rate given in equation (37) is employed to define the additional stress term ( $\sigma_{DSA}$ ) which accounts for capturing the increase in stress due to DSA:

$$\sigma_{DSA} = \sigma'_{DSA} \left( \frac{C}{C_S} \right) \left( 1 - (\beta_{DSA} T - \beta_2 T \ln \dot{\epsilon}_p)^{\frac{1}{q}} \right)^{\frac{1}{p}} \quad (38)$$

The definition of  $\beta_{DSA}$  in equation (38), which is the thermal activation parameter related to DSA follows the same definition given in Eqn. (9). The difference is the

usage of DSA strain rate ( $\dot{\epsilon}_{DSA}$ ), as a substitute to  $\dot{\epsilon}_{p0}^i$  to calculate the thermal activation parameter.  $\sigma'_{DSA}$  represents the type of stress contributing to the activation of DSA. It can be thermal yielding ( $\hat{\sigma}$ ), thermal hardening ( $B_2\epsilon_p^{n_2}$ ), or a combination of both ( $\hat{\sigma} + B_2\epsilon_p^{n_2}$ ). The addition of  $\sigma_{DSA}$  in the constitutive VA model equation is intended to account for dynamic strain aging. The resulting modified constitutive VA model is given in Eqn. (39) for bcc, Eqn. (40) for hcp and alloys as:

$$\sigma = \underbrace{Y_a + B\epsilon_p^n}_{\text{athermal stress}} + \underbrace{\hat{\sigma} \left( 1 - (\beta_1 T - \beta_2 T \ln \epsilon_p)^{\frac{1}{q}} \right)^{\frac{1}{p}}}_{\text{thermal yielding stress}} + \underbrace{\sigma'_{DSA} \left( \frac{C}{C_S} \right) \left( 1 - (\beta_{DSA} T - \beta_2 T \ln \epsilon_p)^{\frac{1}{q}} \right)^{\frac{1}{p}}}_{\text{DSA stress}} \quad (39)$$

$$\sigma = \underbrace{Y_a + B_1\epsilon_p^{n_1}}_{\text{athermal stress}} + \underbrace{\hat{\sigma} \left( 1 - (\beta_1^Y T - \beta_2^Y T \ln \epsilon_p)^{\frac{1}{q}} \right)^{\frac{1}{p}}}_{\text{thermal yielding stress}} + \underbrace{B_2\epsilon_p^{n_2} \left( 1 - (\beta_1^H T - \beta_2^H T \ln \epsilon_p)^{\frac{1}{q}} \right)^{\frac{1}{p}}}_{\text{thermal hardening stress}} + \underbrace{\sigma'_{DSA} \left( \frac{C}{C_S} \right) \left( 1 - (\beta_{DSA} T - \beta_2 T \ln \epsilon_p)^{\frac{1}{q}} \right)^{\frac{1}{p}}}_{\text{DSA stress}} \quad (40)$$

The modification proposed contributes only when the combination of temperature and strain rates responsible for activation of DSA is present and does not provide any contribution otherwise. Furthermore, it should be noted that the concentration ratio exhibits a positive correlation with temperature, reaching a point of saturation beyond which any further increase in temperature does not result in a corresponding increase in the concentration ratio.

#### 3.1.4. Model parameter evaluation

This section gives a brief overview to find the model parameters given in Eqn. (39). With increase in temperature, the metal loses its strength until a certain critical

temperature ( $T_{cr}$ ) is reached. Beyond this temperature, the metal becomes insensitive to temperature, and the athermal stress ( $\sigma_{ath}$ ) parameters are calculated at this temperature. The yield strength of the metal is first calculated using the 0.2% offset method. Afterwards, the strain hardening parameters are identified using a non-linear fit. Once these parameters are found, they are subtracted from the experimental flow stress and the thermal yielding component is calculated at zero plastic strain. The parameters  $p$  and  $q$  are selected from the range mentioned before. A linear fit between  $(\sigma_{th})^p$  and  $(T)^{1/q}$  gives the value for the threshold yield stress parameter ( $\hat{\sigma}$ ) at the intercept and the slope gives the value for  $(\beta^i)^{1/q}$ . Note that only the temperatures that do not show the activation of DSA are used in finding these parameters. Once the thermal yielding component is defined, the thermal hardening component is calculated in the same way by subtracting all the calculated parameters from the experimental data.  $\beta_{DSA}$  is found using the material constants from literature.

### **3.2. FE Modelling**

The proposed constitutive model was applied in ABAQUS which is a commercially available finite element software. This implementation aims to assess the activation of dynamic strain aging (DSA) under different thermomechanical loading scenarios thus validating the applicability of the proposed model for diverse types of metals and alloys. However, the acquisition of experimental results is necessary for the purpose of parameter identification in models, and to effectively facilitate numerical simulations using FEM it is important to provide a precise depiction of thermomechanical loading. This includes the consideration of various factors such as temperature, strain rate, diffusion kinetics, and deformation etc.

As discussed earlier, the experimental findings for different metals/alloys show that metals behave differently with change in temperature owing to the distinct crystal structure. Moreover, the strain rate plays a major role in determining the process (i.e., isothermal, or adiabatic). Therefore, the viscoplastic model must account for the coupled effect of temperature and strain rates.

As previously stated, metals exhibit different inelastic deformation mechanisms, that is, athermal and thermal deformation mechanism. Based on the applied strain rate, the

yield stress function can be static or dynamic. In case of a very low strain rate, the material behaves isothermally and has enough time to dissipate out the heat, generated during deformation, into the environment. Therefore, the static yield functions are used. On the contrary, the dynamic yield stress is of utmost importance in characterizing the material behaviour and is commonly utilized in FE codes for dynamic problems with high strain rates.

Abed developed microstructure-based formulations for the static and dynamic yield functions, utilizing the von Mises yield criterion [75]. The yield function for metals is generalized by:

$$f = \sigma_{eq} - \sigma_{ath} - \sigma_v^{th}(\dot{\epsilon}, T) - \sigma_{DSA}(\dot{\epsilon}_{DSA}, T) \quad (41)$$

Here  $\sigma_{ath}$  represents the athermal stress component which depends on the athermal yield stress ( $Y_a$ ) and athermal hardening stress ( $B\varepsilon^n$ ).  $\sigma_v^{th}(\dot{\epsilon}, T)$  represents the thermal visco-stress while the last part of Eqn. (41) is the yield dependant DSA component that shows the coupled effect of solute/dislocation interactions based on the diffusion kinetics of the solute atoms and temperature. The equivalent stress  $\sigma_{eq}$  is determined by the von Mises yield criterion as given in Eqn.(42):

$$\sigma_{eq} = \left( \frac{3}{2} (\tau_{ij})(\tau_{ij}) \right)^{1/2} \quad (42)$$

Eqn. (43) defines the deviatoric normal stress ( $\tau_{ij}$ ) as:

$$\tau_{ij} = \sigma_{ij} - \frac{1}{3} \sigma_{mm} \delta_{ij} \quad (43)$$

Here  $\sigma_{mm}$  represents the hydrostatic component of stress while  $\delta_{ij}$  represents the Kronecker delta. The thermal stress component ( $\sigma_v^{th}(\dot{\epsilon}, T)$ ) carries the same definition given in Eqn. (7) while the DSA stress component is defined in the same manner as given in Eqn. (38).

Under static loading conditions, when the strain rate ( $\dot{\epsilon}$ ) is very low ( $\dot{\epsilon} \leq \dot{\epsilon}_s$ ), the thermal component of the yield stress is determined by the temperature whereas the impact of the strain rate is negligible. Hence, the elastoplastic deformation transitions into isothermal loading scenario and relies on the initial temperature ( $T_0$ ). The static

yield function (Eqn. (41)) becomes rate independent and is redefined after setting the strain rate equal to the static strain rate ( $\dot{\epsilon} = \dot{\epsilon}_s$ ) by combining Eqns. (6), (7) and (38) with Eqn. (41) as given in Eqn. (44):

$$f_s = \sigma_{eq} - \underbrace{(Y_a + B\epsilon_p^n)}_{\sigma_{ath}} - \underbrace{\hat{\sigma} \left(1 - (\beta T)^{\frac{1}{q}}\right)^{\frac{1}{p}}}_{\sigma_v^{th}(\dot{\epsilon}, T)} - \underbrace{\sigma'_{DSA} \left(\frac{c}{c_s}\right) \left(1 - (\beta_{DSA} T - \beta_2 T \ln \dot{\epsilon}_p)^{\frac{1}{q}}\right)^{\frac{1}{p}}}_{\sigma_{DSA}(\dot{\epsilon}_{DSA}, T)} \text{ for } \dot{\epsilon}_p \leq \dot{\epsilon}_s \quad (44)$$

However, the effect of DSA even at this strain rate depends on the applied strain rate. As discussed before, the temperature range for DSA increases with strain rate. Likewise, at a very low strain rate, the temperature range shifts towards lower temperature value [76]. Within the framework of classical elasto-plastic theory, the static yield function serves to differentiate between the elastic and inelastic deformation states. Moreover, it can be employed to differentiate between the dynamic and static inelastic states of deformation as given in Eqn. (45):

$$\begin{aligned} f_s < 0 &\rightarrow \text{static elastic state} \\ f_s = 0 &\rightarrow \text{static plastic state} \\ f_s > 0 &\rightarrow \text{dynamic plastic state} \end{aligned} \quad (45)$$

It has been discussed before that when the temperature increases beyond the critical temperature ( $T_{cr}$ ), the flow stress becomes insensitive to temperature but remains sensitive to the applied strain rate. Moreover, this critical temperature increases with strain rate. However, in case of static deformation, the critical temperature remains same and aligns with the static strain rate [77]. Upon exceeding the critical temperature, the yield function defined in Eqn. (44) becomes:

$$f_{ath} = \sigma_{eq} - (Y_a + B\epsilon_p^n) \quad (46)$$

In Eqn. (46), the athermal yield function ( $f_{ath}$ ) is rate-independent which is referred to as the lower limit function. This limit indicates the maximum degradation of flow stress due to increase in temperature. This athermal yield function is also used to differentiate between the athermal and thermal states as given in Eqn. (47):

$$f_{ath} \leq 0 \rightarrow \text{athermal state}$$

$$f_{ath} > 0 \rightarrow \text{thermal state} \quad (47)$$

In case of dynamic loading conditions i.e.  $\dot{\epsilon} > \dot{\epsilon}_s$ , the coupled effect of strain rate and temperature is incorporated through the thermal component of the yield stress and the dynamic yield function ( $f_d$ ) is defined as given in Eqn. (48):

$$f_d = \sigma_{eq} - \underbrace{(Y_a + B\epsilon_p^n)}_{\sigma_{ath}} - \underbrace{\hat{\sigma} \left( 1 - (\beta_1 T - \beta_2 T \ln \dot{\epsilon}_p / \dot{\epsilon}_s)^{\frac{1}{q}} \right)^{\frac{1}{p}}}_{\sigma_v^{th}(\dot{\epsilon}, T)} -$$

$$\underbrace{\sigma'_{DSA} \left( \frac{C}{C_s} \right) \left( 1 - (\beta_{DSA} T - \beta_2 T \ln \dot{\epsilon}_p)^{\frac{1}{q}} \right)^{\frac{1}{p}}}_{\sigma_{DSA}(\dot{\epsilon}_{DSA}, T)} \text{ for } \dot{\epsilon}_p > \dot{\epsilon}_s \quad (48)$$

In adiabatic condition, due to the accumulation of dislocation at higher strain rates (dynamic loading), the metal gets stiffer and a higher stress is needed for the dislocations to overcome the obstacles and hence the dynamic yield surface expands until it reaches a maximum value ( $f_{max}$ ), also known as the upper limit function defined in Eqn. (49) as:

$$f_{max} = \sigma_{eq} - (Y_a + B\epsilon_p^n) - \hat{\sigma} \quad (49)$$

$\hat{\sigma}$  here defines the threshold yield stress which is the highest visco-stress at a very high strain rate ( $\dot{\epsilon}_p = \dot{\epsilon}_{po}^i$ ). This threshold stress can also be achieved at zero kelvin temperature value, which indicates a very high viscosity in the metal. Hence, the upper limit function ( $f_{max}$ ) differentiates between the acceptable and unacceptable states as given in Eqn. (50):

$$f_{max} < 0 \rightarrow \text{acceptable state}$$

$$f_{max} \geq 0 \rightarrow \text{inacceptable state} \quad (50)$$

Moreover, the accumulation of dislocations at such high strain rates in acceptable deformation state leads to adiabatic heat generation, which increases with plastic strain, thus reducing the viscosity of the metal. This results in material softening, which reduces the dynamic yield surface until a lower limit (Eqn. (46)) is reached where the evolved temperature approaches to the critical temperature.

Subsequently, it is necessary to establish an accurate measurement of the amplitude of the viscoplastic flow to accurately describe the material's dynamic behaviour. In this context, the viscoplastic multiplier ( $\dot{\lambda}^{vp}$ ) is defined for the von Mises plasticity using the Perzyna model for the rate independent yield function ( $f_s$ ) and the Consistency model for the dynamic yield function ( $f_d$ ).

The Perzyna model incorporates viscoplasticity by utilizing the overstress relation proposed by Perzyna. The primary characteristic of this model is that the yield function utilized to describe the viscoplastic strain can exceed zero, which is referred to as 'overstress'. The magnitude of the viscoplastic flow, as shown by the viscoplastic multiplier ( $\dot{\lambda}^{vp}$ ), varies directly by a nonlinear relationship with the overstress ( $\varphi$ ).

$$\dot{\lambda}^{vp} = \frac{\langle \varphi(f_s) \rangle}{\eta^{vp}} \quad (51)$$

In Eqn. (51), the viscosity parameter, denoted as  $\eta^{vp}$ , represents the relaxation time. The McCauly brackets, denoted as  $\langle \cdot \rangle$ , are defined as  $\langle x \rangle = (x + |x|)/2$ . The function  $\varphi$  is a dimensionless function of the overstress, which is dependent on the rate independent static yield function  $f_s$  and must meet the criteria given in Eqn. (52):

$$\begin{aligned} \varphi(f_s) \text{ is continuous in } [0, \infty] \\ \varphi(0) = 0 \rightarrow \dot{\lambda}^{vp} = 0 \end{aligned} \quad (52)$$

As previously stated, the viscosity is mostly influenced by the temperature of the viscoplastic deformation. However, the formulation of the Perzyna model given above does not explicitly include this impact. The temperature impact is of utmost importance in thermo-viscoplastic deformation, particularly under adiabatic circumstances. Therefore, to minimize the relaxation time, it is crucial to establish a direct correlation between viscosity and temperature, taking into consideration the influence of accumulated heat on adiabatic deformation. In other words, a rate-independent elastic-plastic model can be retrieved, if  $\eta$  approaches a minimum relaxation time value ( $\eta_0^{vp}$ ), indicating a negligible viscosity. the yield stress should be associated with a certain reference temperature and an extremely high strain rate (where  $\eta^{vp} \dot{\epsilon} \rightarrow 1$ ), at which, the overstress reaches its peak value.

Therefore, the current work considers both the overstress function and viscosity parameter as temperature related variables, where the threshold yield stress ( $\hat{\sigma}$ ) is chosen to normalize the overstress function that is taken at  $T \rightarrow 0$ , or  $\dot{\epsilon}_p \rightarrow \dot{\epsilon}_{p0}^i$ . Consequently, after utilizing Eqn. (7), the viscoplastic multiplier in the Perzyna model is obtained as given in Eqn. (53):

$$\lambda^{vp} = \frac{1}{\eta^{vp}(T)} \varphi(f_s, T, \hat{\sigma}) \quad (53)$$

The normalized overstress function given in Eqn. (53) helps in providing a smooth transition from static to dynamic surface or vice versa. Moreover, certain metals exhibit rate dependency even when  $\dot{\epsilon}_p < \dot{\epsilon}_s$ . This suggests that the concept of  $\dot{\epsilon}_s$  does not genuinely apply to real plastic/viscoplastic deformations. In addition, in case of adiabatic deformation,  $f_s$  may align with  $f_{ath}$  when  $\dot{\epsilon}_p > \dot{\epsilon}_s$ , thus indicating an observable rate independent behavior. Therefore, by rearranging Eqn. (12), it is possible to determine the strain rate ( $\dot{\epsilon}_{ath}$ ) at which the metal reaches a state insensitive to changes in temperature and strain rate as defined below in Eqn. (54).

$$\dot{\epsilon}_{ath} = \dot{\epsilon}_{p0}^i e^{-\frac{1}{\beta_2 T_{cr}}} \quad (54)$$

Hence, the normalized overstress function  $\varphi(f_{ath}, T, \hat{\sigma})$  can be defined as Eqn. (55) below:

$$\begin{aligned} \varphi(f_{ath}, T, \hat{\sigma}) &= \exp\left(1 - \frac{(1 - (1 - (f_{ath}/\hat{\sigma}))^p)^q}{\beta_2 T}\right) && \text{for } f_{ath} \geq 0 \\ \varphi(f_{ath}, T, \hat{\sigma}) &= 0 && \text{for } f_{ath} < 0 \end{aligned} \quad (55)$$

As discussed by Voyiadjis and Abed,  $\eta^{vp}$  depends on the waiting time, which is influenced by the temperature. In adiabatic heating, the heat generated inside the metal weakens the obstacles, thus allowing dislocations to overcome them easily, resulting in softening in the metal. This means that increase in temperature reduces the metal viscosity, which significantly reduces the thermos-visco stress. As the temperature reaches the critical temperature ( $T_{cr}$ ), the thermal stress disappears completely, and the yield surface reduces to  $f_{ath}$ .

For the case of dynamic yield function (Eqn. (56)), the consistency model is employed by incorporating a yield condition with a value of zero, which extends the conventional elastoplasticity theory. This model assumes that the ratio of the overstress to the viscosity determines  $\dot{\lambda}^{vp}$ . The dynamic yield surface is represented in a comparable manner to Eqn. (48), after considering  $f_{ath}$  in place of the static yield function ( $f_s$ ), and ignoring the DSA component, as shown in Eqn. (56):

$$f_d = \sigma_{eq} - \underbrace{(Y_a + B\varepsilon_p^n)}_{\sigma_{ath}} - \underbrace{\hat{\sigma} \left( 1 - (-\beta_2 T \ln(\eta_0^{vp} \dot{\varepsilon}_p)) \right)^{\frac{1}{q}}}_{\sigma_v^{th}(\dot{\varepsilon}, T)} \equiv 0 \quad (56)$$

In Eqn. (56), the DSA component is ignored to avoid complexity, as at a particular strain rate and temperature, its value remains fixed and thus it does not play a significant role in defining the dynamic yield function. As discussed earlier, this function can be used to distinguish between the elastic (when  $f_d < 0$ ) and viscoplastic ( $f_d = 0$ ) state of deformation. Therefore, the following consistency condition is yielded:

$$\dot{f}_d = \frac{\partial f_d}{\partial \sigma_{ij}} \dot{\sigma}_{ij} + \frac{\partial f_d}{\partial \varepsilon_p} \dot{\varepsilon}_p + \frac{\partial f_d}{\partial T} \dot{T} + \frac{\partial f_d}{\partial \dot{\varepsilon}_p} \dot{\dot{\varepsilon}}_p = 0 \quad (57)$$

Eqn. (57) can be used to obtain  $\dot{\lambda}^{vp}$  using a differential equation form [78] as given in Eqn. (58):

$$\dot{f}_d = N_{ij} \dot{\sigma}_{ij} - (h + \theta) \dot{\lambda}^{vp} - y \ddot{\lambda}^{vp} = 0 \quad (58)$$

Where  $h$  represents the hardening modulus,  $\theta$  is the softening parameter and  $y$  is the SRS. To introduce the constitutive equations, it is necessary to have a numerical framework that is thermodynamically consistent. The deformation behavior of thermo-elastic-viscoplastic can be defined using two potentials: one to describe the current state (thermodynamic potential), and another to account for irreversible evolutions (dissipative potential) [75]. The details for the thermodynamic formulations can be found in the works reported by Abed and coworkers [16, 75, 77]. After defining all the parameters, the viscoplastic multiplier ( $\dot{\lambda}^{vp}$ ) can be derived by the following expression:

$$\dot{\lambda}(t) = \dot{\lambda}(0) + \frac{1}{y} \left( N_{ij} \varepsilon_{ij}(t) - N_{ij} \varepsilon_{ij}(0) \right) - \frac{H}{y} (\lambda(t) - \lambda(0)) \quad (59)$$

In Eqn. (59),  $H = 3\mu + C - \gamma N_{ij} + h + \theta$ , where  $\mu$  is the shear modulus while  $C$  and  $\gamma$  are material constants.  $N_{ij} = \partial f_d / \partial \sigma_{ij}$  (Eqn. (57) & (58)) and  $\varepsilon_{ij}$  is the strain tensor.

Once the viscoplastic multiplier is determined, the stress and other state variables are updated accordingly which can either be displacement-based or strain-based. In the former method, stress updates at the Gauss points corresponding to a given nodal displacement. Initially, it is assumed that the load history is segmented into sub-intervals. When moving from step  $n$  to  $n + 1$ , we begin at time ( $t_n$ ) with the established converged state ( $\sigma_n, R_n, T_n, \dots$ ). From there, we use an implicit integration scheme to calculate the corresponding values at time  $t_{n+1} = t_n + \Delta t$ .

On the other hand, for strain-based process, the updated total strain ( $\varepsilon_{n+1}$ ) is known and the unknown variables are determined through  $\Delta \lambda^{vp}$ . To accomplish this, the constitutive equations must be discretized and transformed into a residual form. For instance, Eqn. (60) shows the residual expression for the stress.

$$\mathbf{r}_\sigma = \boldsymbol{\sigma}_{n+1} - \mathbf{E} : (\boldsymbol{\varepsilon}_{n+1} - \boldsymbol{\varepsilon}_{n+1}^{vp}) \quad (60)$$

Similarly, the other state variables can be solved while fulfilling the condition given in Eqn. (61)

$$\mathbf{r} (\boldsymbol{\sigma}_{n+1} \quad \boldsymbol{\omega}_{n+1} \quad \Delta \lambda^{vp}) = \mathbf{0} \quad (61)$$

In Eqn. (61),  $\boldsymbol{\omega}_{n+1}$  represent the internal state variables ( $R_{n+1}, T_{n+1}, \dots$ ). Generally, the residual stresses are interlinked, so the solution must be obtained through an iterative process. Therefore, the set of non-linear equations can be solved using a standard Newton-Raphson method by considering the unknowns given in Eqn. (62):

$$\mathbf{x} = [\boldsymbol{\sigma}_{n+1} \quad \boldsymbol{\omega}_{n+1} \quad \Delta \lambda^{vp}]^T \quad (62)$$

Eqn. (63) gives the resultant solution:

$$\mathbf{x}^{i+1} = \mathbf{x}^i - \mathbf{J}(\mathbf{x}^i) \mathbf{r}(\mathbf{x}^i) \quad (63)$$

In this context, the superscripts ( $i$  and  $i + 1$ ) denote the preceding and current iteration, respectively. The Jacobian matrix ( $\mathbf{J}$ ), in relation to the definitions provided above for the internal state variables, assumes a highly complex structure that defines the inverse of the residual's derivative in relation to the internal state variables as shown in Eqn. (64).

$$\mathbf{J}(x^i) = \left( \frac{\partial \mathbf{r}_{n+1}^i}{\partial x_{n+1}^i} \right)^{-1} \quad (64)$$

The solution provided in Eq. (63) offers a general approach for solving a set of non-linear equations. However, in terms of computational efficiency, it may not be the most optimal solution. Indeed, the calculation of the derivatives of the state variables, as required by Eq. (64) for evaluating the Jacobian matrix, can pose a significant challenge for the solution algorithm. When it comes to realistic material models, calculating higher order derivatives of the functions mentioned can be quite challenging or even time-consuming. When faced with such situations, it is most desirable to have an algorithm that solely relies on the essential response functions. Thus, the radial return mapping algorithm, being a variant of the backward-Euler procedure, seeks to overcome the mentioned limitations. For this purpose, the elastic predictor–viscoplastic corrector method is employed in conjunction with both the Perzyna and Consistency viscoplastic models to solve the constitutive equations. Equation (64) is then simplified into a non-linear relation involving a single scalar variable. Additional details can be found in the work by Abed (2005) [75].

For situations involving small deformations, the non-linear behaviour of the material is represented by a rate-form constitutive relation. This relation connects the stress rate to the strain rate, as well as certain internal variables. However, when considering geometrical non-linearity (such as in large deformation problems), the assumption mentioned earlier becomes invalid. In this case, it is crucial to carefully choose appropriate stress and strain rates to maintain the objectivity and rigid body motion in the constitutive formulation. An effective approach to solve such a problem is to utilize objective tensor quantities. The concept of material objectivity asserts that a constitutive relation must remain unaffected by any rigid body motions. In other

words, it should be consistent for two observers who are in relative motion, whether it be translation or rotation.

The objective of these FE simulations is to enhance the understanding related to the response of metals to varying loading conditions and the underlying factors that lead to their failure. The constitutive model (Eqn. (39) and Eqn. (40)) is used in the development of algorithms with the objectivity of capturing dynamic strain aging. The basic framework is coded in the context of the fully implicit (backward Euler) difference method, which is well-known for its exceptional convergence and high accuracy when doing large-scale computations that take a long time. A nonlinear scalar problem is introduced with the help of the radial return algorithm, which is a type of the backward-Euler method. To extend from a small strain constitutive relationship to one that includes finite strains, the effects of finite rotations must be accounted for. This study utilizes a stress integrating method called "local rotated representation." By using this method, we can reduce the problem to the numerical integration of the initial value problem, which will result in a one-parameter subgroup of proper orthogonal transformation [75].

This work presents numerical simulations that will demonstrate the effectiveness of the suggested algorithm in the ABAQUS FE code by using the user defined VUMAT subroutine. However, the implementation is focused on the temperature ranges for dynamic strain aging at a given strain rate, based on the diffusion of solute atoms and their interactions with the dislocations. The numerical results are discussed in comparison with the available experimental data and the constitutive modelling results. Different metals and alloys with distinct material parameters are used in the case studies, which use experimental data from the literature. Numerical problems are also simulated to study the effects of DSA in necking and shearing applications.

### **3.3. Potential Implications**

The study aims to enhance comprehension of the DSA phenomenon, thereby augmenting the existing knowledge base in the field of material science and engineering. The developed model is expected to serve as a valuable instrument for alloy designers, facilitating the controlling of DSA using the model predictions to enhance the mechanical characteristics and lifespan of metals and alloys.

## Chapter 4. Results and Discussions

### 4.1. Commercially Pure Niobium (CP-Nb)

Niobium (Nb), a body-centred cubic (bcc) metal, is often used to increase the strength of steels. Prior constitutive models for Nb at elevated strain rates were successfully formulated by Nemat Nasser [44] and Voyiadjis et al. [8]. Nevertheless, these models did not possess compatibility at lower strain rates. Furthermore, it was noted that DSA was absent at elevated strain rates, but it was present at lower strain rates, as depicted in Figure 15). This activation of DSA could not be accounted for by the original VA model, as illustrated in Figure 16 [8].

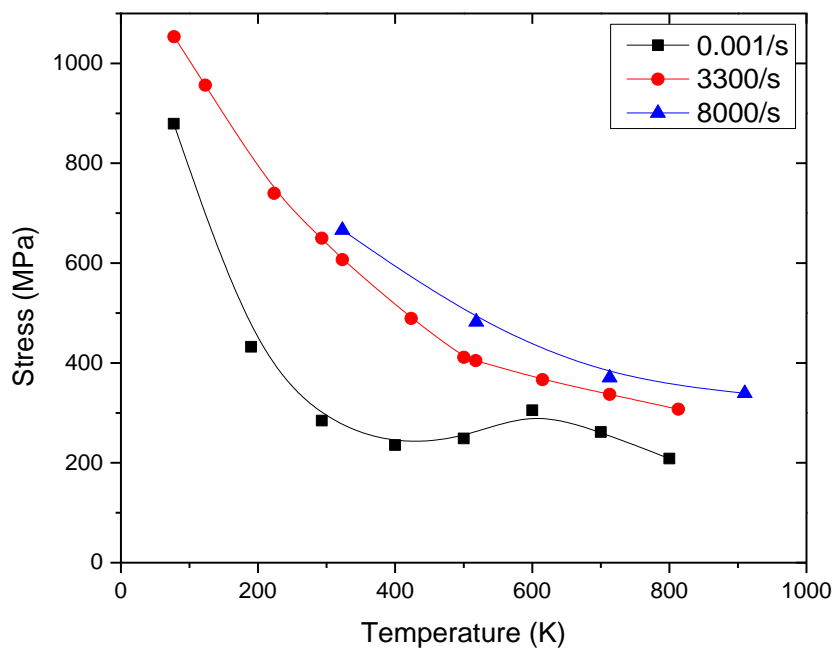


Figure 15 Stress-temperature curves experimentally determined for various strain rates at a plastic strain of 10% for Niobium [44].

Table 1 gives the diffusion data for various impurities evaluated while Table 2 gives the values for parameters that are utilized in Equation (39) for calculating the flow stress for CP-Niobium.

The strength of the metal began to rise when the concentration of diffusing impurity atoms inside the dislocation core increased with temperature at specific strain rates. Furthermore, every impurity atom generates the pinning effect at a distinct

temperature value, which is determined by its diffusion characteristics. Hence, only specific impurity atoms possess the ability to activate DSA and limit the motion of dislocations. The impact of dynamic strain aging (DSA) can be noticed in the stress-temperature relationship at a plastic strain of 10%, as depicted in Figure 16. The original VA model failed to account for DSA in cases where the DSA stress component was absent. However, the modified VA model successfully captured DSA in these scenarios.

Table 1 Diffusion Equation Parameters for impurity diffusion in CP-Niobium

Atom	Carbon	Oxygen	Nitrogen
Diffusion Constant (m <sup>2</sup> /s)	9.8 x 10 <sup>-7</sup>	1.5 x 10 <sup>-6</sup>	6.23 x 10 <sup>5</sup>
Activation Energy (eV)	1.73	1.18	2.1

Table 2 Model Parameters for CP-Niobium.

Parameter	$Y_a$ (MPa)	$B$ (MPa)	$n$	$\hat{\sigma}$ (MPa)	$p$	$q$
Value	25	340	0.27	1200	0.36	1.84
Parameter	$G_0$ (eV)	$\dot{\epsilon}_{po}^i$ (s <sup>-1</sup> )	$\rho$ (g/cm <sup>3</sup> )	$\bar{m}$	$k$ (eV/K)	$b$ (m)
Value	1.6	9.9 x 10 <sup>6</sup>	8.57	1	8.62 x 10 <sup>-5</sup>	2.95 x 10 <sup>-10</sup>
Parameter	$\rho_m$ (m <sup>-2</sup> )	$d$ (m)	$a'$ (m)	$Q_d$ (eV)	$D_0$ (m <sup>2</sup> /s)	
Value	1 x 10 <sup>12</sup>	2.95 x 10 <sup>-8</sup>	8.85 x 10 <sup>-10</sup>	2.1	6.23 x 10 <sup>5</sup>	

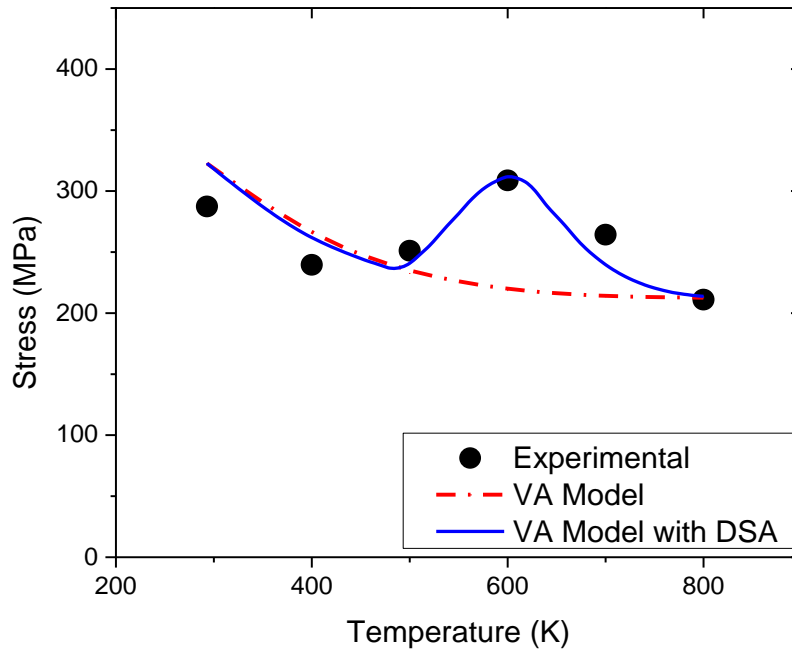


Figure 16 Comparison of Stress vs Temperature for the two models against the experimental data for Niobium at a plastic strain of 10% at  $\dot{\epsilon}_p = 0.001/s$ .

As previously stated, the thermal stress in bcc metals is mostly determined by the threshold yield stress, while the hardening is not significantly affected by temperature. This can be deduced from the experimental evidence depicted in Figure 17. The stress-vs-temperature graph demonstrates that the hardening is temperature-independent since the stress is rising roughly linearly with an increase in plastic strain. This clearly shows that the DSA is caused by interactions between solute atoms and dislocations at short-range barriers.

Figure 18 (a-f) presents the stress-strain graphs that compare the constitutive modeling results with and without the influence of dynamic strain aging (DSA) component to the experimental data. The original VA model failed to accurately represent the activation of DSA during the temperature range of 500 K – 700 K. Nevertheless, upon incorporating the DSA stress component (that considers the impact of impurity atoms and dislocations on stress), the model successfully projected the activation of DSA as depicted in Figure 18 (c-e)). This comparison indicates that the modified model is more appropriate for predicting the behavior of the metal under

thermomechanical loading scenarios at different temperatures and strain rates and could be valuable for future research.

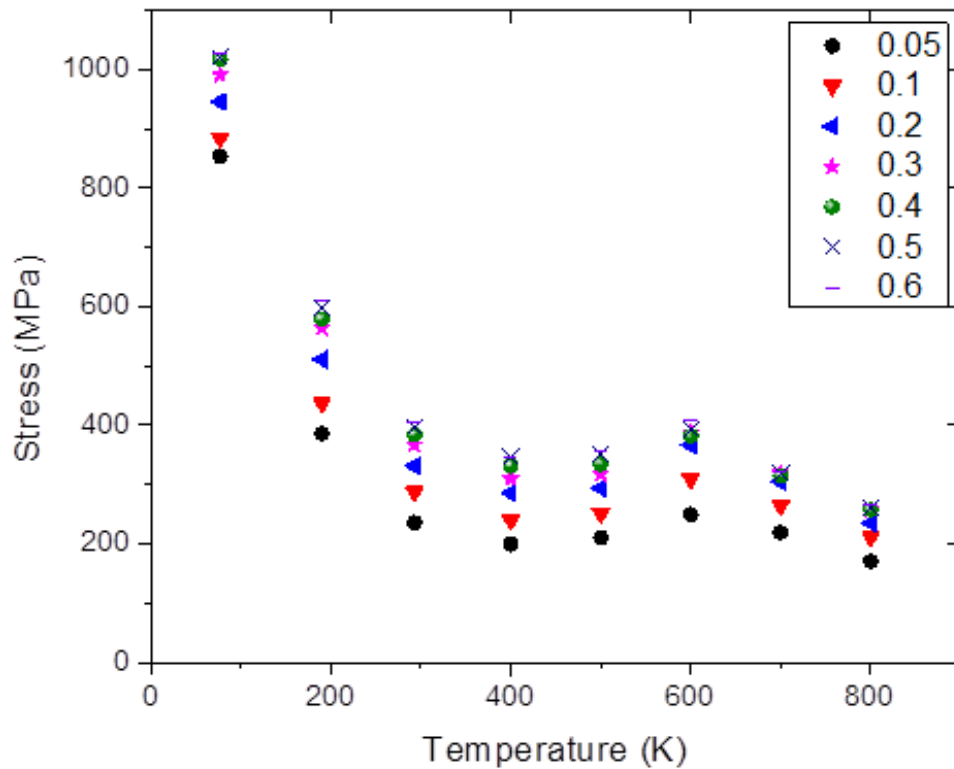


Figure 17 Stress-temperature relationship at various plastic strain levels in Niobium at  $\dot{\epsilon}_p = 0.001/s$  [44].

As mentioned before, the initiation of DSA by different impurities takes place at different temperatures. The diffusion of nitrogen, oxygen, and carbon in bcc niobium begins at temperatures of about 490K, 585K, and 740K, respectively, when subjected to a strain rate of 0.001/s. The collective impact of each impurity aids in capturing the rise in stress induced by DSA by contributing to the concentration of impurities at the core of the dislocation. The diffusion of nitrogen is the primary factor contributing to DSA activation in bcc Nb material while the carbon diffusion takes place at a temperature that is close to the athermal stress temperature, leading to its minimal impact. As evidenced by the results presented, the developed constitutive model successfully captures the activation of dynamic strain aging in commercially pure bcc niobium.

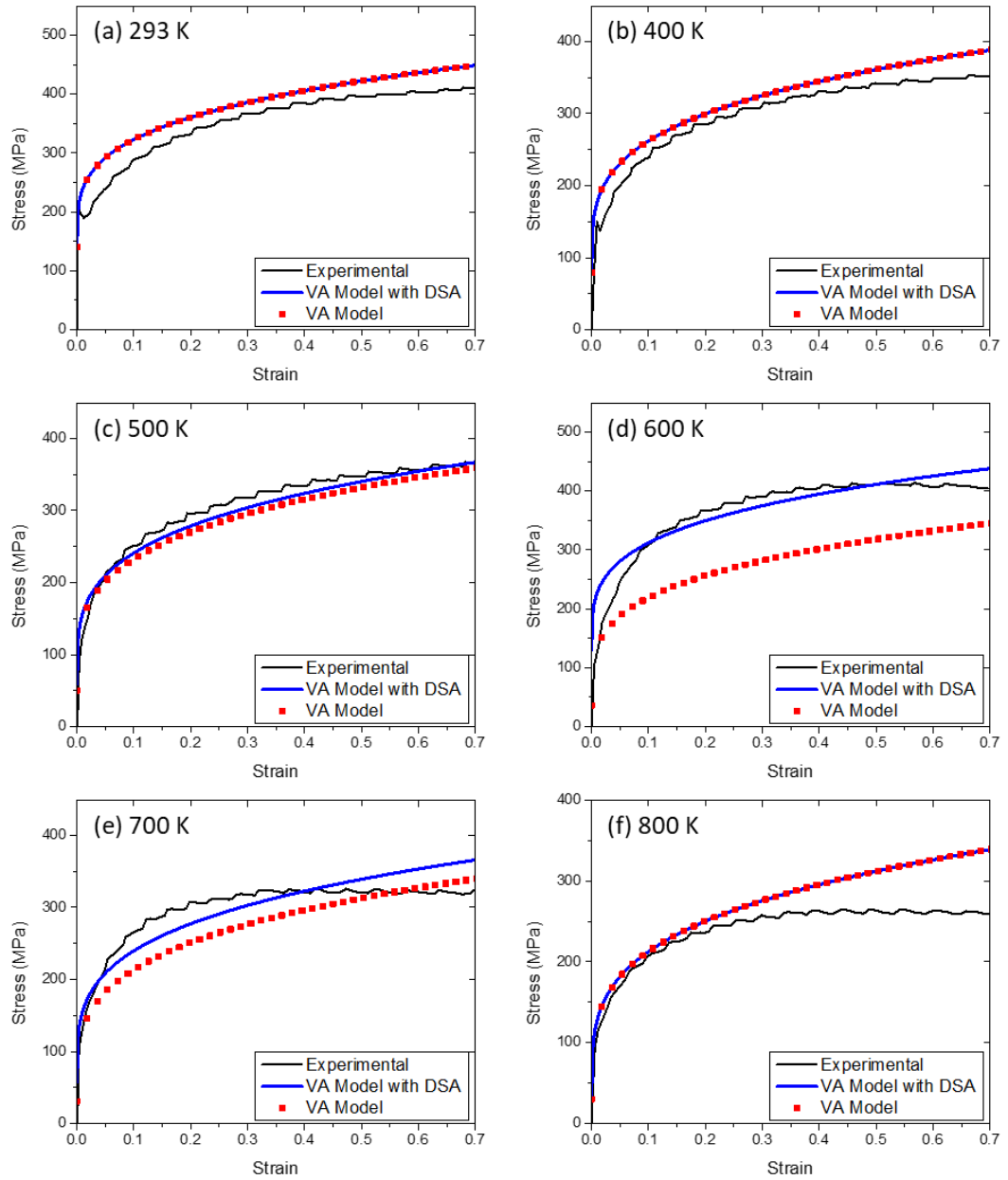


Figure 18 Stress-Strain curves at  $\dot{\epsilon}_p = 0.001/s$  for the VA model with and without DSA in comparison to the experimental data for Niobium. The temperatures considered are (a) 293 K, (b) 400 K, (c) 500 K, (d) 600 K, (e) 700 K, and (f) 800 K.

#### 4.2. CP-Vanadium (CP-V)

Vanadium (V) is a ductile and malleable body-centred cubic (bcc) metal that adds to structural strength of alloys. It is frequently employed in aeronautical applications as part of titanium alloys. The experimental data for vanadium has also been obtained from the research conducted by Nasser and his colleagues [24]. Similarly to CP-Nb,

CP-Vanadium has demonstrated dynamic strain aging (DSA) at lower strain rates, and no DSA was observed at greater strain rates, as depicted in Figure 19. Nemat Nasser et al. [24] and Voyiadjis et al. [8] successfully simulated the thermomechanical behaviour at elevated strain rates, but their models were not applicable for lower strain rates. The VA model exhibited effectiveness when DSA was inactive at lower strain rates. However, it has limited applicability in the regions exhibiting DSA (as depicted in Figure 20). The diffusion data for different impurities in CP-V is presented in Table 3 while the values of different parameters for Vanadium, as stated in Eqn. (39) are listed in Table 4. Figure 20 depicts a comparison between stress and temperature for both the original VA model and the modified VA model, against the experimental data taken at a plastic strain of 10%. The graphs illustrate the impact of the additional term that highlights the role of impurity atom diffusion and their interaction with dislocations. The addition has greatly improved the VA model making it capable of predicting and capturing the activation of DSA, which was previously impossible.

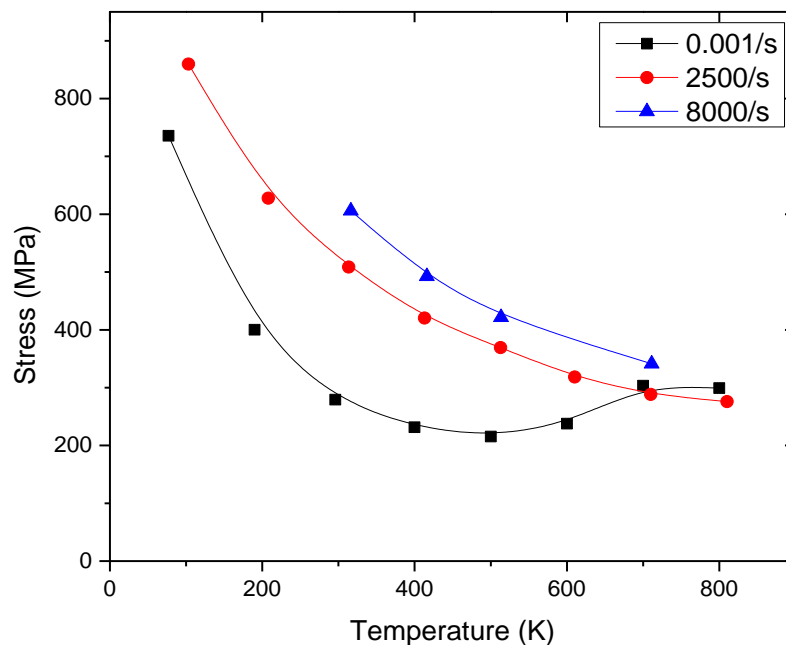


Figure 19 Stress-temperature curves experimentally determined for various strain rates at a plastic strain of 10% for CP-Vanadium [24].

Table 3 Diffusion Equation Parameters for impurity diffusion in CP-Vanadium

Atom	Carbon	Oxygen	Nitrogen
<b>Diffusion Constant (m<sup>2</sup>/s)</b>	8.8 x 10 <sup>-7</sup>	5.9 x 10 <sup>-5</sup>	4.7 x 10 <sup>-7</sup>
<b>Activation Energy (eV)</b>	1	1.82	1.25

As previously discussed, the yielding mechanism plays a major contribution in determining the thermal strength of bcc metals. Consequently, plastic deformation is minimally affected with changes in temperature (Figure 21). Figure 22 shows the comparison of the experimental data with the model devised in Eqn. (39). It was noted that the VA model was unable to capture DSA. However, the constitutive model given in Eqn. (39) successfully captured the strength increase caused by DSA. The introduction of the impurity/solute interaction mechanism enabled this effect, as demonstrated in Figure 22 (d-f).

Table 4 Model parameters for CP-Vanadium

Parameter	$Y_a$ (MPa)	$B$ (MPa)	$n$	$\hat{\sigma}$ (MPa)	$p$	$q$
<b>Value</b>	20	230	0.53	650	0.48	1.8
Parameter	$G_0$ (eV)	$\dot{\epsilon}_{po}^i$ (s <sup>-1</sup> )	$\rho$ (g/cm <sup>3</sup> )	$\bar{m}$	$k$ (eV/K)	$b$ (m)
<b>Value</b>	2.65	1.1 x 10 <sup>6</sup>	6.11	1	8.62 x 10 <sup>-5</sup>	3.1 x 10 <sup>-10</sup>
Parameter	$\rho_m$ (m <sup>-2</sup> )	$d$ (m)	$a'$ (m)	$Q_d$ (eV)	$D_0$ (m <sup>2</sup> /s)	
<b>Value</b>	1 x 10 <sup>12</sup>	3.1 x 10 <sup>-8</sup>	9.3 x 10 <sup>-10</sup>	1	8.8 x 10 <sup>-7</sup>	

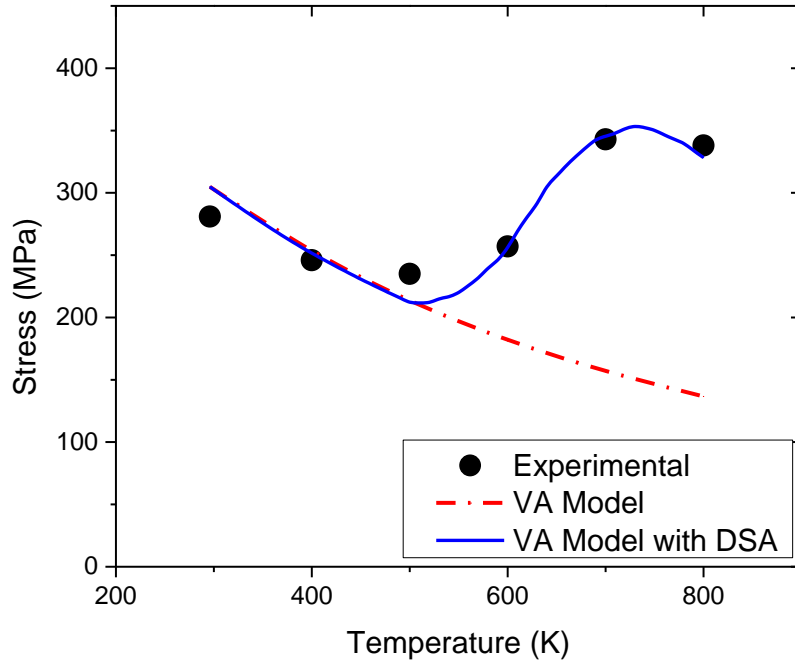


Figure 20 Comparison of Stress vs Temperature for the two models against the experimental data for Vanadium at a plastic strain of 10% at  $\dot{\epsilon}_p = 0.001/s$ .

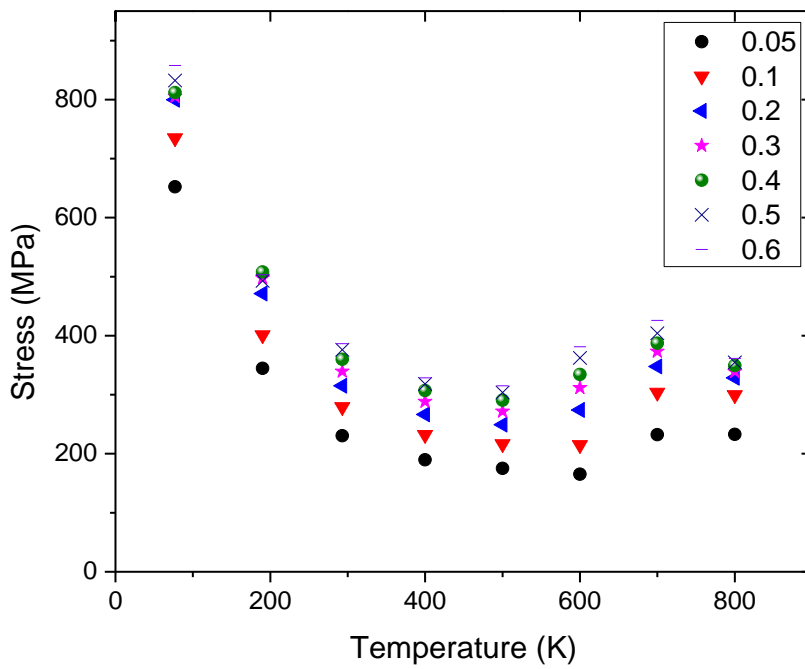


Figure 21 Stress-temperature relationship at various plastic strain levels in Vanadium at  $\dot{\epsilon}_p = 0.001/s$  [24].

This study revealed that the initiation of DSA occurred when carbon atoms diffused at a temperature of around 490 K, while the contribution of nitrogen impurities to DSA was observed at around 650 K. At the highest temperature reached during DSA (785 K), oxygen impurities engaged in the process of immobilizing dislocations. The collective impact of these impurity diffusions led to a strengthening effect within the temperature range of DSA, which in turn influenced the overall DSA profile.

### 4.3. CP-Titanium (CP-Ti)

CP-Ti is a plastically anisotropic hcp metal known to have good strength and high corrosion resistance properties. Owing their light weight and stability at elevated temperatures and extreme environments, most of its alloys are used in industrial, aerospace, defense, and biomedical applications [79-82]. However, the numerical modelling for this metal is rather complex due to the complicated micromechanics taking place during thermomechanical loading conditions. The diffusion parameters for different impurities in CP-Ti is presented in Table 5 while the model parameter values for the constitutive model are given in Table 6.

Nasser et al. validated that the formation of twins do not affect the flow stress in CP-Ti [43]. Figure 23 (a & b) presents the experimental flow stress vs temperature curve at the low and high strain rates for CP-Ti. It can be seen that there was no DSA at the yield points. Due to the formation of microstructural voids and defects, however, the diffusion of impurity atoms was made possible after yield point during plastic deformation in CP-Ti at various combinations of temperature and strain rates. As discussed earlier, at high temperatures, the stress is controlled by the athermal stress component only while both the athermal and thermal stress components control the flow stress mechanism at lower temperatures. In the intermediate temperatures, however, due to the diffusion of impurity atoms and their interactions with dislocations, there is activation of dynamic strain aging which is observed as an increase in the material flow stress.

Figure 24 (a & b) compares the numerical modeling results for the flow stress versus temperature profile at the yield point and 20% plastic strain for (a)  $\dot{\epsilon}_p = 0.001/s$  and (b)  $\dot{\epsilon}_p = 2200/s$ . It can be observed that the original VA model was able to capture the

yield stress and flow stress at very low and very high temperatures only where there was no DSA. But in the range of DSA, the model results were not very much comparable. On the other hand, the modified VA model gave a much better comparison with the experimental data both at the low and high strain rates. It was effective not only at the yield points, but also in the plastic deformation regions where the impurity atoms diffusion pinned the dislocation movement and increased the thermal activation energy at local obstacles.

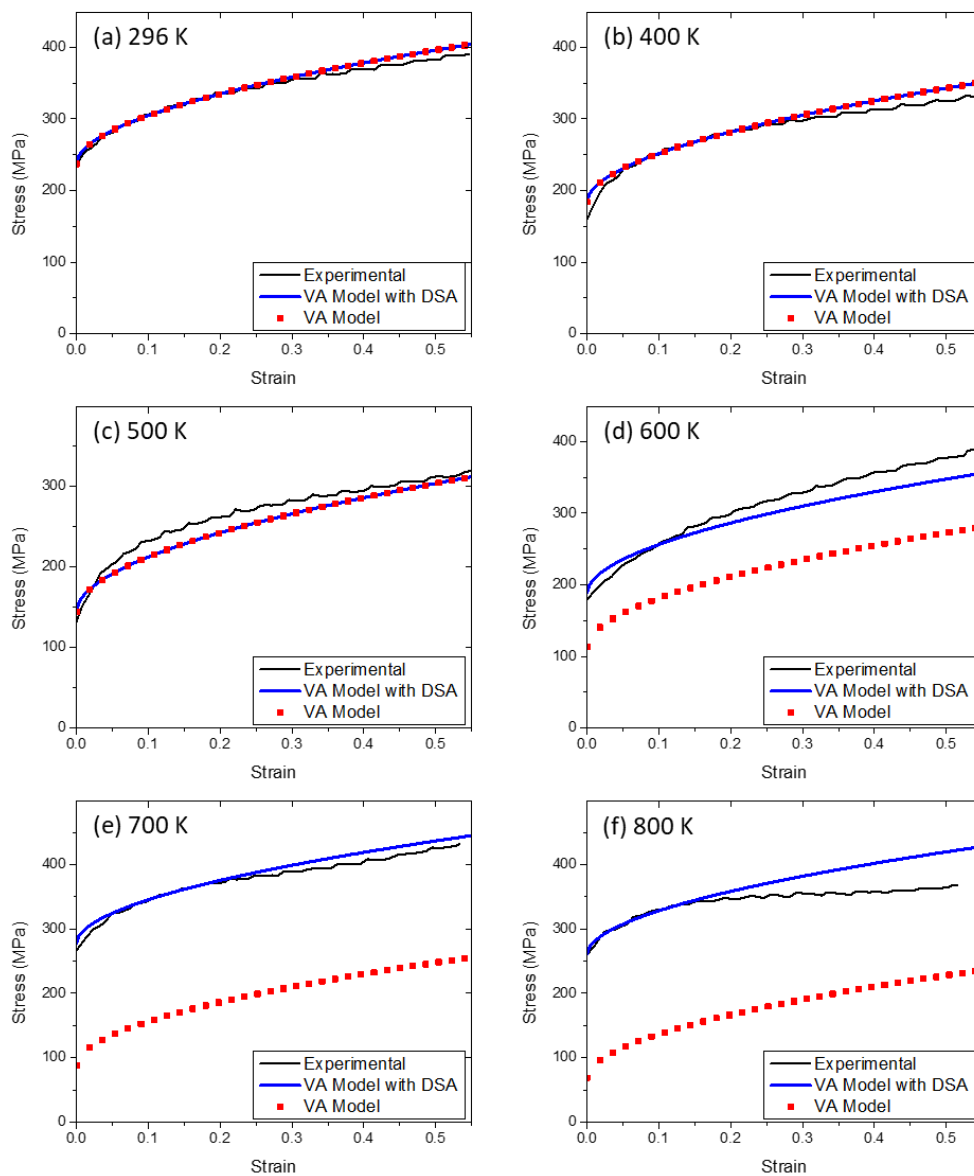


Figure 22 Stress-Strain curves at  $\dot{\epsilon}_p = 0.001/s$  for the VA model with and without DSA in comparison to the experimental data for Vanadium. The temperatures considered are (a) 293 K, (b) 400 K, (c) 500 K, (d) 600 K, (e) 700 K, and (f) 800 K.

Table 5 Diffusion Equation Parameters for impurity diffusion in CP-Titanium

Atom	Hydrogen	Carbon	Oxygen	Nitrogen
Diffusion Constant (m <sup>2</sup> /s)	1.15 x 10 <sup>-6</sup>	5 x 10 <sup>-4</sup>	4.5 x 10 <sup>-5</sup>	2.9 x 10 <sup>-5</sup>
Activation Energy (eV)	0.48	1.89	2.08	2.37

The stress strain profiles for CP-Ti, at a strain rate of 0.001/s is given in Figure 25. Comparing with the experimental results, both the original and the modified VA models were able to capture the yield point efficiently as also shown in Figure 24(a). This was due to no interactions of the impurity atoms with the dislocations. But, later on, as indicated in Figure 25(b-d), with the increase in plastic deformation, there was diffusion of impurity atoms at the newly available sites which increased the impurity atoms concentration along the dislocation line and restricted their flow through the localized obstacles. Consequently, a higher flow stress was observed and was only captured by the constitutive model that accounted for the diffusion kinetics of impurities in CP-Ti within the DSA range.

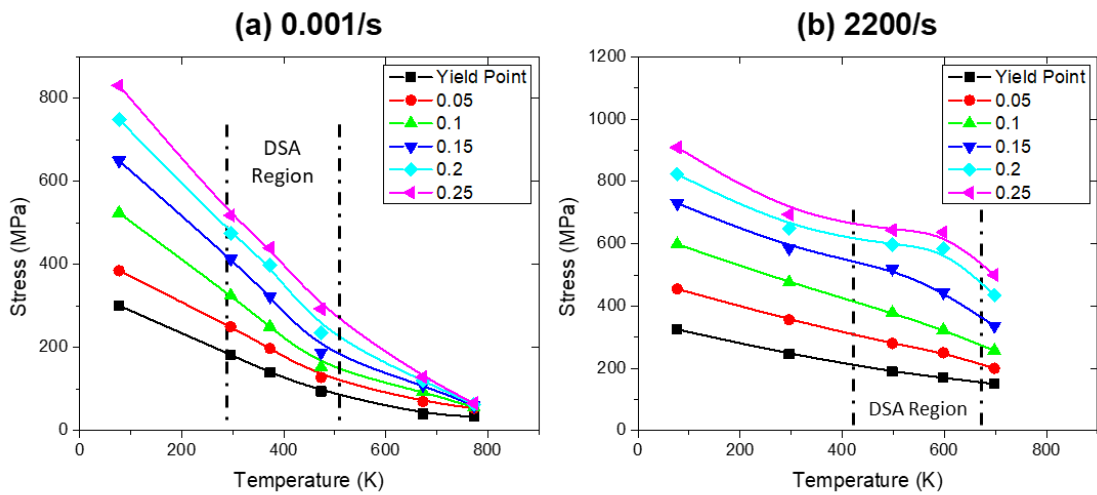


Figure 23 Experimental stress vs temperature with increase in plastic strain at (a)  $\dot{\epsilon}_p = 0.001/s$ , and (b)  $\dot{\epsilon}_p = 2200/s$

Table 6 Model parameter values for CP-Titanium

Parameter	$Y_a$ (MPa)	$B_1$ (MPa)	$n_1$	$\hat{\sigma}$ (MPa)	$p$	$q$
Value	30	65	0.43	270	0.5	1.5
Parameter	$B_2$ (MPa)	$n_2$	$G_0^Y$ (eV)	$G_0^H$ (eV)	$\zeta$	$c_p$ (J.g <sup>-1</sup> K <sup>-1</sup> )
Value	2000	0.55	1.68	1.67	0.985	0.52
Parameter	$\rho$ (g/cm <sup>3</sup> )	$\dot{\epsilon}_{po}^i$ (s <sup>-1</sup> )	$k$ (eV/K)	$\bar{m}$	$b$ (m)	$\rho_m$ (m <sup>-2</sup> )
Value	4.5	$1.95 \times 10^7$	$8.62 \times 10^{-5}$	1	$3 \times 10^{-10}$	$2.55 \times 10^{13}$
Parameter	$d$ (m)	$a'$ (m)	$D_0$ (m <sup>2</sup> /s)	$Q_d$ (eV)		
Value	$3 \times 10^{-8}$	$9 \times 10^{-10}$	$1.15 \times 10^{-6}$	0.48		

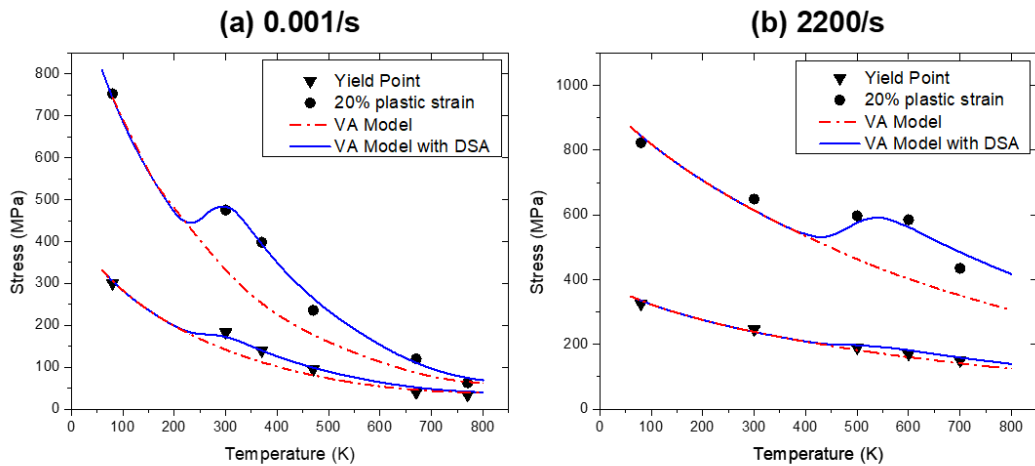


Figure 24 Comparison of the VA and Modified VA models to the experimental Stress vs Temperature profile at the yield point and 20% plastic strain and at (a)  $\dot{\epsilon}_p = 0.001/s$ , and (b)  $\dot{\epsilon}_p = 2200/s$ .

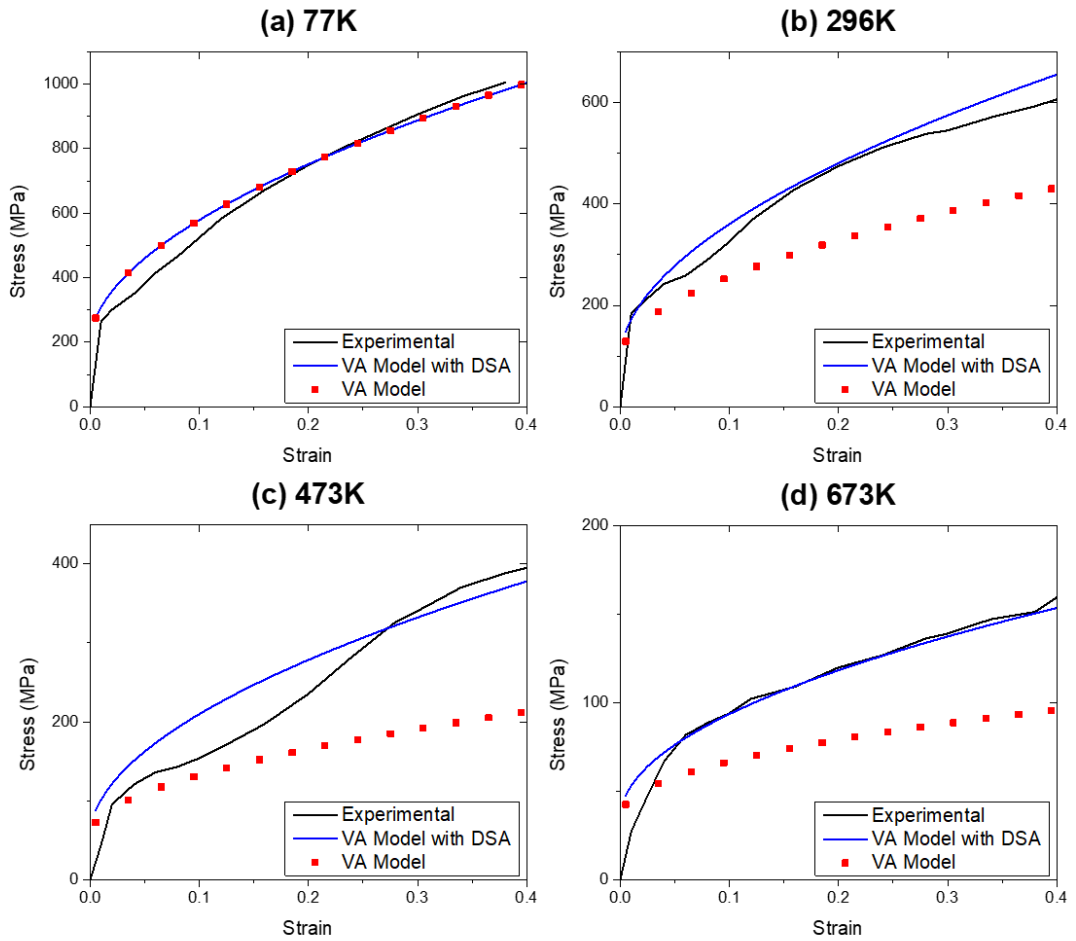


Figure 25 Comparison of Stress-Strain profile of CP-Ti for the VA model with and without the DSA component at  $\dot{\epsilon}_p = 0.001/s$  and  $T =$  (a) 77 K, (b) = 296 K, (c) = 473 K, and (d) = 673K.

Further, the temperature range for a particular impurity varies, in the case of CP-Ti, with a change in strain rate since each impurity starts diffusing into the dislocation core at its own specific temperature and strain rate applied. The diffusion kinetics constants revealed that at a strain rate of 0.001/s, the impurities of Nitrogen and Oxygen did not play any role in the diffusion kinetics even until a temperature of 700K while the impurities of Hydrogen, and Carbon, started to diffuse at 210 K and 670K, respectively.

The model outcome was similar when CP-Ti was loaded at a higher strain rate of 2200/s as can be seen in Figure 26(a-d). The yield points and the DSA inactive temperature regions were accurately captured by the VA model, when the thermal activation energy was assumed constant (Figure 26(a & b)). On the other hand, only

the modified VA model was able to capture DSA in the intermediate temperature region (Figure 26(c & d)).

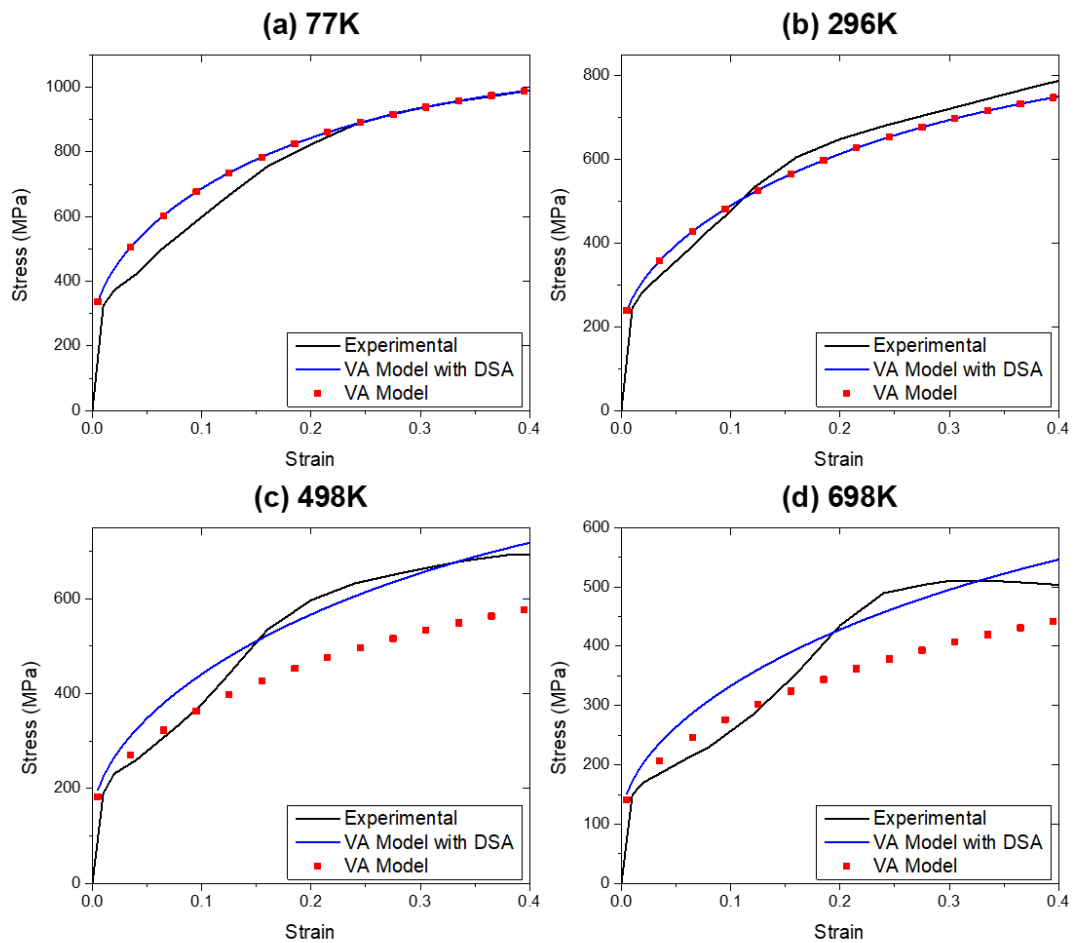


Figure 26 Comparison of Stress-Strain profile of CP-Ti for the VA model with and without the DSA component at  $\dot{\epsilon}_p = 2200/s$  and  $T =$  (a) 77 K, (b) = 296 K, (c) = 498 K, and (d) = 698 K.

As stated earlier, with an increase in the strain rate, the temperature range for DSA activation moves towards higher temperature. The beauty of the modification proposed here is that the physical parameters and the diffusion constant values define the temperature range for DSA activation and it automatically captures this effect of change in temperature range with a change in the strain rate. In this context, it was found that when the strain rate was increased to 2000/s, the diffusion of hydrogen started to take place at a temperature of about 390K while there was no contribution from carbon even until 700K temperature. The results shown in Figure 24(b) and

Figure 26(a-d) exhibit a high degree of similarity between the temperature range for diffusion delineated in this study and the one that was experimentally observed.

#### 4.4. Martensitic Microcomposite Formable (MMFX) Steel

Steel is an iron-based alloy that is widely used in different industrial applications. But the versatility of these applications in terms of strength and temperature has always been a focus of researchers, and several experimental works are performed to evaluate the thermomechanical response of this material [6, 10, 15, 17, 21, 35, 83-85]. Martensitic Microcomposite Formable Steel is an iron-based alloy that is mostly used in different structural applications [86] for its high strength [87] and corrosion resistance [88] properties.

The main reason for this steel to be used in corrosion resistance application is due to the high amount of chromium as well as the manufacturing process which avoids the formation of micro galvanic cells [86]. Abed and coworkers reported this steel to be exhibiting DSA at low (0.0015/s) and high (0.15/s) strain rates in temperature range of 400K to 800K. Moreover, the experimental data showed that the effect of temperature was visible in thermal yielding component of stress while hardening was insensitive to temperature (Figure 27). In this regard, Eqn. (39) was applied to capture the activation of DSA. The average chemical composition for this alloy is given in Table 7. The model parameters for MMFX steel are given in Table 8.

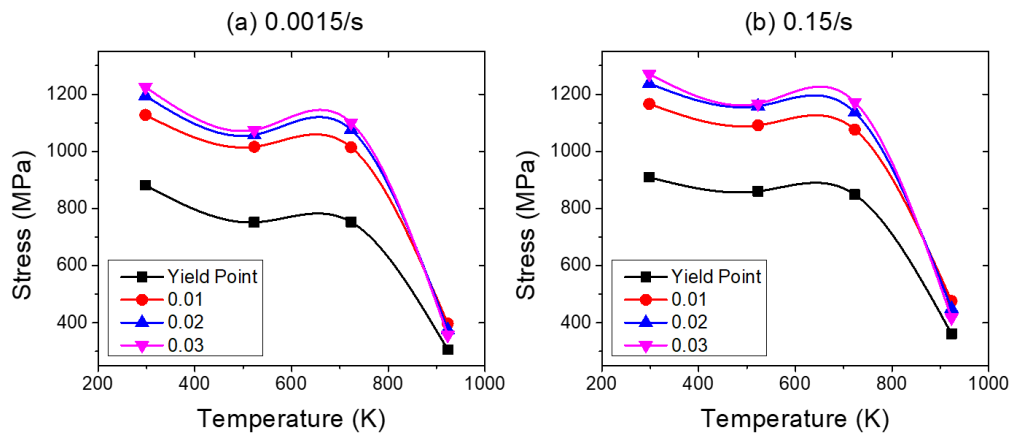


Figure 27 Stress-temperature curves experimentally determined for various plastic strains at strain rates of (a) 0.0015/s and (b) 0.15/s for MMFX steel [14].

The VA model with and without the DSA stress component has been compared with the experimental data at 1% plastic strain for the two strain rates i.e., 0.0015/s and 0.15/s in Figure 28 (a) and (b) respectively. The experimental flow stress has been plotted against the respective temperature where it was observed that the flow stress increased with temperature instead of decreasing owing to the activation of DSA at both the strain rates. In both the figures, it can be noticed that there was a rise in the stress in the range of 523 K to 723 K. The regular VA model was unable to capture DSA while the incorporation of diffusion kinetics-based DSA component in the flow stress enabled the constitutive model to capture DSA and gave a reasonable comparison to the experimental data.

Table 7. MMFX average chemical composition [14]

Constituent	C	Cr	Mn	Si	Fe
Wt. %	0.15	9.6	1.1	0.5	Balance

Table 8. Model parameters for MMFX steel.

Parameter	$Y_a$ (MPa)	$B$ (MPa)	$n$	$\hat{\sigma}$ (MPa)	$p$	$q$
Value	190	1050	0.26	2100	0.54	1.6
Parameter	$G_0$ (eV)	$\dot{\epsilon}_{po}^i$ (s <sup>-1</sup> )	$\rho$ (g/cm <sup>3</sup> )	$\bar{m}$	$k$ (eV/K)	$b$ (m)
Value	1.33	3 x 10 <sup>8</sup>	7.85	1	8.62 x 10 <sup>-5</sup>	2.02 x 10 <sup>-10</sup>
Parameter	$\rho_m$ (m <sup>-2</sup> )	$d$ (m)	$\alpha'$ (m)	$Q_d$ (eV)	$D_0$ (m <sup>2</sup> /s)	
Value	1 x 10 <sup>12</sup>	2.02 x 10 <sup>-8</sup>	6.08 x 10 <sup>-10</sup>	0.76	6.2 x 10 <sup>-7</sup>	

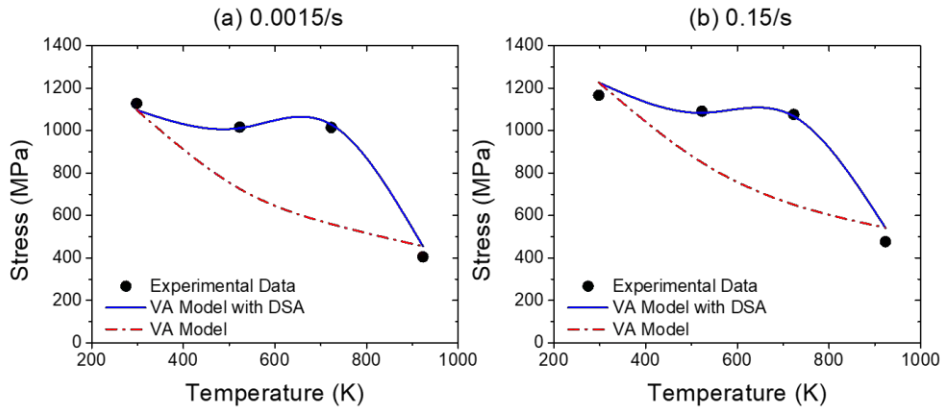


Figure 28 Stress vs Temperature comparison, at 1% plastic strain, between the two models with the experimental data for MMFX at (a)  $\dot{\epsilon}_p = 0.0015/s$  and (b)  $\dot{\epsilon}_p = 0.15/s$ .

The constitutive modeling comparison, for the stress-strain curves at  $\dot{\epsilon}_p = 0.0015/s$ , with and without the inclusion of the proposed modification is given in Figure 29 (a-d). It can be noticed here that both the regular and modified VA model could predict the experimental results in the absence of DSA (Figure 29 (a) & (d)). Figure 29 ((b) & (c)) shows that the regular VA model could not capture DSA due to the lack of diffusion-based DSA component. On the contrary, the comparative results for modified VA model clearly show the effect of diffusion kinetics on temperature and strain rates which made it possible to capture DSA in MMFX effectively.

Likewise, the comparison at higher strain rate is presented in Figure 30. By the same token, for  $\dot{\epsilon}_p = 0.15/s$ , when the effect of solute/dislocations interaction was not accounted for, the regular VA model could only predict the stress-strain curve for 298 K and 923 K temperature (Figure 30 (a) & (d)) where there was no DSA and was incapable of predicting the flow stress in the range of DSA (Figure 30 (b) & (c)). However, the proposed modification not only predicted the flow stress in the absence of DSA, it also accurately captured the flow stress within the DSA region. This clearly signifies the effectiveness of increase in solute concentration along the line of dislocations that resulted in the activation of DSA. The additional expression for capturing DSA only activates in the presence of DSA thus enabling the VA model to calculate stress-strain curves for MMFX steel at low strain rates and over a broad temperature range both in the absence and presence of DSA.

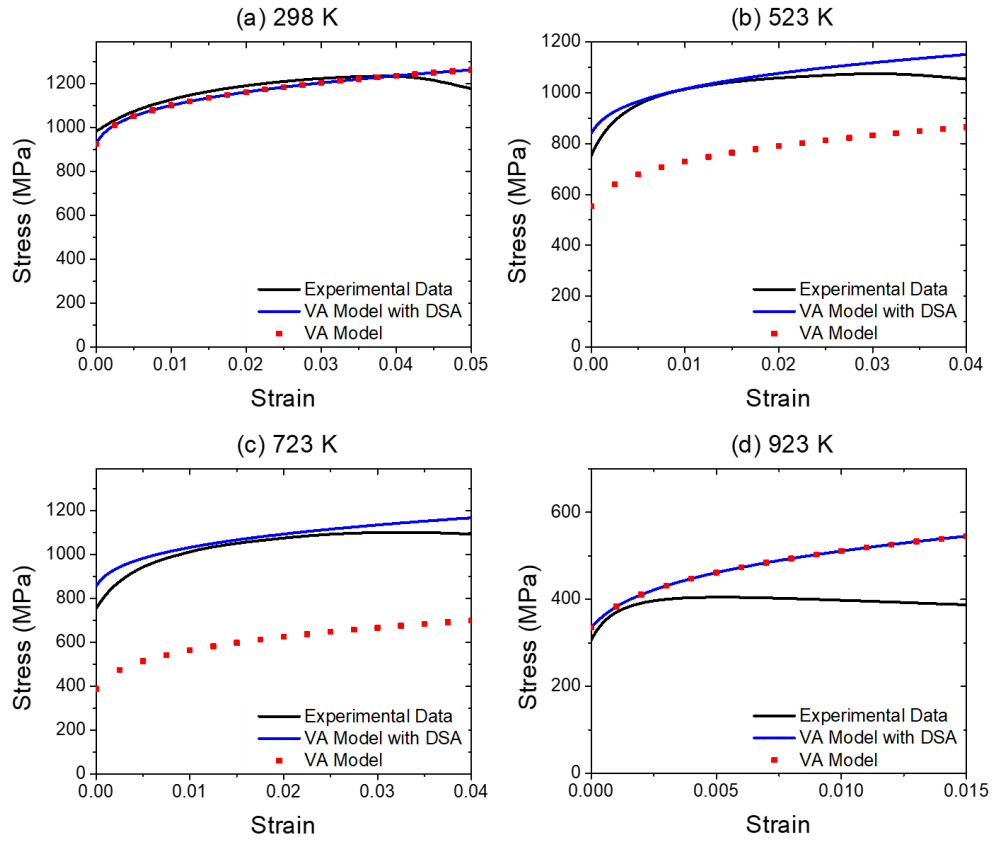


Figure 29 Stress-Strain curves for original VA model, modified VA model, and experimental data at  $\dot{\epsilon}_p = 0.0015/s$  and (a)  $T = 298$  K, (b)  $T = 523$  K, (c)  $T = 723$  K, and (d)  $T = 923$  K for MMFX steel

#### 4.5. Medium Carbon C45 Steel

C45 is a medium carbon steel with carbon being the major alloying element with 0.45 wt. % composition. The overall composition for this material is tabulated in Table 9 [21]. This material is known mostly for its applications in machines, tools, and structures where they can provide good strength, toughness, and weldability. Several studies exist for the experimental and numerical based analysis for its fatigue strength [89, 90], flow stress [91], damage behavior [21], frictional [92] and other surface properties [93-95]. Researchers have also investigated its thermomechanical response both experimentally and computationally [96, 97].

In their recent study on the damage behaviour of C45 steel, Abed et al. [21], reported the presence of DSA in C45 steel under specific combinations of temperature and strain rate. Furthermore, the activation of DSA was primarily detected in the

hardening region. This suggests that the long-range obstacles which contribute to the thermal hardening effect, are facilitating the occurrence of DSA (Figure 31).

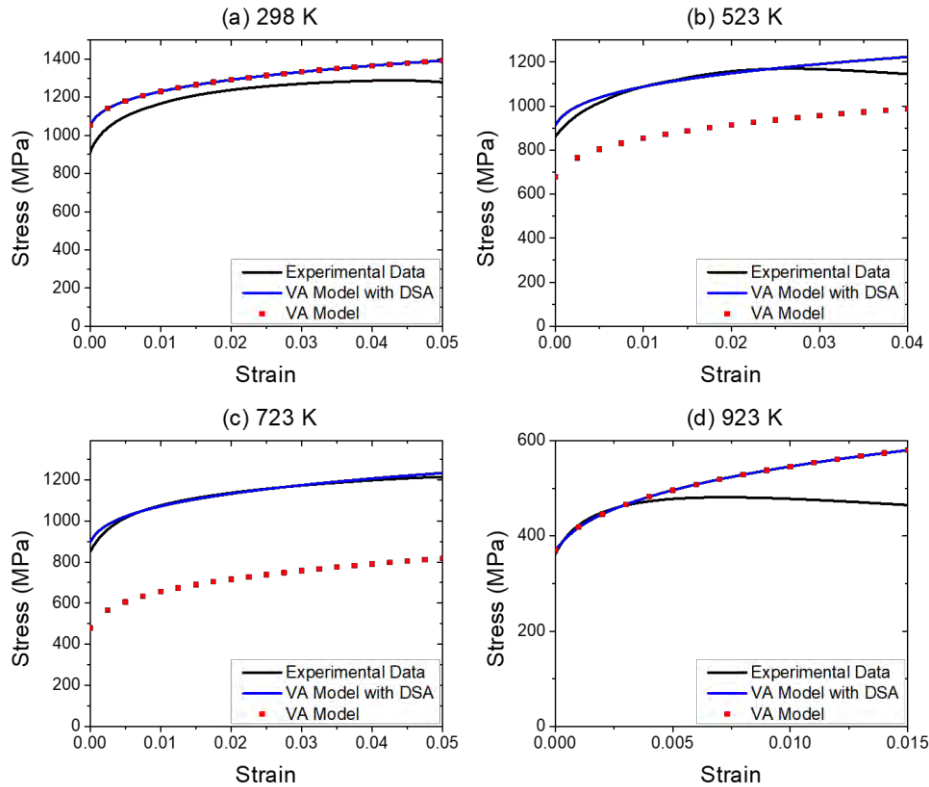


Figure 30 Stress-Strain curves for original VA model, modified VA model, and experimental data at  $\dot{\epsilon}_p = 0.15/s$  and (a)  $T = 298$  K, (b)  $T = 523$  K, (c)  $T = 723$  K, and (d)  $T = 923$  K for MMFX steel

Table 9 C45 steel composition [21]

Constituent	Fe	Mn	C	Si	P	S	Cu
Wt.%	98.45	0.62	0.45	0.25	0.19	0.02	0.02

Figure 31 presents the experimental stress vs temperature data taken at yield point and different plastic strains. One can observe here that at lower strain rate (i.e., 0.0015/s), there was a rise in the stress at 523 K which dropped to a temperature of 723 K indicating the presence of DSA effect. Similarly, at 0.15/s strain rate, the DSA peak shifted to higher temperature values. This indicates that DSA activation is not only dependent on the temperature but also on the strain rate.

A comparison was made for the VA model in the absence and presence of DSA component against the experimental data to validate the proposed modification given in Eqn. (40). The model parameters are tabulated in Table 10. The comparison between the two models and the experimental data at 4% strain is given in Figure 32 for different temperature and plastic strain rate. The figure clearly shows that considering the effect of increase in solute concentration, along the line of dislocation, has successfully enabled the VA model to capture DSA. Otherwise, if this is not considered, the VA model only gives comparable results in the absence of DSA. The results are further verified in the stress vs strain graphs for different temperatures and strain rates shown in Figure 33 (a & b) to Figure 36 (a & b) where (a) is for the lower strain rate i.e. 0.0015/s and (b) is for the higher strain rate i.e. 0.15/s.

Table 10 Model Parameters for C45 Steel.

<b>Parameter</b>	$Y_a$ (MPa)	$B_1$ (MPa)	$n_1$	$\hat{\sigma}$ (MPa)	$B_2$ (MPa)	$n_2$
<b>Value</b>	160	370	0.3	200	3000	0.3
<b>Parameter</b>	$p$	$q$	$G_0^Y$ (eV)	$G_0^H$ (eV)	$\dot{\epsilon}_{po}^i$ (s <sup>-1</sup> )	$k$ (eV/K)
<b>Value</b>	0.5	1.5	1.33	1.37	2.35 x 10 <sup>6</sup>	8.62 x 10 <sup>-5</sup>
<b>Parameter</b>	$\rho$ (g/cm <sup>3</sup> )	$\bar{m}$	$b$ (m)	$\rho_m$ (m <sup>-2</sup> )	$d$ (m)	$a'$ (m)
<b>Value</b>	7.85	1	2.02 x 10 <sup>-10</sup>	1 x 10 <sup>12</sup>	2.02 x 10 <sup>-8</sup>	6.08 x 10 <sup>-10</sup>
<b>Parameter</b>	$D_0$ (m <sup>2</sup> /s)	$Q_d$ (eV)				
<b>Value</b>	6.2 x 10 <sup>-7</sup>	0.76				

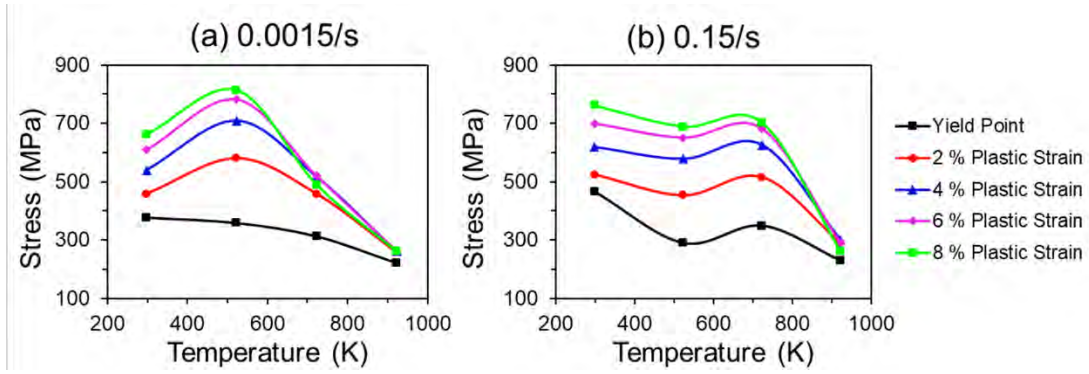


Figure 31 Stress vs Temperature curve for C45 Steel at the yield point and different  $\epsilon_p$  for (a)  $\dot{\epsilon}_p = 0.0015/s$  and (b)  $\dot{\epsilon}_p = 0.15/s$  [21].

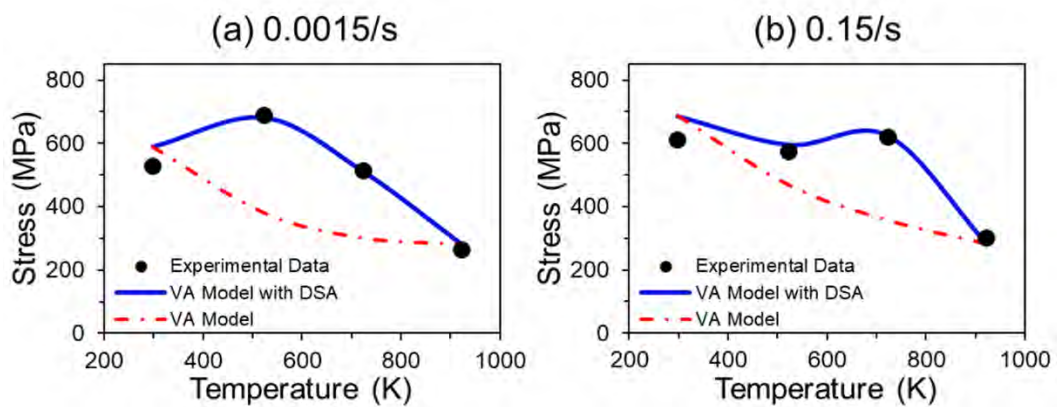


Figure 32 Stress vs Temperature comparison at 4% plastic strain between the two model with the experimental data for (a)  $\dot{\epsilon}_p = 0.0015/s$  and (b)  $\dot{\epsilon}_p = 0.15/s$ .

Figure 33 (a & b) shows the comparison between the VA model, modified VA model and experimental stress-strain curves at 923 K. Since this temperature was the critical temperature as indicated by the values of  $\beta$ , this curve has no thermal contribution and was utilized to find the athermal stress component of VA model. Note that this component was the same for both VA and modified VA model.

The experimental data showed no sign of DSA at 298 K. Therefore, the thermal component of stress was found as per the method discussed before using the experimental data at this temperature. As discussed before, the regular VA model without considering the effect of DSA is efficient enough to capture the thermomechanical response of any material over a broad range of temperature and strain rates [8-10, 15]. Likewise, the VA model accurately predicted the thermomechanical response for C45 at 298 K for both the strain rates of interest as

shown in Figure 34 (a & b). For comparison, the modified VA model results are also given and it can be seen that the modified model was also able to capture the experimental results with the same accuracy as of regular VA model.

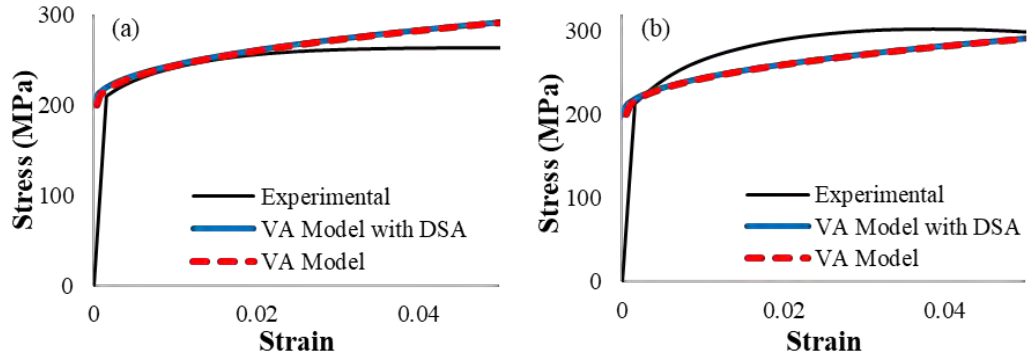


Figure 33 Stress-Strain curves defining the parameters for athermal component of VA model, in comparison to the experimental data, at  $T = 923\text{K}$  and (a)  $\dot{\epsilon}_p = 0.0015/s$  and (b)  $\dot{\epsilon}_p = 0.15/s$ .

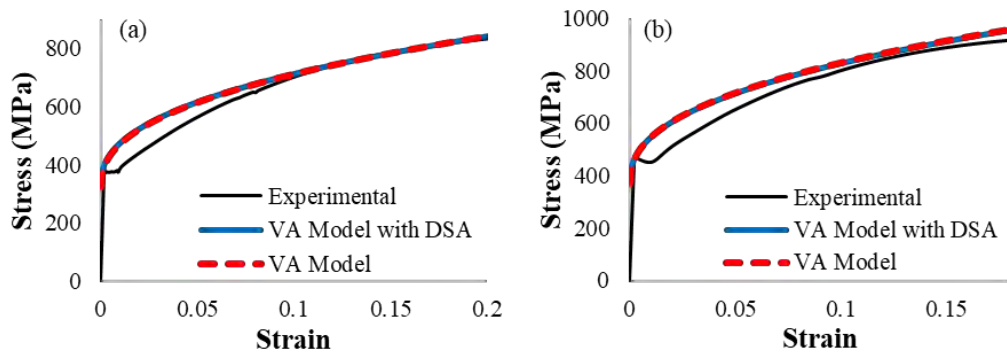


Figure 34 Stress-Strain curves for original VA model, modified VA model, and experimental data at  $T = 298\text{K}$  and (a)  $\dot{\epsilon}_p = 0.0015/s$  and (b)  $\dot{\epsilon}_p = 0.15/s$  strain rate.

However, when it comes to the thermomechanical response due to the activation of DSA, the VA model is inefficient. As stated earlier; to capture the activation of DSA, the effect of solute-dislocation interactions must be accounted for along with the increase in the solute concentrations at local obstacles that impedes the dislocation movement. Figure 35 (a & b) and Figure 36 (a & b) compares the model prediction with and without the DSA stress component at 523 K and 723 K respectively.

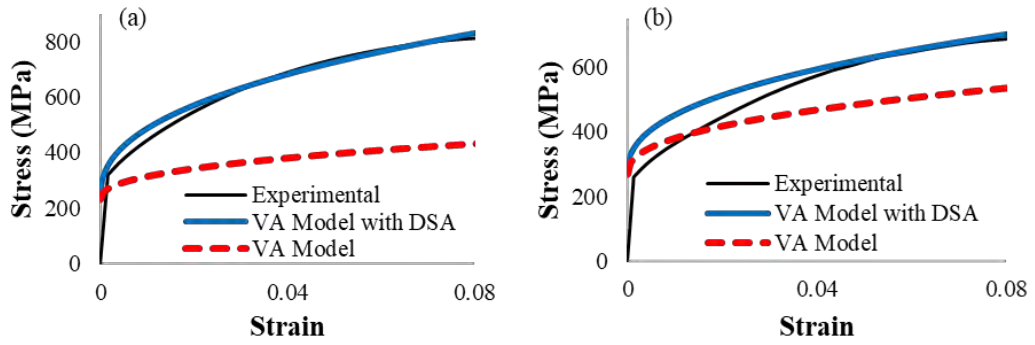


Figure 35 Stress-Strain curves for original VA model, modified VA model, and experimental data at  $T = 523\text{K}$  and (a)  $\dot{\epsilon}_p = 0.0015/\text{s}$  and (b)  $\dot{\epsilon}_p = 0.15/\text{s}$  strain rate.

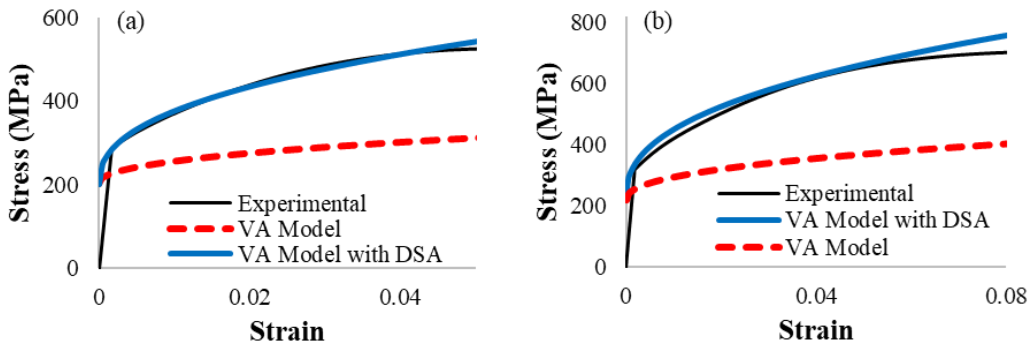


Figure 36 Stress-Strain curves for original VA model, modified VA model, and experimental data at  $T = 723\text{K}$  and (a)  $\dot{\epsilon}_p = 0.0015/\text{s}$  and (b)  $\dot{\epsilon}_p = 0.15/\text{s}$ .

The VA model does not account for the damage incorporated in a material once it crosses the ultimate strength and hence the stress keeps on rising with increase in plastic strain. To account for the damage incorporated in the material, the energy-based damage evolution model has been incorporated with the VA model as discussed in the next section.

#### 4.6. Damage Modeling

Whenever a material is deformed plastically and approaches failure, there is permanent deformation in the material that results in the loss of material capability to bear stress. This degradation of mechanical properties is termed as damage in the material which is a process related to the microstructural features of the material and has been reported in different studies [21, 33-41]. Utilizing the relationship between

the damaged and undamaged flow stress (Eqn. (24)), the effect of damage evolution model was incorporated in the modified VA constitutive model with DSA for MMFX (Figure 37) and C45 steel (Figure 38 and Figure 39).

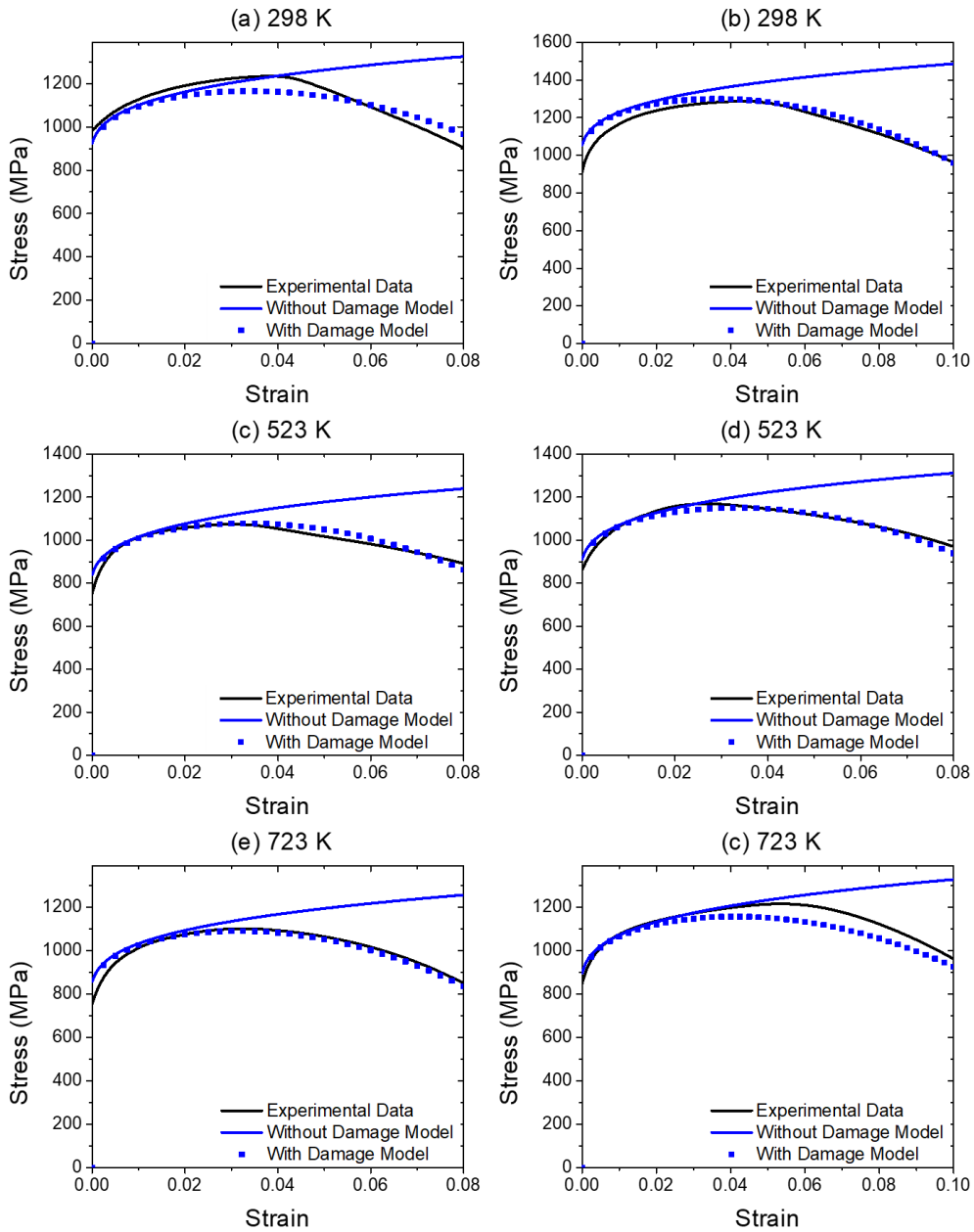


Figure 37 Comparison of the stress-strain curves obtained through the modified constitutive model at different temperatures and strain rate of (a, c, and e) 0.0015/s and (b, d, and f) 0.15/s in the presence and absence of damage parameter with the experimental data.

Figure 37 shows the effect of incorporation of damage parameter in the modified VA model for MMFX steel in comparison to the model without damage at  $\dot{\epsilon}_p = 0.0015/s$

and 0.15/s for different temperatures. Though the modified VA model was able to predict the flow stress, the inclusion of damage model has enhanced the effectiveness of the modified VA model even after the ultimate stress by capturing the material deformation behavior in MMFX steel.

Likewise, a comparison was between the experimental and numerical results after incorporating the damage evolution parameter. The results demonstrate that the inclusion of damage parameter has enhanced the accuracy of the modified VA model for C45 steel. Considering the lower strain rates i.e., at  $\dot{\epsilon}_p = 0.0015/s$  (Figure 38), and the higher strain rates i.e., at  $\dot{\epsilon}_p = 0.15/s$  (Figure 39), the results obtained for the constitutive model, accounting for both DSA and damage incorporation, exhibited excellent comparison with the experimental results. Notably, it can be seen that that the model combined with damage evolution parameter was able to give more accurate results due to its ability of capturing the material deformation beyond the ultimate stress point.

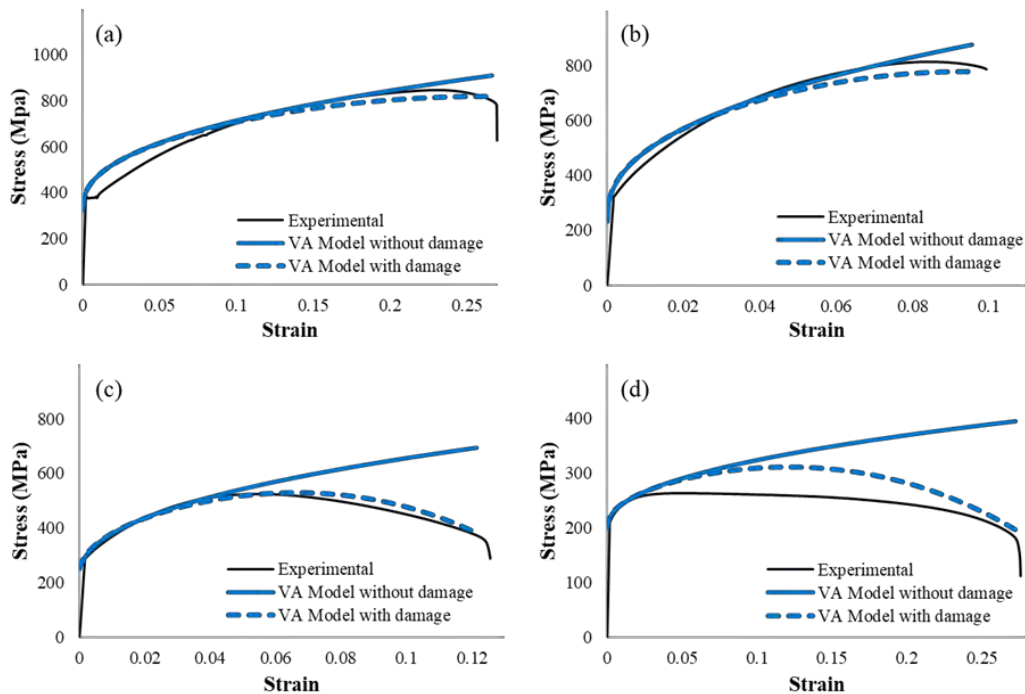


Figure 38 Modified VA Model with and without the damage parameter compared to experimental data at  $\dot{\epsilon}_p = 0.0015/s$  and (a)  $T = 298\text{ K}$ , (b)  $T = 523\text{ K}$ , (c)  $T = 723\text{ K}$ , (d)  $T = 923\text{ K}$ .

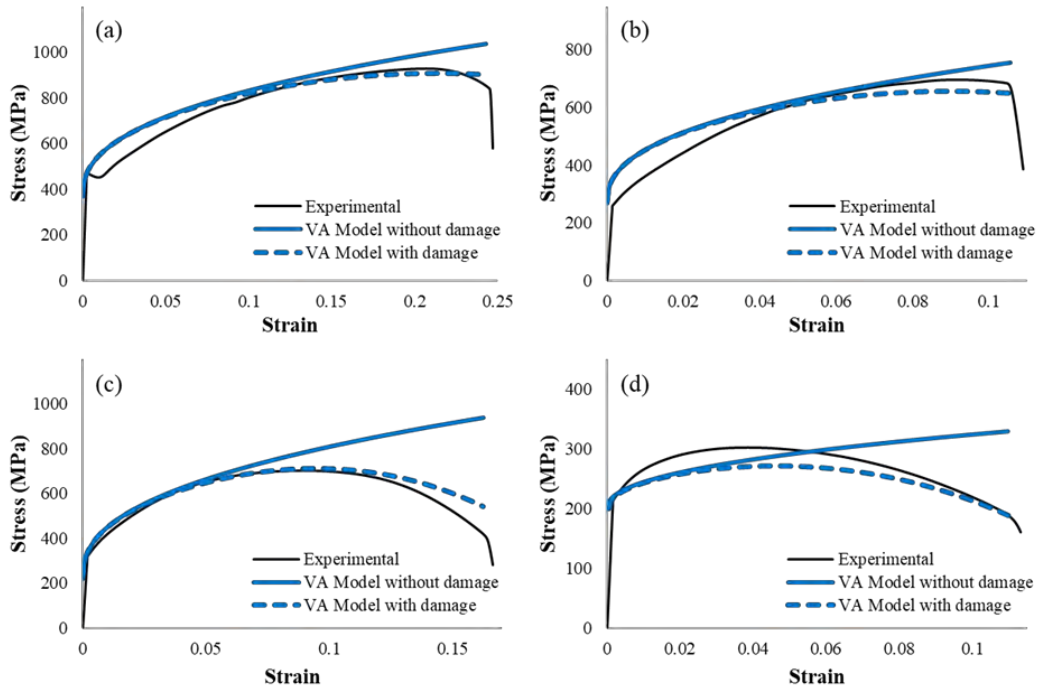


Figure 39 Modified VA Model with and without the damage parameter compared to experimental data at  $\dot{\epsilon}_p = 0.15/s$  and (a)  $T = 298$  K, (b)  $T = 523$  K, (c)  $T = 723$  K, (d)  $T = 923$  K.

## Chapter 5. FE Modelling

The FE simulations were performed by integrating the modified constitutive VA model, which had been previously developed, into ABAQUS using a user-defined material subroutine called VUMAT. A uniaxial tension problem was solved using a mesh which involves a single axisymmetric element. The entire sample is given in Figure 40(a) and, considering its symmetry, just one-quarter of the problem is considered (Figure 40 (b)) which also shows the boundary conditions. This element was subjected to loading conditions with different displacement velocities (strain rates) and Figure 40 (c) depicts the loading history, which allows for executing the test at a precise and consistent strain rate.

The numerical problem demonstrated the ability of the FE formulation to precisely reflect the activation of DSA in response to variations in strain rates and temperatures on the stress-strain curves, as compared to the experimental data. The results presented in this section are based on the simulations carried out on the different metals and alloys studied in this dissertation and accurately align with the experimental data, effectively predicting the temperature range at which DSA activates under different strain rates.

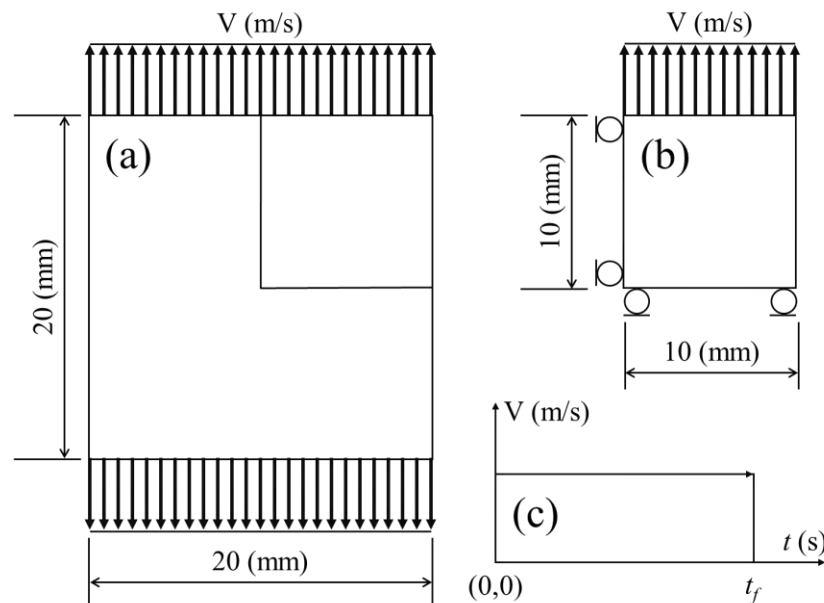


Figure 40 Sketch of the uniaxial sample tested in FE simulations. (a) The loaded sample. (b) Quarter of the problem. (c) Applied loading profile

## 5.1. CP-Niobium

As discussed before, CP-Nb is one of the most commonly used alloying elements in different industrial applications. Figure 41 compares the results obtained for the constitutive model and the FE simulations at the strain rate 0.001/s for CP-Nb. Figure 41(a) shows that the stress-temperature results obtained by the FE simulations are very consistent with the constitutive model and the experimental data. This signifies that the stress computed through FE code developed in VUMAT is in line with the constitutive model results.

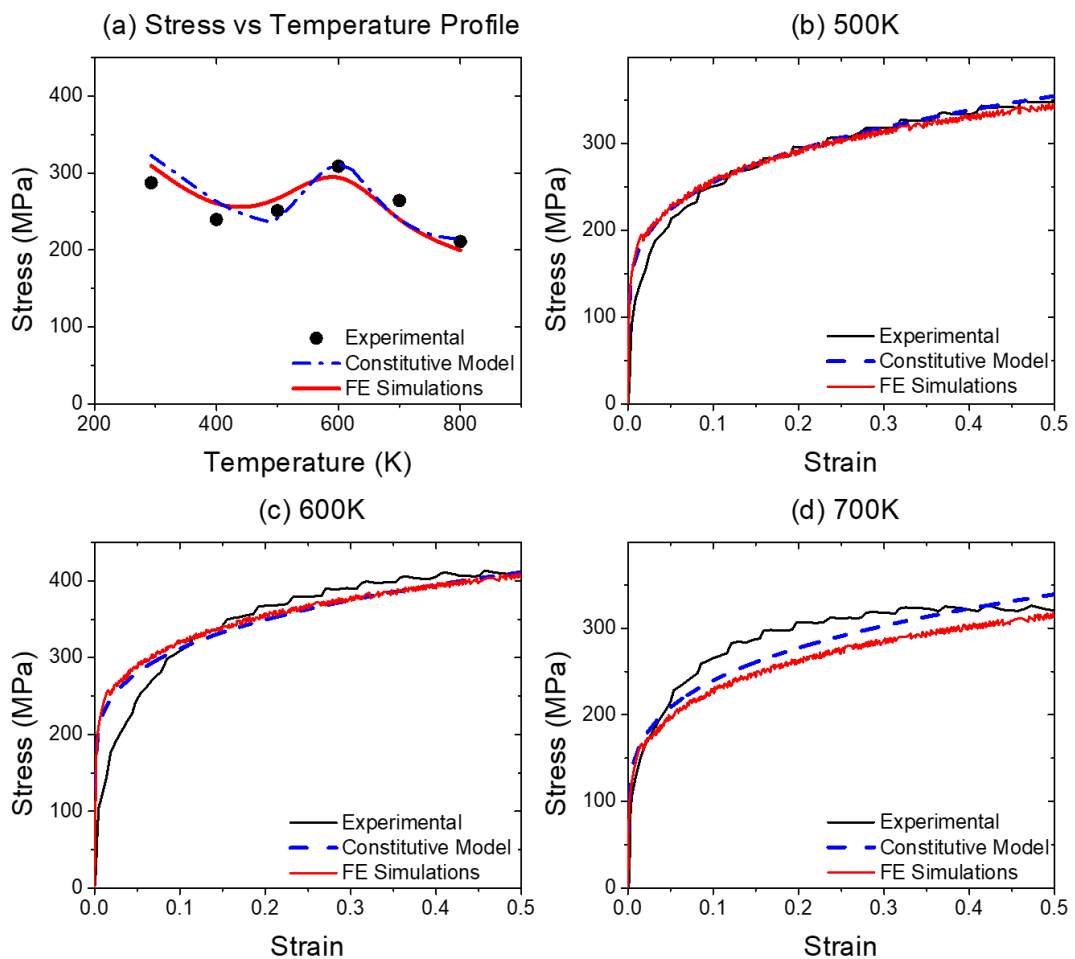


Figure 41 Comparison of the experimental stress against the flow stress obtained using the constitutive model and FE simulations for CP-Niobium. At a strain rate of 0.001/s, (a) gives the stress vs temperature profile while (b), (c), and (d) gives the stress-strain comparison at 500K, 600K, and 700K respectively.

This can also be observed with stress strain profiles given in Figure 41 (b, c, and d). Stress strain curves were obtained for FE simulations when the single element sample

was loaded at different temperatures (i.e., 500K, 600K and 700K) at the strain rate of 0.001/s in the DSA activation region. The results obtained gave a reasonable comparison with the experimental data and the constitutive model results as can be seen in Figure 41.

## 5.2. CP-Vanadium

The simulation performed for CP-Vanadium also gave comparable results as given in Figure 42 at the strain rate 0.001/s. Figure 42(a) shows that the stress-temperature results obtained by the FE simulations are very consistent with the constitutive model and the experimental data. This signifies that the stress computed through FE code developed in VUMAT is in line with the constitutive model results.

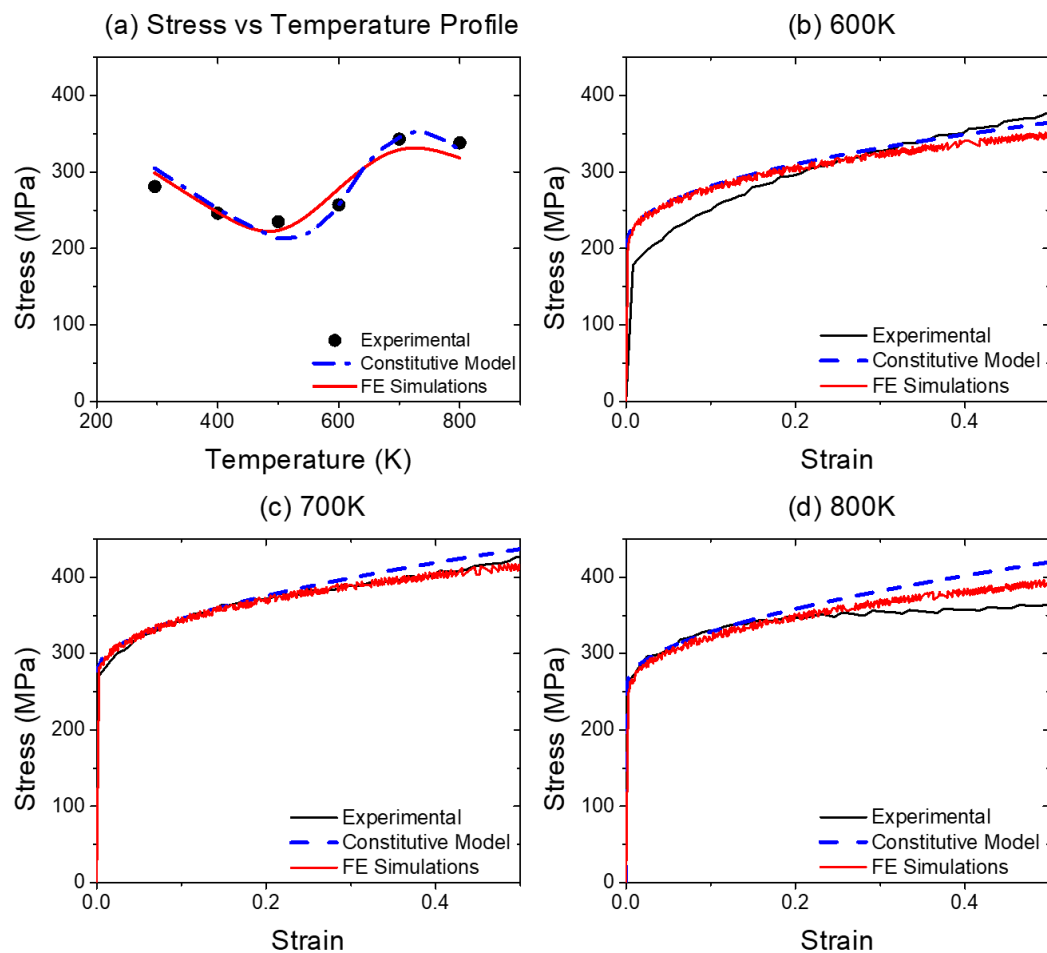


Figure 42 Comparison of the experimental stress against the flow stress obtained using the constitutive model and FE simulations for CP-Vanadium. At a strain rate of 0.001/s, (a) gives the stress vs temperature profile while (b), (c), and (d) gives the stress-strain comparison at 600K, 700K, and 800K respectively.

This can also be observed with stress strain profiles given in Figure 42 (b, c, and d). When the single element sample was loaded at different temperatures (i.e., 600K, 700K, and 800K) at the strain rate of 0.001/s in the DSA activation region, the FE simulations gave stress-strain curves which are very much comparable to the experimental data and the constitutive model results.

### **5.3. CP-Titanium**

As previously discussed, CP-Titanium exhibited DSA over a broad range of strain rates and temperatures. DSA was observed both at low and high strain rates. Therefore, FE simulations were carried out at both these strain rates (i.e., 0.001/s and 2200/s).

Figure 43 shows the stress-strain comparison of the constitutive (blue line) and numerical (red line) model results in comparison to the available experimental data. As can be seen, the FE simulations result align well with the constitutive model results. Moreover, the simulations predicted accurate results in comparison to the experimental data. This means that the numerical integration carried out to develop the VUMAT subroutine is giving accurate results.

Moreover, the results were not valid only at a lower strain rate but the high strain rate results in the absence and presence of DSA gave equally accurate results (Figure 44). Moreover, the adiabatic heating effect was also successfully incorporated into the FE code, which helped in successful predictions of the stress-strain profile both in the absence and presence of DSA.

### **5.4. MMFX Steel**

Figure 45(a and b) presents a comparison between the experimental data and the flow stress calculated by the constitutive model and the FE simulations for MMFX steel. This comparison is done at various temperatures and strain rates at the yield point.

The results indicate that the VA model with DSA effectively predicts the temperature range for DSA activation under varying strain rates, while also precisely capturing the rise in flow stress caused by the segregation of solute atoms along the line of dislocations.

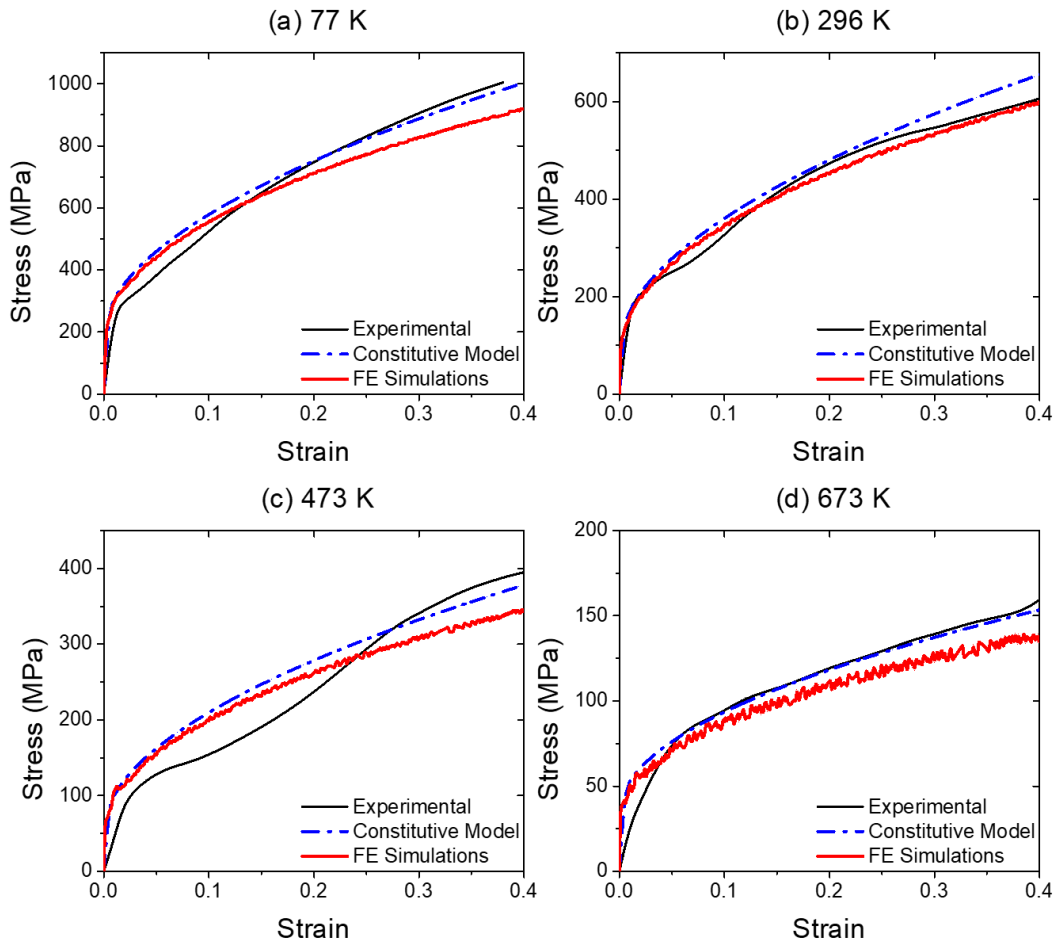


Figure 43 Comparison of the experimental stress against the flow stress obtained using the constitutive model and FE simulations for CP-Titanium at a strain rate of 0.001/s, and temperatures of (a) 77K, (b) 296K, (c) 473K and (d) 673K.

Moreover, the stress-strain curves derived from the constitutive and finite element (FE) models, under varying temperatures and strain rates (as shown in Figure 46 and Figure 47) exhibit accurate results with comparison to the experimental data. Figure 46(a-d) presents a comparison of the experimental data obtained at a strain rate of 0.0015/s. As can be seen, no DSA was present at 298K temperature. But with increase in temperatures, DSA activated (Figure 46(b and c) due to the diffusion activated interactions of the solute atoms with the dislocations. The constitutive model accurately represented this, and the finite element simulations yielded comparable outcomes.

In addition, the FE model also yielded similar results when tested at a higher strain rate of 0.15/s (Figure 47(a-d)). The results presented clearly shows the effectiveness

of the FE generated simulations in comparison to the constitutive model and the experimental data. It can be observed that the flow stress increased in the activation regions of DSA and both the constitutive and numerical models captured this successfully.

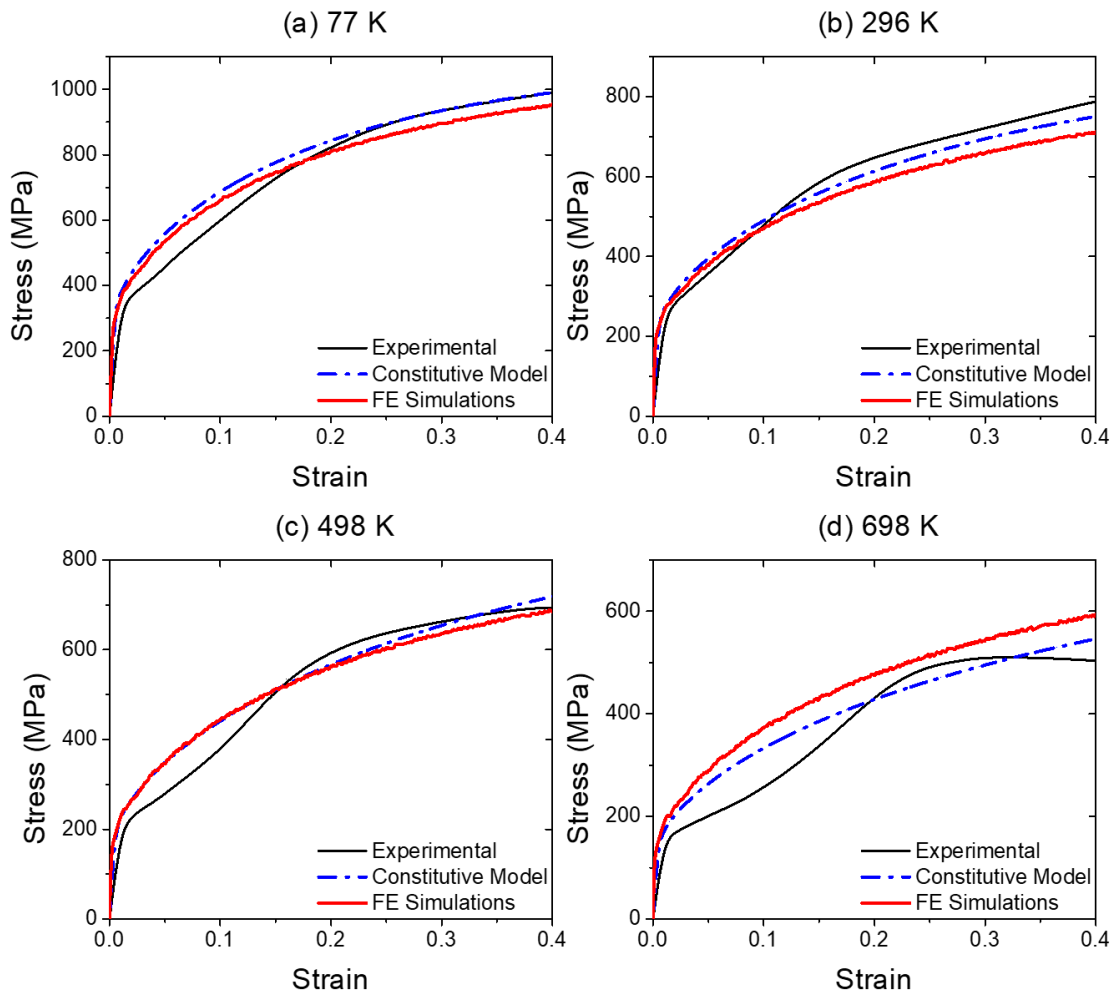


Figure 44 Comparison of the experimental stress against the flow stress obtained using the constitutive model and FE simulations for CP-Titanium at a strain rate of 2200/s, and temperatures of (a) 77K, (b) 296K, (c) 473K and (d) 673K.

Based on the findings shown in Figure 45, Figure 46, and Figure 47, it is evident that both the constitutive model and the FE model accurately predicted the temperature ranges for activation of DSA at various strain rates. The FE simulations were able to accurately predict and capture the activation of DSA. In addition, the modified VA model effectively captures the increase in flow stress by considering the effect of solute concentration.

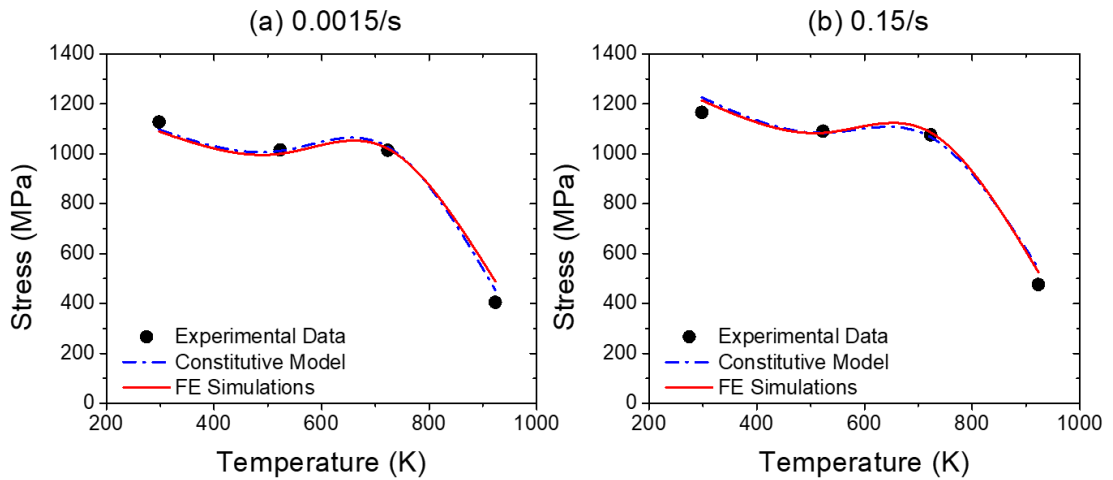


Figure 45 Stress-Temperature profile obtained through the constitutive model for MMFX steel and the FE simulations and its comparison with the experimental data at a strain rate of (a) 0.0015/s and (b) 0.15/s.

### 5.5. C45 Steel

Figure 48 (a and b) compares the experimental data with the flow stress computed by the constitutive model and the FE simulations at different temperatures and strain rates at a plastic strain of 4%. The results show that the modified VA model not only predicts the temperature region for DSA activation at different strain rates, but also accurately captures the increase in flow stress due to segregation of solute atoms along dislocation.

Furthermore, the stress-strain curves, obtained from constitutive and FE model, at different temperatures and strain rates (Figure 49 and Figure 50) also show comparable results with the experimental data. Figure 49 (a-d) compares the experimental data at a strain rate of 0.0015/s. At low temperature (298K), there was no activation of DSA. But with increase in plastic strain, DSA activated at higher temperatures (Figure 49 (b and c)) owing to the diffusion of the carbon atoms and their interaction with dislocations. This was accurately captured by the constitutive model and the FE simulations predicted similar results.

Moreover, the FE model also predicted comparable results at a higher strain rate of 0.15/s (Figure 50(a-d)). There was a less increase in the flow strength at 523K as the starting temperature for DSA activation at this strain rate is around 500K. However,

with increase in temperature, the flow stress increases greatly as the solute concentration along the dislocation core increases.

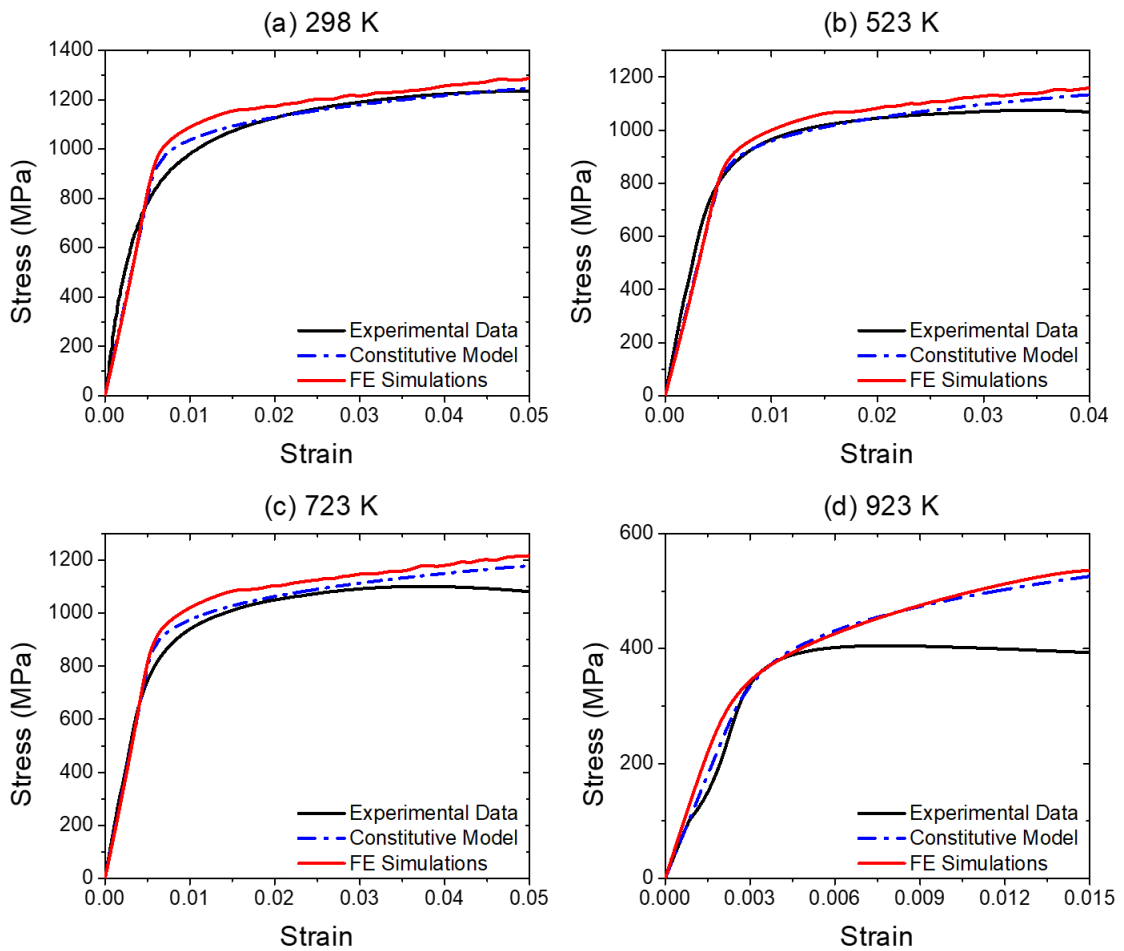


Figure 46 Stress-Strain profiles obtained through the constitutive model and the FE simulations for MMFX steel in comparison to the experimental data at a strain rate of 0.0015/s and temperatures of (a) 298 K, (b) 523 K, (c) 723 K, and (d) 923 K.

By the results presented in Figure 48, Figure 49, and Figure 50, it can be clearly observed that the constitutive model and the FE model successfully predicted the DSA activation temperature ranges accurately at different strain rates. The model accurately predicted the temperature regions for activation of DSA both at the low and high strain rates. Also, the increase in flow stress was effectively captured owing to the solute concentration parameter defined in the constitutive model. These results for single element simulations validate the accuracy of the developed VUMAT code which is tested for numerical problems such as necking and shearing in the next section.

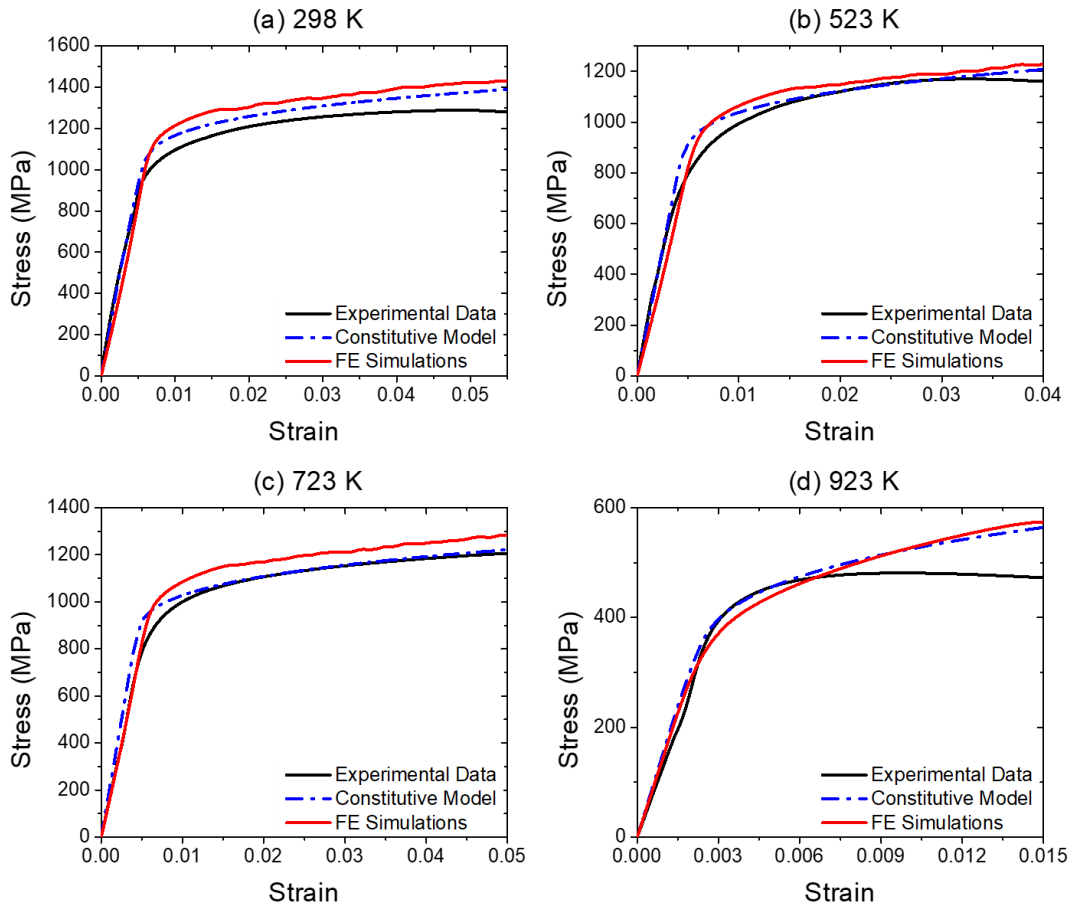


Figure 47 Stress-Strain profiles obtained through the constitutive model and the FE simulations for MMFX steel in comparison to the experimental data at a strain rate of 0.15/s and temperatures of (a) 298 K, (b) 523 K, (c) 723 K, and (d) 923 K.

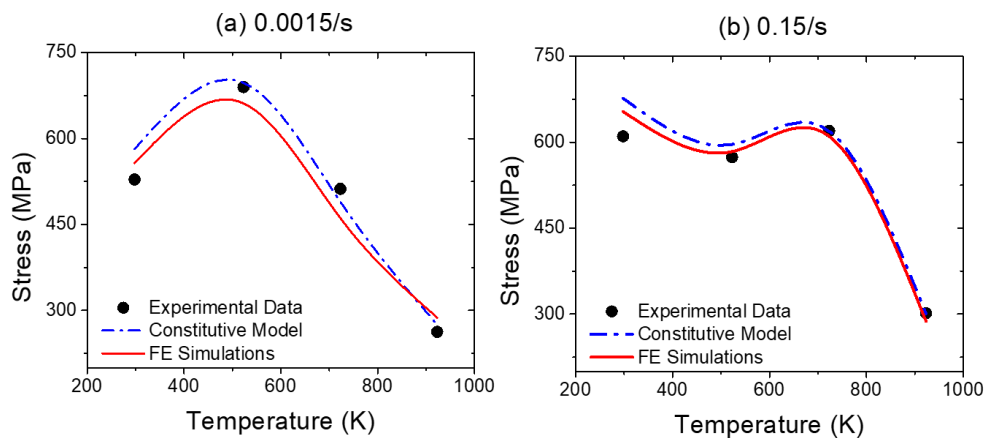


Figure 48 Comparison of the flow stress at different temperatures and  $\dot{\epsilon}_p$  of (a) 0.0015/s and (b) 0.15/s for C45 steel.

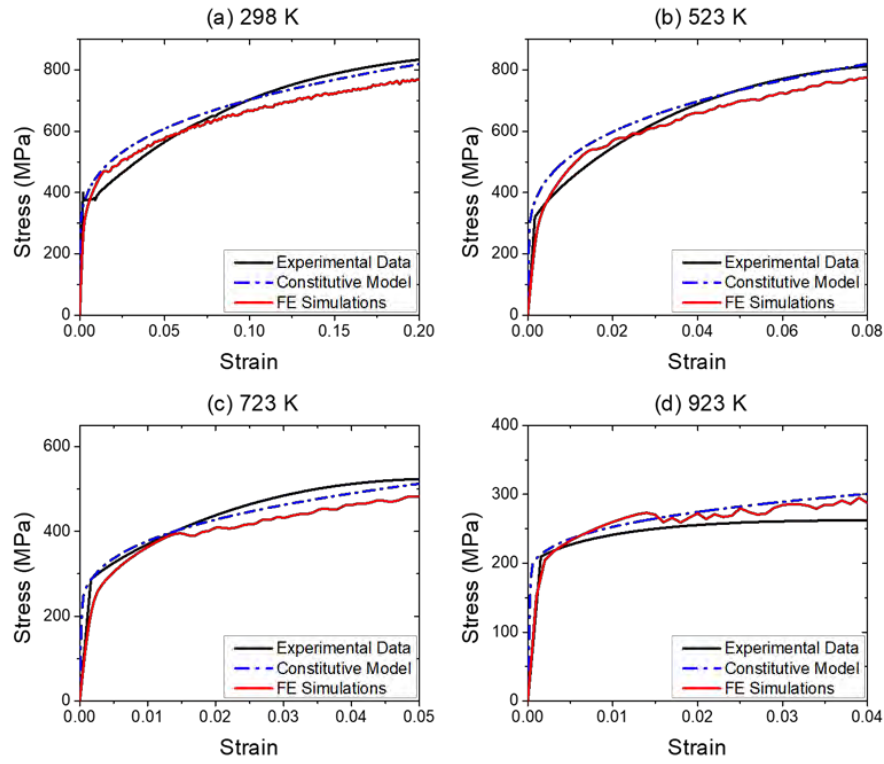


Figure 49 Comparison of the stress-strain profile at  $\dot{\epsilon}_p = 0.0015/s$  and  $T =$  (a) 298K, (b) 523K, (c) 723K, and (d) 923K for C45 steel.

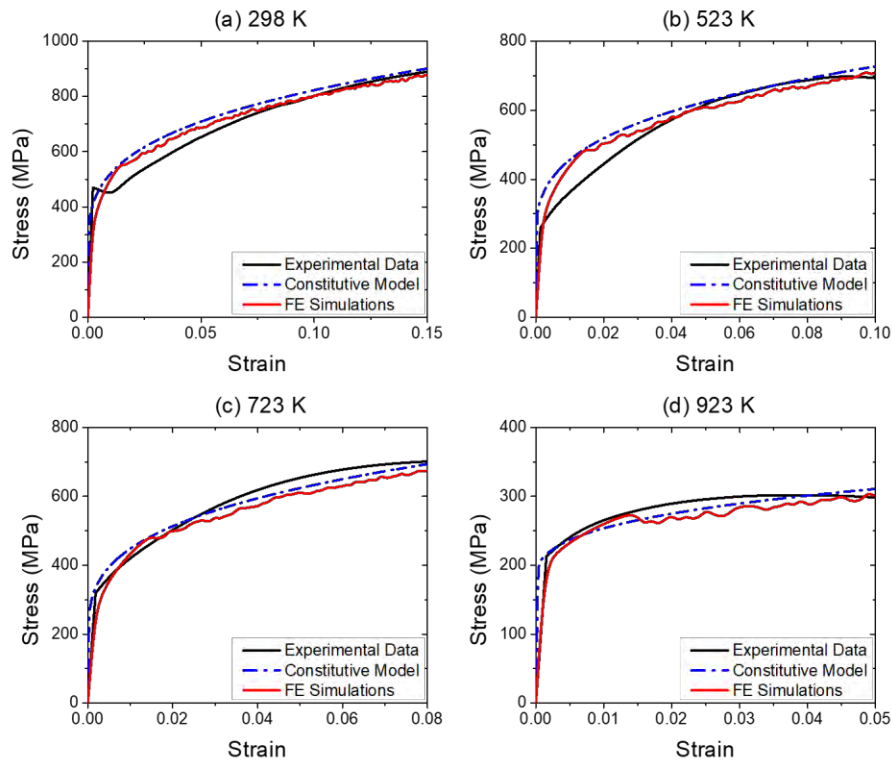


Figure 50 Comparison of the stress-strain profile at  $\dot{\epsilon}_p = 0.15/s$  and  $T =$  (a) 298K, (b) 523K, (c) 723K, and (d) 923K for C45 steel.

## Chapter 6. Numerical Examples

This chapter simulates real-time examples related to the mechanical testing of metals. A uniaxial tensile test is simulated in the activation region of DSA for both the models. The effect of necking is studied by introducing a geometrical defect in the sample tested. Moreover, shear localization is intensified due to the activation of DSA. This has been verified by simulation of a hat shaped axisymmetric problem. Both these examples indicate that the activation of DSA leads to an early failure of the metals as discussed below:

### 6.1. Necking Problem

Necking problem was analyzed using an axisymmetric cylindrical sample. A circular bar was subjected to uniaxial thermomechanical loading scenarios reported to exhibit DSA in different metals and alloys. A fourth of the sample was modelled with a 7 x 30 mesh size four-node axisymmetric element (CAX4R type). A 1% radius reduction geometric flaw introduced into the bar caused necking in the middle (Figure 51).

The actual mesh geometry used for simulations is presented in Figure 52 where the quarter of the sample subjected to the thermomechanical loading is given Figure 52 (a) while Figure 52 (b) gives the whole cylindrical sample that was subjected to necking during tensile loading.

The effect of dynamic strain aging was studied to find the reduction in the cross-sectional area along the neck when uniform tensile loading is applied. In all the materials tested in this loading scenario, it was found that the stress accumulation due to dynamic strain aging resulted in an earlier failure of the material in comparison to the scenario where there was no DSA under the same thermomechanical loading conditions. The different metals tested under this loading condition are discussed in this chapter as follows:

#### 6.1.1. CP-Niobium

As discussed previously, when DSA is activated, there is an increase in the strength of the metals. This rise is due to the segregation of solute atoms along dislocation core

which resist deformation. Consequently, the material reaches its UTS at an earlier stage than its expected plastic deformation time. The necking application highlights this phenomenon.

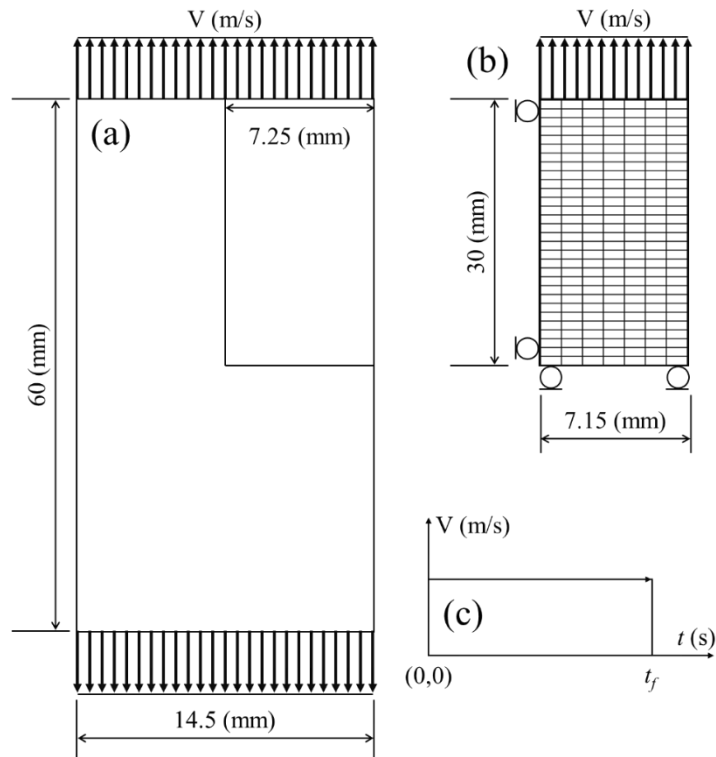


Figure 51 Sketch of the uniaxial sample tested in FE simulations for necking problem. (a) The loaded sample. (b) Quarter of the problem with mesh (7 x 30). (c) Applied loading profile.

Axial tensile velocity of  $3 \times 10^{-5}$  m/s (corresponding to a strain rate of 0.001/s) is applied for a total time step of 200s (equal to an elongation of  $6\text{mm} = 3 \times 10^{-5}$  m/s  $\times$  200s) at two different temperatures (600K and 700K). The resultant deformed shapes, both with and without DSA, are depicted in Figure 53 and Figure 54 for 600K and 700K respectively. The x-direction displacement patterns of the deformed objects exhibit a decrease in radius at the necking region.

In general, the samples that exhibited DSA demonstrated a greater decrease in the neck radius. When Nb was subjected to tensile loading scenario in the activation region of DSA, it showed that its ability to plastically deform was reduced. This was observed when a comparison was made between the deformed shape in the absence

and presence of DSA. The sample was loaded in the previously reported activation region of DSA i.e., at a strain rate of 0.001/s for 200s and temperature of 600K (Figure 53) and 700K (Figure 54).

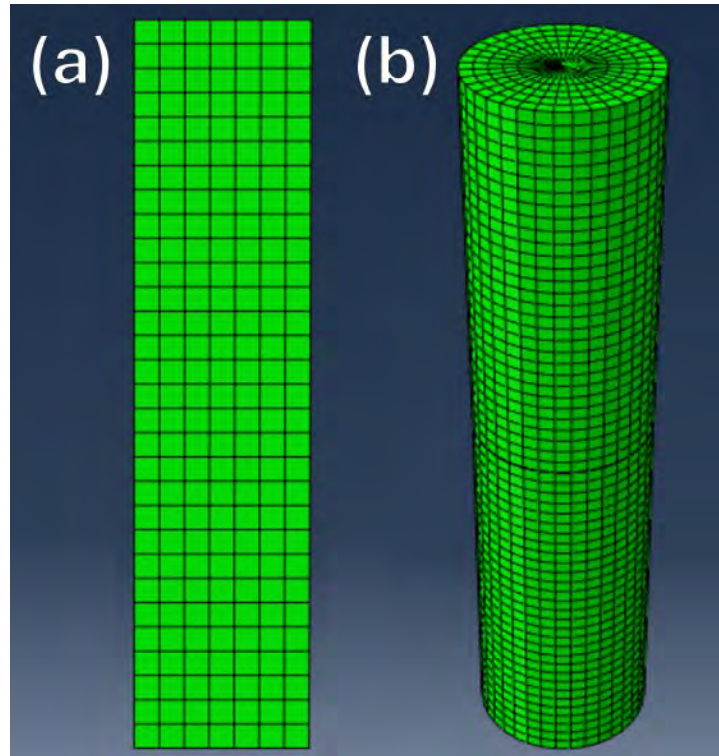


Figure 52 Mesh geometry for the necking problem where (a) gives the quarter of the axisymmetric sample while (b) shows the complete cylindrical sample subjected to the necking application.

When DSA was not taken into consideration, the necking phenomenon was not very highlightable even after 200s (Figure 53(a) and Figure 54(a)). On the contrary, when the DSA activation was considered, a significant reduction in the necking region was observed (Figure 53(b) and Figure 54(b)). The activation of DSA amplified the reduction in neck radius thus indicating an earlier failure in the material (Figure 53(c) and Figure 54(c)).

This may be attributed to increase in metal viscosity due to segregation of solute atoms along dislocations which results in pinning and ultimately increase the strength of the metal. Therefore, with increase in metallic strength, Nb loses its ductility (which is the ability of material to deform before breakage [98]), that causes earlier necking in the metal (Figure 53(d) and Figure 54(d)). This can be further verified in

(Figure 53(e) and Figure 54(e)), where a comparison for plastic deformation is made in the presence and absence of DSA. Although the effect is not sharply contrasted, it can be observed that the ability of Nb to deform plastically decreases with an increase in longitudinal strain in the presence of DSA which indicates that the ductility of the material reduces when DSA activates.

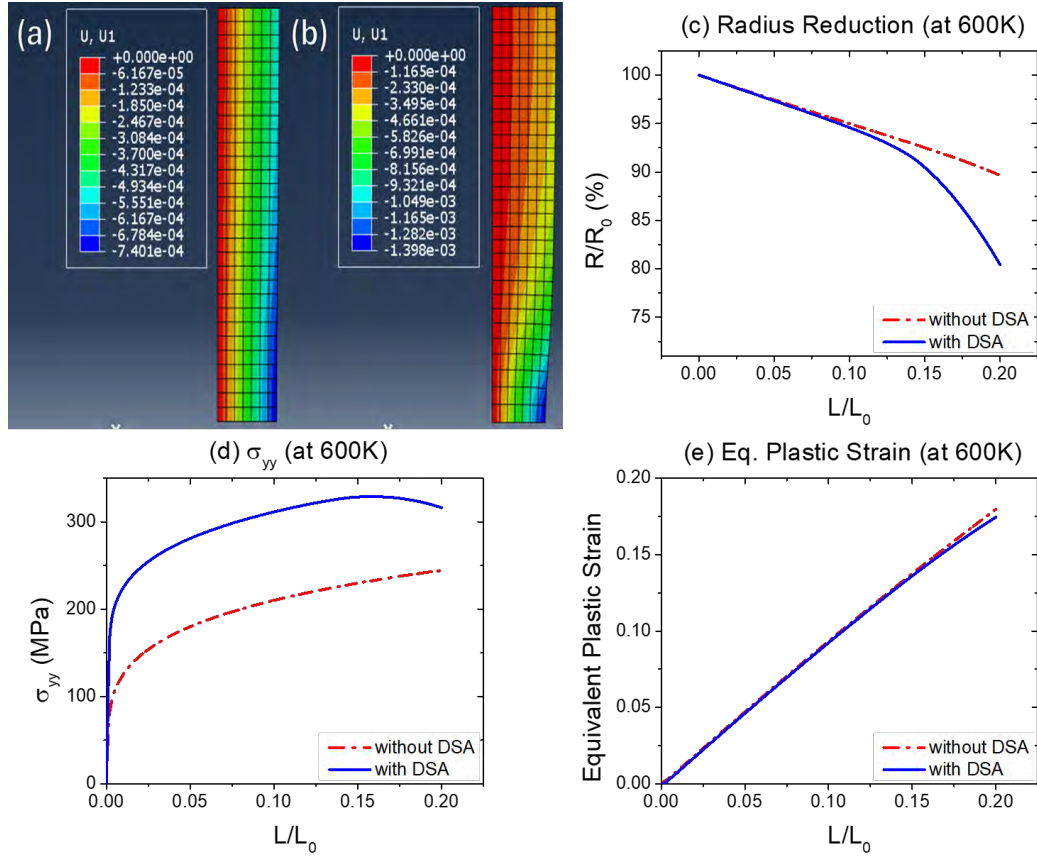


Figure 53 Deformed Nb sample at  $\dot{\epsilon}_p = 0.001/s$  and  $T = 600$  K in the (a) absence and (b) presence of DSA. (c) Radius reduction, (d) Longitudinal stress, and (e) Equivalent plastic strain against the longitudinal strain with and without DSA.

### 6.1.2. CP-Vanadium

Just like CP-Nb, when CP-Vanadium was subjected to the same tensile loading scenario in the activation range of DSA, it showed that its ability to plastically deform was reduced. The deformed shapes resulting from the simulation, with and without DSA, are shown in Figure 55(a) and Figure 56(a) at temperatures of 600K and 700K, respectively.

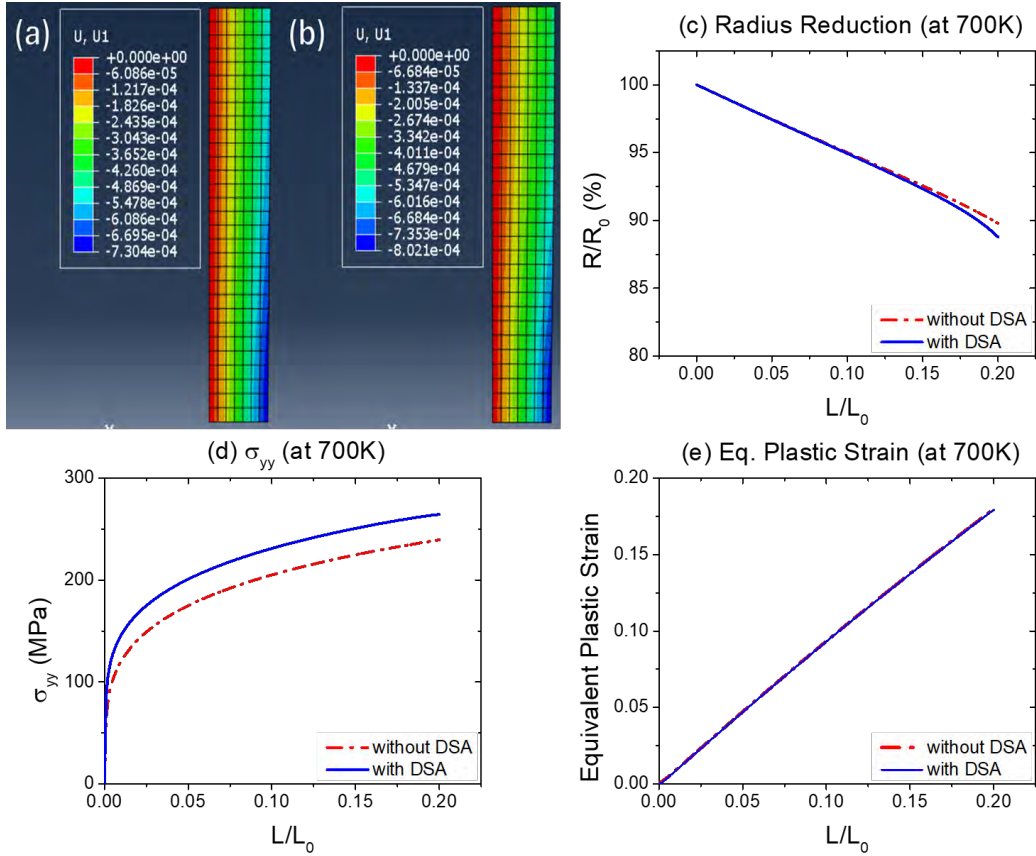


Figure 54 Deformed Nb sample at  $\dot{\epsilon}_p = 0.001/s$  and  $T = 700$  K in the (a) absence and (b) presence of DSA. (c) Radius reduction, (d) Longitudinal stress, and (e) Equivalent plastic strain against the longitudinal strain with and without DSA.

When the effects of DSA were not considered, the necking phenomena was not very prominent even after 200 seconds, as shown in Figure 55 (a) and Figure 56(a). In contrast, the activation of DSA resulted in a notable decrease in the necking region, as depicted in Figure 55 (b) and Figure 56(b).

The effect of DSA on necking reduction with increase in plastic strain is also presented in Figure 55 (c) and Figure 56(c). A significant drop in the neck radius occurs in the presence of DSA, which indicates that the activation of DSA intensified the decrease in neck radius, hence leading to an earlier failure of the material (Figure 55 (d) and Figure 56(d)).

As previously mentioned, this phenomenon is caused by the rise in metal viscosity caused by the diffusion of solute atoms along dislocations. This segregation leads to pinning and, thus, an increase the metal's strength. Consequently, when the metallic strength of V increases, its ductility decreases, and it undergoes less plastic

deformation (Figure 55 (e) and Figure 56(e)). This also indicates that DSA introduces brittleness in the metal, that results in an earlier necking of the metal.

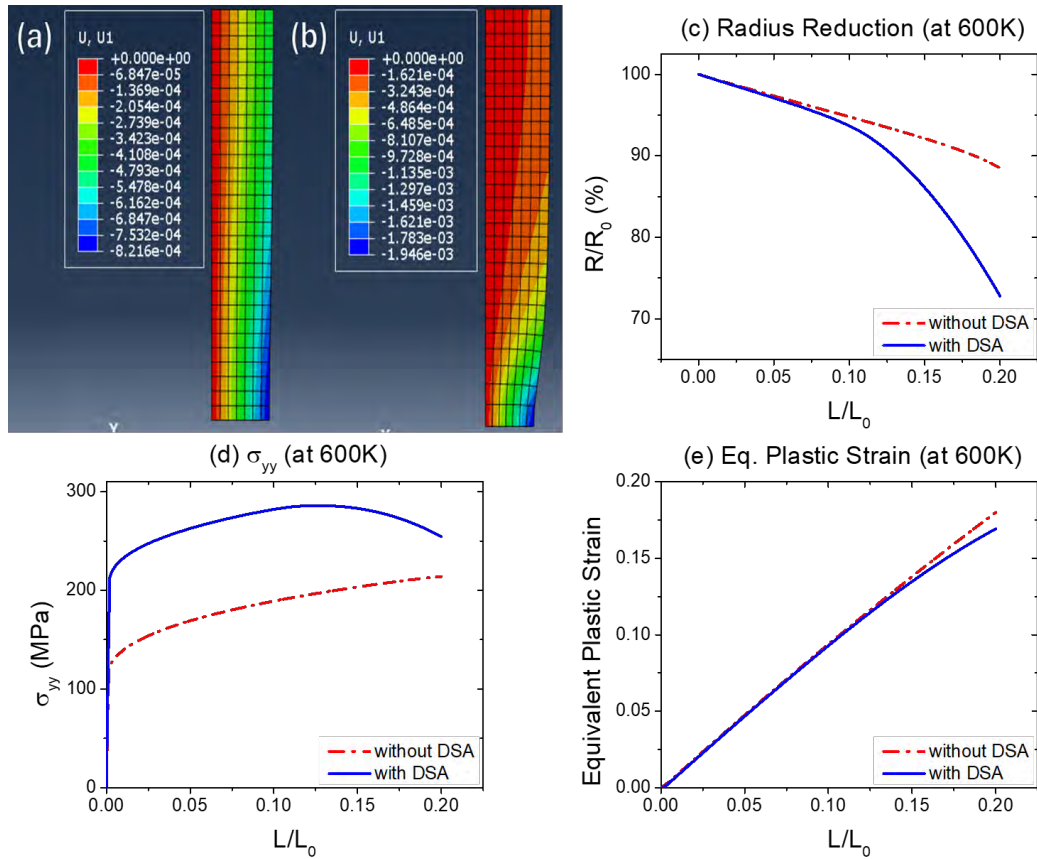


Figure 55 Deformed V sample at  $\dot{\epsilon}_p = 0.001/s$  and  $T = 600\text{ K}$  in the (a) absence and (b) presence of DSA. (c) Radius reduction, (d) Longitudinal stress, and (e) Equivalent plastic strain against the longitudinal strain with and without DSA.

## 6.2. Shear Hat Problem

The effect of DSA on shear properties was analyzed using a cylindrical hat-shaped sample. The dimensions of the sample were chosen with the expectation that the brim's inner radius and the hat radius match. The schematic of the sample along with sample dimensions is given in Figure 57(a), while the undeformed section view of the axisymmetric hat-shaped sample is given in Figure 57(b). The growth of shear localization was analyzed along the path given in Figure 58 where the loading scenario is also indicated. The location of the shear localization is forced to be in the shear zone to study the effect of DSA on shear failure mechanisms. The different metals studied for this scenario and their analysis is given in the subsequent sections.

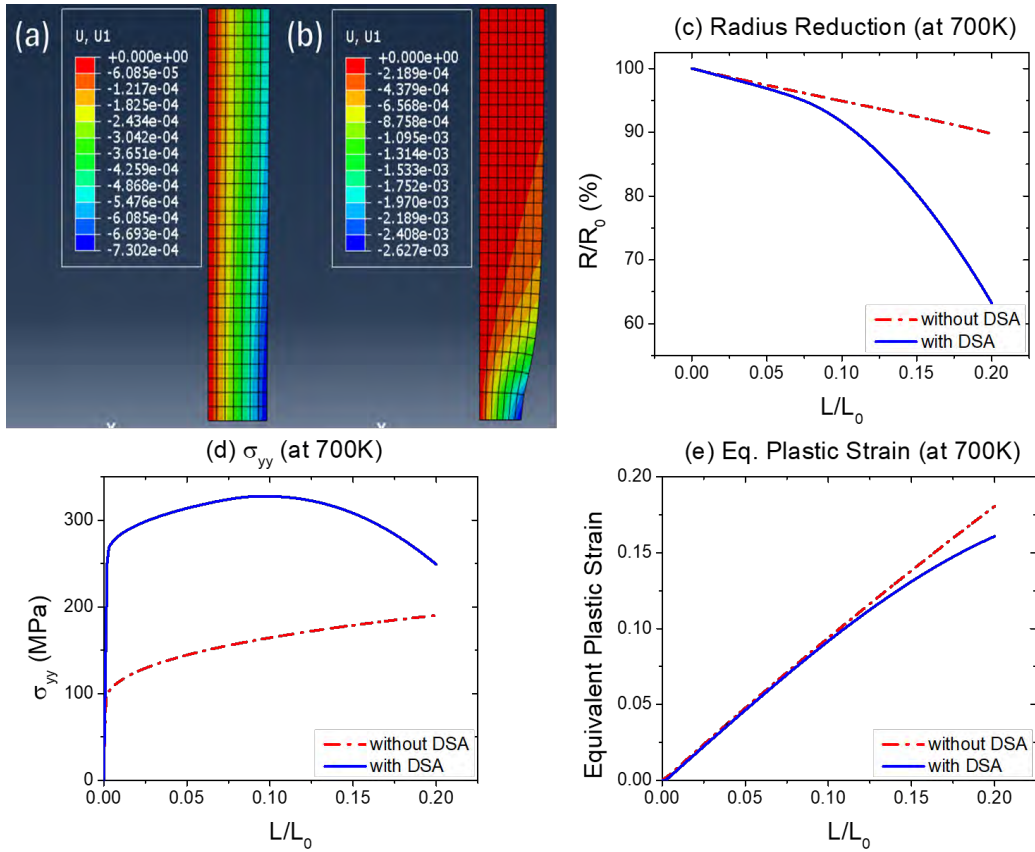


Figure 56 Deformed V sample at  $\dot{\epsilon}_p = 0.001/s$  and  $T = 700\text{ K}$  in the (a) absence and (b) presence of DSA. (c) Radius reduction, (d) Longitudinal stress, and (e) Equivalent plastic strain against the longitudinal strain with and without DSA.

### 6.2.1. BCC Niobium

Results for the axisymmetric shear hat sample at  $0.001/s$  strain rate are presented in Figure 59 and Figure 60 for 600K and 700K temperatures, respectively. These loading scenarios were specifically chosen considering the DSA activation range discussed previously. The deformed sample shows that localized shear bands were observed within the shear zone indicating that the sample was purely loaded in shear deformation mode (Figure 59(a) and Figure 60(a)).

The distribution of equivalent plastic strain along the specified path indicates strain localization in the shear zone (Figure 59(b)). When the effect of DSA was studied, an increase in the strain localization was observed. This increase in strain localization increases the likelihood of crack initiation due to brittleness caused by the DSA. The diffusion of impurity atoms along the dislocations makes their movement difficult that

leads to an increase in metal viscosity. As discussed earlier, this reduces the ability of the material to deform plastically which leads to earlier failure of material.

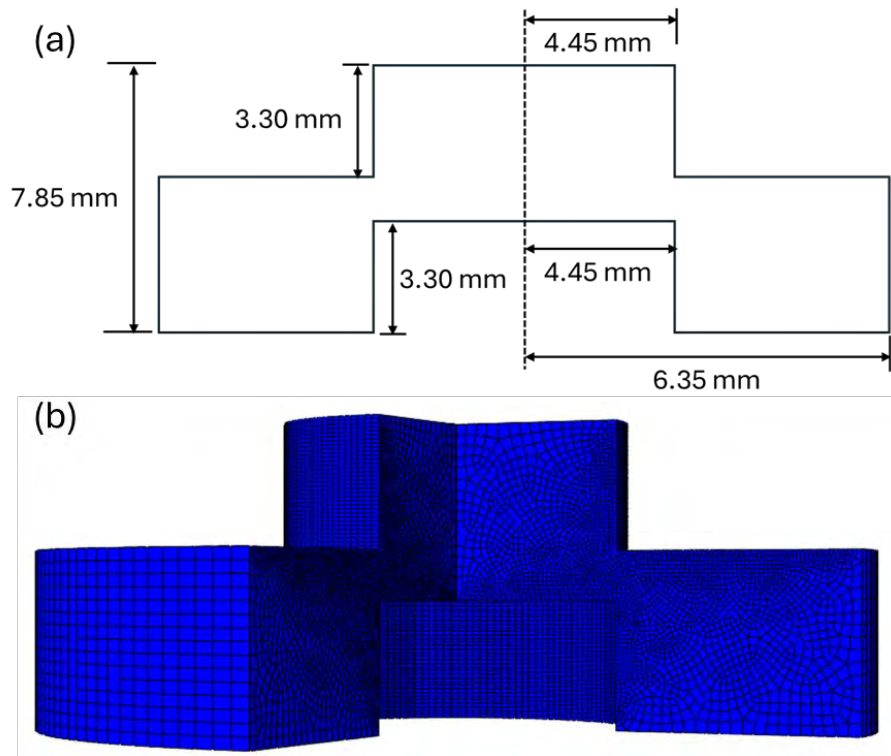


Figure 57 (a) Sketch, and (b) section view of the axisymmetric hat-shaped sample

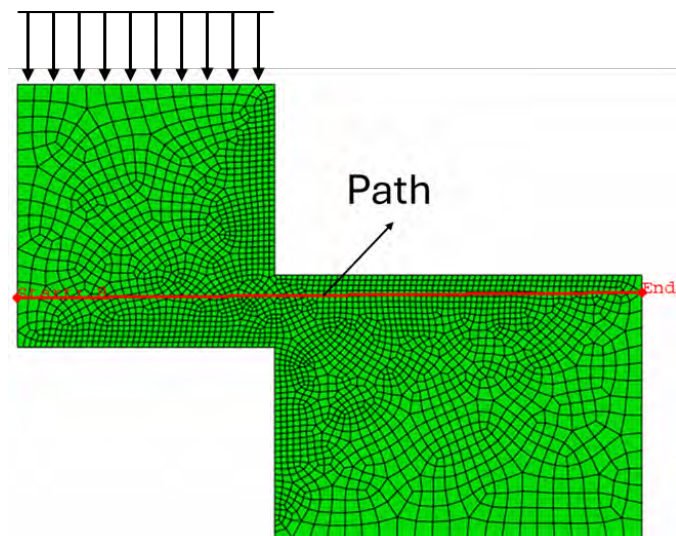


Figure 58 Path specified for the shear localization due to axial loading conditions

When the load was applied, the displacement profile was identical in the beginning. However, when DSA was activated, with further increase in deformation, a prominent increase in the nodal displacement was observed. This can be attributed to the formation of cracks in the sample that accounts for a drop in material strength. The initiation and propagation of cracks reduce the load bearing capability of the material. This leads to material failure and a rapid increase in deformation is observed which is also indicated by the nodal displacement profile given in Figure 59(c).

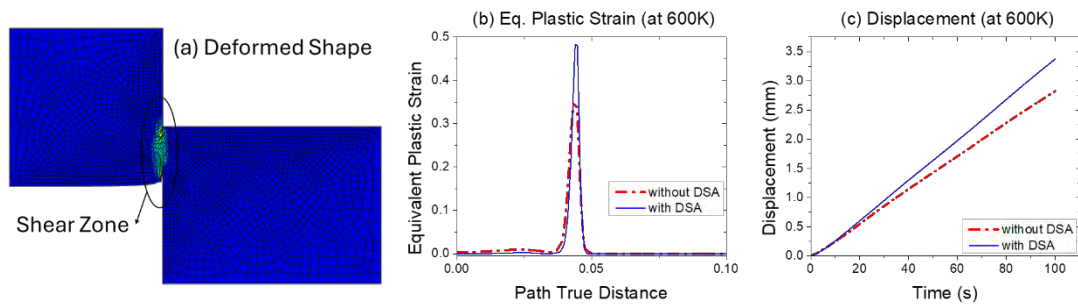


Figure 59 (a) Stress distribution across the deformed sample, (b) Equivalent plastic strain along the path, and (c) Nodal displacement after deformation for Nb at 0.001/s strain rate and 600K temperature.

Similar trends were observed when the metal was subjected to shear loading at 700K temperature (Figure 60(b and c)). Increased strain localization and nodal displacement were observed in the activation region of DSA. As discussed before, the development of cracks in the material increases the strain localization, which leads to earlier failure due to the brittle like failure mode (Figure 60(b)). Once the cracks have developed, the material undergoes pronounced deformation which can be observed in the nodal displacement curve (Figure 60(c)).

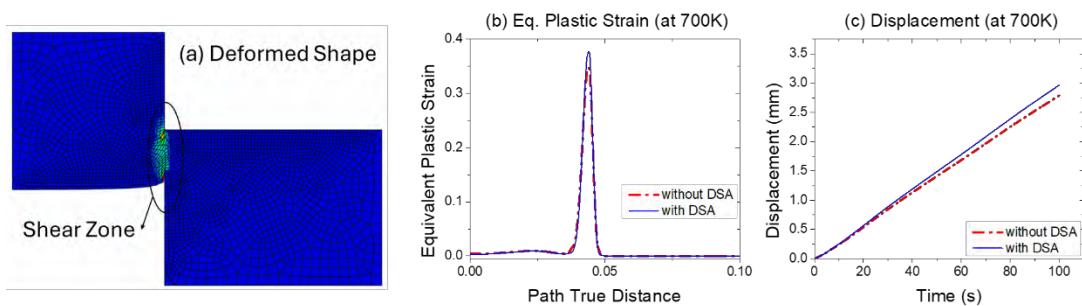


Figure 60 (a) Stress distribution across the deformed sample, (b) Equivalent plastic strain along the path, and (c) Nodal displacement after deformation for Nb at 0.001/s strain rate and 600K temperature.

## Chapter 7. Conclusions

This dissertation can be categorized into two interrelated parts: (a) The development of the constitutive model to predict and capture the activation of Dynamic Strain Aging across different combinations of strain rates and temperatures in pure metals having different crystal structures and alloys; and (b) The numerical implementation of the constitutive equations to carry out finite element simulations using the commercial software ABAQUS through FE code written in VUMAT.

### (a) Constitutive Model for dynamic strain aging

This part of the thesis develops the constitutive model which enables it to capture dynamic strain aging in metals and alloys. This has been achieved through the formulation of a diffusion-based expression for the interstitial/solute atoms inside the metallic structure. This expression first calculates a strain rate parameter (referred here as the DSA strain rate), which depends on the diffusion constant and activation energy that results in an increased waiting time for dislocations. This parameter also depend on the applied temperature and strain rate which empowers it to predict the temperature range for activation of DSA at a particular strain rate. The model has been verified for different commercially pure metals (Niobium, Vanadium and Titanium) and steel alloys (C45 and MMFX) over a broad range of temperature and strain rates. The highlightable conclusion for this section of dissertation comprises:

- Dynamic Strain Aging (DSA) in metals is activated when the impurity or solute atoms diffuse along the dislocation core through pipe diffusion. This results in a pinning effect that obstructs the movement of dislocations across the local obstacles, ultimately causing an increase in the strength of the metals.
- DSA occurs when the dislocation waiting time becomes equivalent to the time it takes for the impurity/solute atoms to diffuse over the width of the local obstacles. This helps in defining the temperature range for activation of DSA at a particular strain rate for different metals.
- The variation of temperature range for different metals is related to the distinctive diffusion kinetics of each impurity/solute atoms at different temperatures. The pinning effect generated due to the diffusion is material

specific and influenced by several physical and microstructural parameters, including dislocation density, burgers vector, average activation distance, diffusion constant, activation energy, and applied strain rate.

- The strengthening in metal is associated to the increase in concentration of impurity/solute atoms that diffuse into the dislocation core through pipe diffusion. This concentration progressively increases as the temperature continues to rise until it reaches a maximum level.
- The steel alloys discussed in this dissertation showed damage while approaching failure. This damage is attributed to the formation of microstructural voids and defects. To capture this, the model efficacy was enhanced by combing it with an energy-based damage parameter and the results showed good comparison with the experimental data for these alloys.
- The proposed constitutive model has been utilized effectively to capture DSA. The accuracy is demonstrated through comparison with the experimental data, validating its ability to predict thermomechanical stress-strain profile both in the presence and absence of dynamic strain aging.

#### **(b) FE Simulations for dynamic strain aging**

This part of the dissertation provides the numerical integration of the constitutive equations. Thermal and athermal yield functions are established based on the von Mises type yield criterion, which apply to both dynamic and static deformations. The concepts given are equivalent to the dynamic and static yield surfaces used in the framework of plasticity/viscoplasticity by merging thermal activation analysis with dislocation interaction processes and the proposed definitions are applicable to a wide range of strain rates and temperatures.

The dynamic/adiabatic deformation considers the influence of temperature and strain rate, whereas the static/isothermal formulation assumes a yield function that is independent of the strain rate and temperature. To provide an accurate description of the material's dynamic behaviour, a precise definition for the magnitude of the viscoplastic flow is essential. Therefore, two separate definitions for the viscoplastic multiplier are provided. The first definition is formulated based on the Perzyna

viscoplastic model, whereas the second definition is derived by applying the same concept to the Consistency model.

Later, two numerical examples are simulated to evaluate the efficacy and performance of the proposed framework and its finite element implementation in ABAQUS under various thermomechanical loading scenarios. The main highlights of this section are:

- In Perzyna model, viscoplasticity occurs by a rate independent yield function. For rate-dependent yield functions, the viscoplasticity is modelled using the consistency model. Once the viscoplastic multiplier is obtained, the values for stress and other state variables are calculated and updated accordingly.
- The substitution of the static and dynamic yield functions with thermal and athermal yield surfaces in the thermodynamic formulation is deemed satisfactory. Moreover, the static yield surface show consistency with the athermal yield surface when the temperature approaches the critical temperature.
- The effectiveness of the numerical framework is verified through the FE simulations conducted in ABAQUS. A single element is first subjected to tensile loading scenario to obtain thermomechanical stress strain curves for the studied pure metals (Niobium, Vanadium, and Titanium) and steel alloys (C45, and MMFX). The simulation results compare very well with the available experimental data, thus validating the model's accuracy.
- The simulations conducted for tensile testing of a cylindrical rod show that the metals exhibiting DSA demonstrated more pronounced neck reduction in comparison to the ones simulated in the absence of DSA. This is attributed to the increase in stress due to segregation of impurities along dislocations during DSA, which increase the material viscosity and reduce its ductility, consequently deteriorating its ability to undergo plastic deformation.
- Shear testing conducted for the axisymmetric hat-shaped samples indicate that the activation of DSA leads an increase in the strain localization within the shear zone. This results in the development of cracks which rapidly decrease the stress bearing capability, thus leading to an earlier failure in the material.

This dissertation develops a deeper understanding of dynamic strain aging in metals and alloys, making it an invaluable resource for researchers in the fields of material science and engineering. It not only enhances the theoretical perspective of the DSA phenomenon but also offers practical implications for its application and further investigation.

Future works in this field can focus on the development of an activation energy-based impurity/solute concentration profile with respect to the change in temperature within the activation region of dynamic strain aging. Moreover, the numerical investigations of the viscosity parameter with respect to the diffusion kinetics may lead to further clarification of the early necking phenomenon.

Applications can be expanded to carry out simulations with three dimensional problems to predict and understand the role of DSA in complex geometries. Detailed experimental works, aided with microstructural studies, can be carried out to further enhance the material behavior during DSA. Recent studies have shown that emerging materials, such as medium and high entropy alloys, also exhibit DSA. Therefore, expanding the current model to encompass these materials would be an interesting avenue for future investigations, thus broadening its applicability and significance in materials science and engineering.

## References

- [1] M. Ghazisaeidi, L. Hector Jr, and W. Curtin, "Solute strengthening of twinning dislocations in Mg alloys," *Acta materialia*, vol. 80, pp. 278-287, 2014.
- [2] R. Mulford and U. Kocks, "New observations on the mechanisms of dynamic strain aging and of jerky flow," *Acta Metallurgica*, vol. 27, no. 7, pp. 1125-1134, 1979.
- [3] L. De Almeida, I. Le May, and P. Emygdio, "Mechanistic modeling of dynamic strain aging in austenitic stainless steels," *Materials characterization*, vol. 41, no. 4, pp. 137-150, 1998.
- [4] J. Cheng and S. Nemat-Nasser, "A model for experimentally-observed high-strain-rate dynamic strain aging in titanium," *Acta materialia*, vol. 48, no. 12, pp. 3131-3144, 2000.
- [5] S. Nemat-Nasser and W.-G. Guo, "Thermomechanical response of HSLA-65 steel plates: experiments and modeling," *Mechanics of Materials*, vol. 37, no. 2-3, pp. 379-405, 2005.
- [6] S. Nemat-Nasser, W.-G. Guo, and D. P. Kihl, "Thermomechanical response of AL-6XN stainless steel over a wide range of strain rates and temperatures," *Journal of the Mechanics and Physics of Solids*, vol. 49, no. 8, pp. 1823-1846, 2001.
- [7] A. Paul and S. Divinski, *Handbook of Solid State Diffusion: Volume 1: Diffusion Fundamentals and Techniques*. Oxford, UK: Elsevier, 2017.
- [8] G. Z. Voyiadjis and F. H. Abed, "Effect of dislocation density evolution on the thermomechanical response of metals with different crystal structures at low and high strain rates and temperatures," *Archives of Mechanics*, vol. 57, no. 4, pp. 299-343, 2005.
- [9] G. Z. Voyiadjis and F. H. Abed, "Microstructural based models for bcc and fcc metals with temperature and strain rate dependency," *Mechanics of Materials*, vol. 37, no. 2-3, pp. 355-378, 2005.
- [10] F. H. Abed, S. I. Ranganathan, and M. A. Serry, "Constitutive modeling of nitrogen-alloyed austenitic stainless steel at low and high strain rates and temperatures," *Mechanics of Materials*, vol. 77, pp. 142-157, 2014.

- [11] A. Tabei, F. Abed, G. Voyiadjis, and H. Garmestani, "Constitutive modeling of Ti-6Al-4V at a wide range of temperatures and strain rates," *European Journal of Mechanics-A/Solids*, vol. 63, pp. 128-135, 2017.
- [12] A. Abdul-Latif, F. Abed, C. Oucif, and G. Voyiadjis, "Effect of various temperatures and strain-rates combinations on the thermomechanical behavior of 42CrMo steel," *Archives of Mechanics*, vol. 74, no. 5, pp. 1-28, 2022.
- [13] F. Abed, A. Abdul-Latif, and A. Yehia, "Experimental study on the mechanical behavior of EN08 steel at different temperatures and strain rates," *Metals*, vol. 8, no. 9, p. 736, 2018.
- [14] F. Abed, A. Abdul-Latif, and G. Z. Voyiadjis, "Performance of MMFX steel rebar at elevated temperatures," *Journal of Engineering Mechanics*, vol. 146, no. 11, p. 04020126, 2020.
- [15] F. H. Abed and G. Z. Voyiadjis, "Plastic deformation modeling of AL-6XN stainless steel at low and high strain rates and temperatures using a combination of bcc and fcc mechanisms of metals," *International Journal of Plasticity*, vol. 21, no. 8, pp. 1618-1639, 2005.
- [16] F. H. Abed and G. Voyiadjis, "Adiabatic shear band localizations in BCC metals at high strain rates and various initial temperatures," *International Journal for Multiscale Computational Engineering*, vol. 5, no. 3-4, 325-349, 2007.
- [17] F. H. Abed, A. K. Al-Tamimi, and R. M. Al-Himairee, "Characterization and modeling of ductile damage in structural steel at low and intermediate strain rates," *Journal of engineering mechanics*, vol. 138, no. 9, pp. 1186-1194, 2012.
- [18] F. Abed, W. Abuzaid, and Y. Morad, "Thermomechanical response of Mg AZ31 at different levels of temperatures and strain rates," in *MATEC Web of Conferences*, Athens, Greece, 2019, vol. 304: EDP Sciences, p. 01025.
- [19] G. Voyiadjis and F. Abed, "Transient localizations in metals using microstructure-based yield surfaces," *Modelling and Simulation in Materials Science and Engineering*, vol. 15, no. 1, p. S83, 2006.
- [20] F. Abed, T. Jankowiak, and A. Rusinek, "Verification of a Thermoviscoplastic Constitutive Relation for Brass Material Using Taylor's Test," *Journal of Engineering Materials and Technology*, vol. 137, no. 4, p. 041005, 2015.

- [21] F. H. Abed, M. H. Saffarini, A. Abdul-Latif, and G. Z. Voyiadjis, "Flow stress and damage behavior of C45 steel over a range of temperatures and loading rates," *Journal of Engineering Materials and Technology*, vol. 139, no. 2, p. 021012, 2017.
- [22] G. R. Johnson and W. H. Cook, "Fracture characteristics of three metals subjected to various strains, strain rates, temperatures and pressures," *Engineering fracture mechanics*, vol. 21, no. 1, pp. 31-48, 1985.
- [23] D. L. Preston, D. L. Tonks, and D. C. Wallace, "Model of plastic deformation for extreme loading conditions," *Journal of applied physics*, vol. 93, no. 1, pp. 211-220, 2003.
- [24] S. Nemat-Nasser and W. Guo, "High strain-rate response of commercially pure vanadium," *Mechanics of Materials*, vol. 32, no. 4, pp. 243-260, 2000.
- [25] F. J. Zerilli and R. W. Armstrong, "Dislocation-mechanics-based constitutive relations for material dynamics calculations," *Journal of applied physics*, vol. 61, no. 5, pp. 1816-1825, 1987.
- [26] J. Wang, W.-G. Guo, X. Gao, and J. Su, "The third-type of strain aging and the constitutive modeling of a Q235B steel over a wide range of temperatures and strain rates," *International Journal of Plasticity*, vol. 65, pp. 85-107, 2015.
- [27] G. Z. Voyiadjis, Y. Song, and A. Rusinek, "Constitutive model for metals with dynamic strain aging," *Mechanics of Materials*, vol. 129, pp. 352-360, 2019.
- [28] Y. Song and G. Z. Voyiadjis, "Constitutive modeling of dynamic strain aging for HCP metals," *European Journal of Mechanics-A/Solids*, vol. 83, p. 104034, 2020.
- [29] W. Cao, J. Yang, and H. Zhang, "Unified constitutive modeling of Haynes 230 including cyclic hardening/softening and dynamic strain aging under isothermal low-cycle fatigue and fatigue-creep loads," *International Journal of Plasticity*, vol. 138, p. 102922, 2021.
- [30] S. P. Mates and S.-Y. Li, "Dynamic Plasticity Model for Rapidly Heated 1045 Steel Up to 1000 C," *Journal of Research of the National Institute of Standards and Technology*, vol. 126, pp. 1-17, 2021.
- [31] S. Gangireddy, "A Modified Johnson-Cook Model for Cp-Ti to Incorporate the Effects of Dynamic Strain Aging and Phase Transformation,"

- International Journal of Metallurgy and Metal Physics*, vol. 3, no. 2, pp. 1-11, 2018.
- [32] A. Moris Devotta *et al.*, "A modified Johnson-Cook model for ferritic-pearlitic steel in dynamic strain aging regime," *Metals*, vol. 9, no. 5, p. 528, 2019.
- [33] J. Chaboche, "Thermodynamics of local state: overall aspects and micromechanics based constitutive relations," *Technische Mechanik*, vol. 23, no. 2-4, pp. 113-119, 2003.
- [34] J. Lemaitre and J. Dufailly, "Damage measurements," *Engineering Fracture Mechanics*, vol. 28, no. 5-6, pp. 643-661, 1987.
- [35] R. M. Al-Himairee, F. H. Abed, and A. K. Al-Tamimi, "Damage evolution in structural steel at different loading conditions," *Key Engineering Materials*, vol. 471, pp. 969-974, 2011.
- [36] N. Bonora, D. Gentile, and A. Pirondi, "Identification of the parameters of a non-linear continuum damage mechanics model for ductile failure in metals," *The Journal of Strain Analysis for Engineering Design*, vol. 39, no. 6, pp. 639-651, 2004.
- [37] S. Chandrakanth and P. Pandey, "A new ductile damage evolution model," *International Journal of Fracture*, vol. 60, no. 4, pp. R73-R76, 1993.
- [38] B. M. Darras, F. H. Abed, S. Pervaiz, and A. Abdu-Latif, "Analysis of damage in 5083 aluminum alloy deformed at different strainrates," *Materials Science and Engineering: A*, vol. 568, pp. 143-149, 2013.
- [39] J. Lemaitre, "How to use damage mechanics," *Nuclear engineering and design*, vol. 80, no. 2, pp. 233-245, 1984.
- [40] W. H. Tai, "Plastic damage and ductile fracture in mild steels," *Engineering Fracture Mechanics*, vol. 37, no. 4, pp. 853-880, 1990.
- [41] M. Zheng, C. Hu, Z. Luo, and X. Zheng, "A ductile damage model corresponding to the dissipation of ductility of metal," *Engineering fracture mechanics*, vol. 53, no. 4, pp. 653-659, 1996.
- [42] G. Z. Voyiadjis and Y. Song, "A physically based constitutive model for dynamic strain aging in Inconel 718 alloy at a wide range of temperatures and strain rates," *Acta Mechanica*, vol. 231, no. 1, pp. 19-34, 2020.

- [43] S. Nemat-Nasser, W. Guo, and J. Cheng, "Mechanical properties and deformation mechanisms of a commercially pure titanium," *Acta materialia*, vol. 47, no. 13, pp. 3705-3720, 1999.
- [44] S. Nemat-Nasser and W. Guo, "Flow stress of commercially pure niobium over a broad range of temperatures and strain rates," *Materials Science and Engineering: A*, vol. 284, no. 1-2, pp. 202-210, 2000.
- [45] Y. Lin, H. Yang, X. M. Chen, and D. D. Chen, "Influences of Initial Microstructures on Portevin-Le Chatelier Effect and Mechanical Properties of a Ni-Fe-Cr-Base Superalloy," *Advanced Engineering Materials*, vol. 20, no. 8, p. 1800234, 2018.
- [46] G. Ananthakrishna, "Current theoretical approaches to collective behavior of dislocations," *Physics reports*, vol. 440, no. 4-6, pp. 113-259, 2007.
- [47] S. Chen *et al.*, "Temperature effects on the serrated behavior of an Al<sub>0.5</sub>CoCrCuFeNi high-entropy alloy," *Materials Chemistry and Physics*, vol. 210, pp. 20-28, 2018.
- [48] J. Brechtel *et al.*, "A review of the serrated-flow phenomenon and its role in the deformation behavior of high-entropy alloys," *Metals*, vol. 10, no. 8, p. 1101, 2020.
- [49] S. Nalawade, M. Sundararaman, R. Kishore, and J. Shah, "The influence of aging on the serrated yielding phenomena in a nickel-base superalloy," *Scripta Materialia*, vol. 59, no. 9, pp. 991-994, 2008.
- [50] H. Aboulfadl, J. Deges, P. Choi, and D. Raabe, "Dynamic strain aging studied at the atomic scale," *Acta Materialia*, vol. 86, pp. 34-42, 2015.
- [51] A. Abhijit, J. Varghese, P. Chalavadi, P. Sai Karthik, K. Bhanu Sankara Rao, and K. Rajulapati, "Negative strain rate sensitivity in two-phase nanocrystalline CoCrFeMnNi high-entropy alloy with broader grain size distribution studied by nanoindentation," *Transactions of the Indian Institute of Metals*, vol. 72, no. 10, pp. 2861-2867, 2019.
- [52] J. Xu, B. Holmedal, O. S. Hopperstad, T. Mánik, and K. Marthinsen, "Dynamic strain ageing in an AlMg alloy at different strain rates and temperatures: experiments and constitutive modelling," *International Journal of Plasticity*, vol. 151, p. 103215, 2022.

- [53] R. Khani, A. Zarei-Hanzaki, A. Moshiri, H. Abedi, and S. S. Sohn, "Dynamic strain aging and twin formation during warm deformation of a novel medium-entropy lightweight steel," *journal of materials research and technology*, vol. 17, pp. 1628-1641, 2022.
- [54] J. Xing, L. Hou, H. Du, B. Liu, and Y. Wei, "A new explanation for the effect of dynamic strain aging on negative strain rate sensitivity in Fe–30Mn–9Al–1C steel," *Materials*, vol. 12, no. 20, p. 3426, 2019.
- [55] T. Ogawa, M. Koyama, C. C. Tasan, K. Tsuzaki, and H. Noguchi, "Effects of martensitic transformability and dynamic strain age hardenability on plasticity in metastable austenitic steels containing carbon," *Journal of Materials Science*, vol. 52, pp. 7868-7882, 2017.
- [56] M. Koyama, T. Sawaguchi, T. Lee, C. S. Lee, and K. Tsuzaki, "Work hardening associated with  $\epsilon$ -martensitic transformation, deformation twinning and dynamic strain aging in Fe–17Mn–0.6 C and Fe–17Mn–0.8 C TWIP steels," *Materials Science and Engineering: A*, vol. 528, no. 24, pp. 7310-7316, 2011.
- [57] Y. Cao, C. Zhang, C. Zhang, H. Di, G. Huang, and Q. Liu, "Influence of dynamic strain aging on the mechanical properties and microstructural evolution for Alloy 800H during hot deformation," *Materials Science and Engineering: A*, vol. 724, pp. 37-44, 2018.
- [58] Y. Cao *et al.*, "Effect of dynamic strain aging and precipitation on the hot deformation behavior of 253MA heat-resistant alloy," *Journal of Materials Science*, vol. 54, no. 2, pp. 1716-1727, 2019.
- [59] M. Pham and S. Holdsworth, "Dynamic strain ageing of AISI 316L during cyclic loading at 300 C: Mechanism, evolution, and its effects," *Materials Science and Engineering: A*, vol. 556, pp. 122-133, 2012.
- [60] W. Karlsen, M. Ivanchenko, U. Ehrnstén, Y. Yagodzinsky, and H. Hänninen, "Microstructural manifestation of dynamic strain aging in AISI 316 stainless steel," *Journal of nuclear materials*, vol. 395, no. 1-3, pp. 156-161, 2009.
- [61] J.-D. Hong, J. Lee, C. Jang, and T. S. Kim, "Low cycle fatigue behavior of alloy 690 in simulated PWR water—Effects of dynamic strain aging and hydrogen," *Materials Science and Engineering: A*, vol. 611, pp. 37-44, 2014.

- [62] X. Li *et al.*, "Effects of temperature and strain rate on tensile properties and dynamic strain aging behaviour of LPBF Hastelloy X," *Additive Manufacturing Letters*, vol. 4, p. 100105, 2023.
- [63] P. Follansbee, "A Model for Dynamic Strain Aging," in *Fundamentals of Strength: Principles, Experiments, and Applications of an Internal State Variable Constitutive Formulation*. Cham, Switzerland: Springer, 2022, pp. 409-434.
- [64] Y. Song and W. Peterson, "Theoretical study for dynamic strain aging in niobium: Effect of temperature and strain rate on the flow stress," *Metals and Materials International*, vol. 28, no. 3, pp. 589-602, 2022.
- [65] S. Nemat-Nasser and Y. Li, "Flow stress of fcc polycrystals with application to OFHC Cu," *Acta Materialia*, vol. 46, no. 2, pp. 565-577, 1998.
- [66] A. Marchenko, M. Maziere, S. Forest, and J.-L. Strudel, "Crystal plasticity simulation of strain aging phenomena in  $\alpha$ -titanium at room temperature," *International Journal of Plasticity*, vol. 85, pp. 1-33, 2016.
- [67] S. Serajzadeh and H. Sheikh, "Investigation into occurring dynamic strain aging in hot rolling of AA5083 using finite elements and stream function method," *Materials Science and Engineering: A*, vol. 486, no. 1-2, pp. 138-145, 2008.
- [68] F. Bleicher *et al.*, "Considering the influence of heating rate, complex hardening and dynamic strain aging in AISI 1045 machining: experiments and simulations," *CIRP Annals*, vol. 70, no. 1, pp. 49-52, 2021.
- [69] Y. Song, J. Yeon, and G. Z. Voyiadjis, "Constitutive modeling and numerical simulations for dynamic strain aging in MMFX steel at elevated temperatures," *International Journal of Mechanical Sciences*, vol. 210, p. 106743, 2021.
- [70] N. Anjabin, A. K. Taheri, and H. Kim, "Simulation and experimental analyses of dynamic strain aging of a supersaturated age hardenable aluminum alloy," *Materials Science and Engineering: A*, vol. 585, pp. 165-173, 2013.
- [71] E. Orowan, *Symposium on internal stresses in metals and alloys*. London, UK: Institute of Metals, 1948, p. 543.
- [72] U. F. Kocks, A. AS, and A. MF, *Thermodynamics and kinetics of slip*. Oxford, England: Pergamon Press Ltd., 1975, p. 304.

- [73] R. Kapoor and S. Nemat-Nasser, "Determination of temperature rise during high strain rate deformation," *Mechanics of materials*, vol. 27, no. 1, pp. 1-12, 1998.
- [74] L. Kubin and Y. Estrin, "Evolution of dislocation densities and the critical conditions for the Portevin-Le Chatelier effect," *Acta metallurgica et materialia*, vol. 38, no. 5, pp. 697-708, 1990.
- [75] F. H. Abed, "Physically based multiscale-viscoplastic model for metals and steel alloys: theory and computation," PhD Dissertation, Civil and Environmental Engineering, Louisiana State University and Agricultural & Mechanical College, Baton Rouge, LA, USA, 294, 2005.
- [76] A. Hassan and F. Abed, "Constitutive modelling of thermomechanical abnormalities due to dynamic strain aging in commercially pure titanium," *Journal of Materials Research and Technology*, vol. 25, pp. 5174-5183, 2023.
- [77] G. Z. Voyiadjis and F. H. Abed, "A coupled temperature and strain rate dependent yield function for dynamic deformations of bcc metals," *International Journal of Plasticity*, vol. 22, no. 8, pp. 1398-1431, 2006.
- [78] W. Wang, "Stationary and propagative instabilities in metals: A computational point of view," PhD Dissertation, Technische Universiteit Delft, Delft University Press, Netherlands, 1998.
- [79] S. A. Batool, A. Ahmad, A. Wadood, A. Mateen, and W. Hussain, "Development of lightweight aluminum-titanium alloys for aerospace applications," in *Key Engineering Materials*, 2018, vol. 778: Trans Tech Publ, pp. 22-27.
- [80] S. Mahmood *et al.*, "Microstructure, consolidation, electrochemical, and mechanical performance of titanium (Ti) composites reinforced by graphene nanoplatelets (GNPs) via mechanical alloying," *Materials Chemistry and Physics*, vol. 285, p. 126142, 2022.
- [81] A. Wadood, "Brief overview on nitinol as biomaterial," *Advances in Materials Science and Engineering*, vol. 2016, pp. 1-9, 2016.
- [82] A. Wadood, *Titanium and Titanium Alloys*. Islamabad, Pakistan: Higher Education Commission, 2018, pp. 1-144.
- [83] A. Rusinek and J. Klepaczko, "Shear testing of a sheet steel at wide range of strain rates and a constitutive relation with strain-rate and temperature

- dependence of the flow stress," *International Journal of Plasticity*, vol. 17, no. 1, pp. 87-115, 2001.
- [84] A. Rusinek, J. Rodriguez-Martinez, J. Klepaczko, and R. Pęcherski, "Analysis of thermo-visco-plastic behaviour of six high strength steels," *Materials & Design*, vol. 30, no. 5, pp. 1748-1761, 2009.
- [85] P. Simon, Y. Demarty, A. Rusinek, and G. Z. Voyiadjis, "Material behavior description for a large range of strain rates from low to high temperatures: Application to high strength steel," *Metals*, vol. 8, no. 10, p. 795, 2018.
- [86] L. Gong, D. Darwin, J. P. Browning, and C. E. Locke Jr, "Evaluation of mechanical and corrosion properties of MMFX reinforcing steel for concrete," Kansas. Dept. of Transportation, Kansas, US, 2004.
- [87] Y. Zhou, Y.-C. Ou, G. C. Lee, and J. S. O'Connor, "Mechanical and low-cycle fatigue behavior of stainless reinforcing steel for earthquake engineering applications," *Earthquake Engineering and Engineering Vibration*, vol. 9, no. 3, pp. 449-457, 2010.
- [88] J. Ji, D. Darwin, and J. Browning, "Corrosion resistance of duplex stainless steels and MMFX microcomposite steel for reinforced concrete bridge decks," University of Kansas Center for Research, Inc., Lawrence, Kansas, 2005.
- [89] G. Szala and B. Ligaj, "Application of hybrid method in calculation of fatigue life for C45 steel (1045 steel) structural components," *International Journal of Fatigue*, vol. 91, pp. 39-49, 2016.
- [90] D. Rigon, F. Berto, and G. Meneghetti, "Estimating the multiaxial fatigue behaviour of C45 steel specimens by using the energy dissipation," *International Journal of Fatigue*, vol. 151, p. 106381, 2021.
- [91] P. Opěla *et al.*, "Hot flow stress models of the steel C45," *Metalurgija*, vol. 54, no. 3, pp. 469-472, 2015.
- [92] M. Stembalski, P. Preś, and W. Skoczyński, "Determination of the friction coefficient as a function of sliding speed and normal pressure for steel C45 and steel 40HM," *Archives of civil and mechanical engineering*, vol. 13, no. 4, pp. 444-448, 2013.
- [93] S. Genna, C. Leone, V. Lopresto, L. Santo, and F. Trovalusci, "Study of fibre laser machining of C45 steel: influence of process parameters on material

- removal rate and roughness," *International Journal of Material Forming*, vol. 3, no. 1, pp. 1115-1118, 2010.
- [94] J. Padgurskas *et al.*, "Tribological properties of coatings obtained by electro-spark alloying C45 steel surfaces," *Surface and Coatings Technology*, vol. 311, pp. 90-97, 2017.
- [95] M. Szkodo, "Relationship between microstructure of laser alloyed C45 steel and its cavitation resistance," *Journal of Materials Processing Technology*, vol. 162, pp. 410-415, 2005.
- [96] I. Magnabosco, P. Ferro, A. Tiziani, and F. Bonollo, "Induction heat treatment of a ISO C45 steel bar: Experimental and numerical analysis," *Computational materials science*, vol. 35, no. 2, pp. 98-106, 2006.
- [97] N. Ranc, V. Favier, B. Munier, F. Vales, G. Thoquenne, and F. Lefebvre, "Thermal response of C45 steel in high and very high cycle fatigue," *Procedia Engineering*, vol. 133, pp. 265-271, 2015.
- [98] M. Gensamer, "Strength and ductility," *Metallography, Microstructure, and Analysis*, vol. 6, pp. 171-185, 2017.

## Vita

Arhum Hassan was born on June 10, 1991, in Rawalpindi, Pakistan. He got his primary and secondary education from local schools in Rawalpindi. Later, he was graduated from Institute of Space Technology (IST), Islamabad, Pakistan with a Bachelor of Science degree in Materials Science and Engineering in August 2015. He started working as a graduate teaching assistant in the department of Materials Science and Engineering, IST from September 2015 and later joined the same department in 2016 as Teaching/Research Associate where apart from teaching different lab courses, he contributed to the departmental curriculum development to get the bachelor's program accredited from the Washington Accord. He completed his Master of Science degree in Materials Science and Engineering in August 2019, where he developed PbS/TiO<sub>2</sub>/MoS<sub>2</sub> nanocomposite based Photoanode material for Solar paint application. In spring 2021, he joined the American University of Sharjah as a PhD scholar in Materials Science and Engineering. As a PhD student, he worked on the development of a constitutive and numerical model for dynamic strain aging in metals and alloys. He has participated in different national and international conferences and published his works in prestigious journals. He got married to Syeda Ifrah Bint e Sarwat in 2018 in Pakistan and has a five-year-old daughter named Zoeya e Hassan.